

**AFRL-VA-WP-TR-2000-3023**

**DYNAMICS OF AEROSPACE VEHICLES --  
NONLINEAR FLIGHT MECHANICS**



**JERRY E. JENKINS  
GREGORY A. ADDINGTON  
PHILLIP S. BERAN  
DEBORAH S. GRISMER  
ERNEST S. HANFF  
ALEXANDER H. HSIA  
CHARLES E. JOBE  
JAMES H. MYATT  
JEFFREY C. TROMP**

**AFRL/VACA  
BLDG. 146, ROOM 305  
2210 8<sup>TH</sup> STREET  
WRIGHT-PATTERSON AFB, OH 45433-7542**

**MAY 2000**

**FINAL REPORT FOR 06/01/1987 – 06/30/1998**

**APPROVED FOR PUBLIC RELEASE; DISTRIBUTION UNLIMITED**

**AIR VEHICLES DIRECTORATE  
AIR FORCE RESEARCH LABORATORY  
AIR FORCE MATERIEL COMMAND  
WRIGHT-PATTERSON AIR FORCE BASE OH 45433-7542**

**DTIC QUALITY INSPECTED 4**

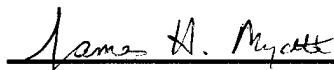
**20000803 180**

## NOTICE

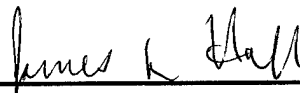
USING GOVERNMENT DRAWINGS, SPECIFICATIONS, OR OTHER DATA INCLUDED IN THIS DOCUMENT FOR ANY PURPOSE OTHER THAN GOVERNMENT PROCUREMENT DOES NOT IN ANY WAY OBLIGATE THE US GOVERNMENT. THE FACT THAT THE GOVERNMENT FORMULATED OR SUPPLIED THE DRAWINGS, SPECIFICATIONS, OR OTHER DATA DOES NOT LICENSE THE HOLDER OR ANY OTHER PERSON OR CORPORATION; OR CONVEY ANY RIGHTS OR PERMISSION TO MANUFACTURE, USE, OR SELL ANY PATENTED INVENTION THAT MAY RELATE TO THEM.

THIS REPORT IS RELEASABLE TO THE NATIONAL TECHNICAL INFORMATION SERVICE (NTIS). AT NTIS, IT WILL BE AVAILABLE TO THE GENERAL PUBLIC, INCLUDING FOREIGN NATIONS.


THIS TECHNICAL REPORT HAS BEEN REVIEWED AND IS APPROVED FOR PUBLICATION.



JAMES H. MYATT, PhD  
Aerospace Engineer  
Control Theory Optimization Branch



JAMES K. HALL, Capt, USAF  
Chief, Control Theory Optimization Branch  
Control Sciences Division



JOHN A. BOWLUS  
Chief, Control Sciences Division  
Air Vehicles Directorate

Do not return copies of this report unless contractual obligations or notice on a specific document require its return.

REPORT DOCUMENTATION PAGE			Form Approved OMB No. 0704-0188	
Public reporting burden for this collection of information is estimated to average 1 hour per response, including the time for reviewing instructions, searching existing data sources, gathering and maintaining the data needed, and completing and reviewing the collection of information. Send comments regarding this burden estimate or any other aspect of this collection of information, including suggestions for reducing this burden, to Washington Headquarters Services, Directorate for Information Operations and Reports, 1215 Jefferson Davis Highway, Suite 1204, Arlington, VA 22202-4302, and to the Office of Management and Budget, Paperwork Reduction Project (0704-0188), Washington, DC 20503.				
1. AGENCY USE ONLY (Leave blank)		2. REPORT DATE MAY 2000		3. REPORT TYPE AND DATES COVERED FINAL REPORT FOR 06/01/1987 - 06/30/1998
4. TITLE AND SUBTITLE DYNAMICS OF AEROSPACE VEHICLES -- NONLINEAR FLIGHT MECHANICS			5. FUNDING NUMBERS C IN-HOUSE PE 61102 PR 2307 TA N3 WU 29	
6. AUTHOR(S) JERRY E. JENKINS, GREGORY A. ADDINGTON, PHILLIP S. BERAN, DEBORAH S. GRISMER, ERNEST S. HANFF, ALEXANDER H. HSIA, CHARLES E. JOBE, JAMES H. MYATT, AND JEFFREY C. TROMP				
7. PERFORMING ORGANIZATION NAME(S) AND ADDRESS(ES) AFRL/VACA BLDG. 146, ROOM 305 2210 8th STREET WRIGHT-PATTERSON AFB, OH 45433-7542			8. PERFORMING ORGANIZATION REPORT NUMBER	
9. SPONSORING/MONITORING AGENCY NAME(S) AND ADDRESS(ES) AIR VEHICLES DIRECTORATE AIR FORCE RESEARCH LABORATORY AIR FORCE MATERIEL COMMAND WRIGHT-PATTERSON AFB, OH 45433-7542 POC: DR. JAMES H. MYATT, AFRL/VACA, 937-255-8491			10. SPONSORING/MONITORING AGENCY REPORT NUMBER  AFRL-VA-WP-TR-2000-3023	
11. SUPPLEMENTARY NOTES				
12a. DISTRIBUTION AVAILABILITY STATEMENT  APPROVED FOR PUBLIC RELEASE, DISTRIBUTION UNLIMITED.			12b. DISTRIBUTION CODE	
13. ABSTRACT (Maximum 200 words)  The unsteady aerodynamics due to vortex breakdown are studied, with application to a 65-degree delta wing. At high angles of attack, the flow field response to changes in attitude contains multiple time scales. Furthermore, severe nonlinearities are present which further complicate aerodynamic modeling. The implications for wind tunnel testing and aerodynamic modeling are discussed.				
14. SUBJECT TERMS Unsteady aerodynamics, Nonlinear Flight Mechanics, Delta Wing, Vortex Breakdown			15. NUMBER OF PAGES 53	
			16. PRICE CODE	
17. SECURITY CLASSIFICATION OF REPORT UNCLASSIFIED	18. SECURITY CLASSIFICATION OF THIS PAGE UNCLASSIFIED	19. SECURITY CLASSIFICATION OF ABSTRACT UNCLASSIFIED	20. LIMITATION OF ABSTRACT SAR	

# **Simplification of Nonlinear Indicial Response Models: Assessment for the Two-Dimensional Airfoil Case**

Jerry E. Jenkins

## **Journal of Aircraft**

Volume 28, Number 2, Pages 131-138

# Simplification of Nonlinear Indicial Response Models: Assessment for the Two-Dimensional Airfoil Case

Jerry E. Jenkins\*

Wright Research and Development Center, Wright-Patterson Air Force Base, Ohio 45433

Simplifications to the functional form of the nonlinear indicial response model and application to the aerodynamic response due to arbitrary motion inputs are discussed. Numerical results for a thin two-dimensional airfoil with wake distortion nonlinearities are used to control and justify the assumptions employed. Useful relationships between indicial response parameters and steady-state oscillatory force and moment data are obtained by representing the indicial response with a Taylor series (in terms of onset motion parameters) and approximating the superposition integral with an asymptotic expansion. In particular, the appearance of certain harmonics and their variation with frequency, amplitude, and mean angle of attack are traced to specific onset parameters. A nonlinear parameter identification procedure is proposed by which active onset parameters may be determined from experimental data. Restrictions imposed by using the asymptotic expansion are also examined. Nonlinear stability derivatives are shown to be related to specific indicial response characteristics.

## Nomenclature

- $A$  = amplitude of harmonic oscillation in  $\alpha$ , rad  
 $C_L$  = section lift coefficient, lift/ $q c$   
 $C_{L_{am}}$  = apparent mass derivative, 1/rad  
 $C_{L_0}$  = mean section lift coefficient for oscillatory motion  
 $C_{L_n}$  = nonlinear indicial response, section lift due to  $\alpha$   
 $c$  = chord length, ft  
 $F$  = deficiency function, difference between steady-state and transient indicial responses, 1/rad  
 $F_0$  = linear deficiency function evaluated at  $\alpha = 0$ , 1/rad  
 $F_2$  = nonlinear deficiency function,  $\partial^2 F / \partial \alpha^2$  evaluated at  $\alpha = 0$ , 1/rad<sup>3</sup>  
 $g_0$  = superposition integral linear onset parameter,  $= \dot{\alpha}$   
 $g_2$  = superposition integral nonlinear onset parameter,  $= \alpha^2 \ddot{\alpha}$   
 $k$  = reduced frequency,  $= \omega c / 2U_\infty$   
 $q$  = dynamic pressure, psf  
 $R_n$  = remainder after  $n$  terms of partial sum  
 $t$  = time, nondimensionalized by  $2U_\infty / c$   
 $U_\infty$  = freestream velocity, ft/s  
 $\alpha$  = angle of attack, rad  
 $\dot{\alpha}, \ddot{\alpha}$  = first and second derivatives of  $\alpha$  with respect to  $t$ , rad  
 $\alpha_0$  = mean angle of attack for harmonic motion, rad  
 $\tau$  = nondimensional time at step onset  
 $\tau_1$  = elapsed nondimensional time from onset,  $= t - \tau$   
 $\omega$  = circular frequency, rad/s

## Introduction

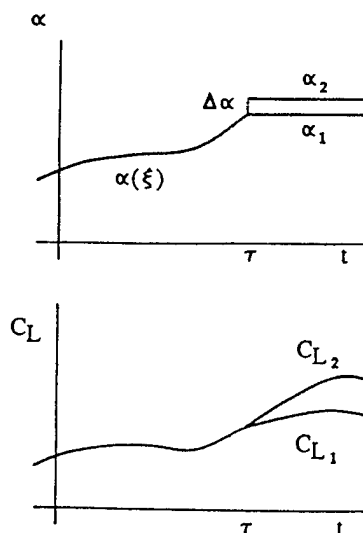
LARGE-AMPLITUDE oscillatory force and moment data typically exhibit nonlinear dependencies on amplitude and frequency. Often these effects can be attributed to hysteresis; sometimes "simple" nonlinear variations in either (or both) static or dynamic force and moment data are the cause. In either case, aerodynamic response modeling for flight mechanics analyses is a difficult problem.

The current work focuses on establishing relationships between steady-state oscillatory force and moment data and models capable of accounting for some of these nonlinear effects. Limits of applicability for these models is also explored. The basis for this study is nonlinear aerodynamic modeling work reported by Tobak and Chapman<sup>1</sup> and Tobak and Schiff.<sup>2</sup>

The modeling concepts apply equally well to any of the six force and moment components and to any motion input, including control deflection; however, lift response due to angle of attack is used throughout to illustrate the concepts.

## Nonlinear Indicial Responses

The nonlinear indicial response is the most generally applicable modeling concept. It is defined in terms of two motions as shown in the following sketch:



where  $\alpha(\xi)$  is the "reference motion," defined for  $-\infty < t \leq \tau$ ;  $\alpha_1$  consists of  $\alpha(\xi)$ , for  $t \leq \tau$ , and is held constant at  $\alpha(\tau)$  for  $t > \tau$ ; and  $\alpha_2$  consists of  $\alpha(\xi)$ , for  $t \leq \tau$ , but jumps instantaneously to  $\alpha(\tau) + \Delta\alpha$  for  $t > \tau$ . The nonlinear indicial lift response is the limit, as step height  $\Delta\alpha$  approaches zero, of the difference between the corresponding lift time histories.

Evidence supporting the need for such a definition is given in Figs. 1-3, taken from Graham's<sup>3</sup> tow-tank experiments

Received July 5, 1989; presented as Paper 89-3351 at the AIAA Atmosphere Flight Mechanics Conference, Boston, MA, Aug. 14-16, 1989; revision received June 8, 1990; accepted for publication June 8, 1990. This paper is declared a work of the U.S. Government and is not subject to copyright protection in the United States.

\*Aerospace Engineer. Member AIAA.

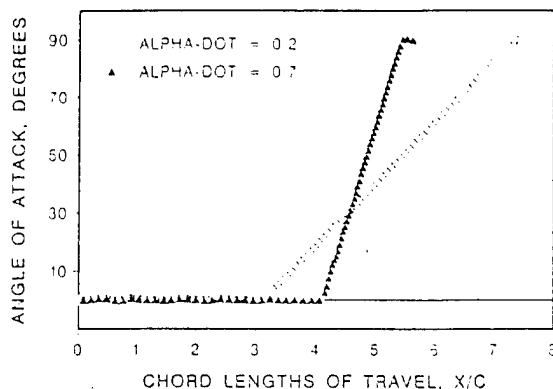


Fig. 1 Reference motions.

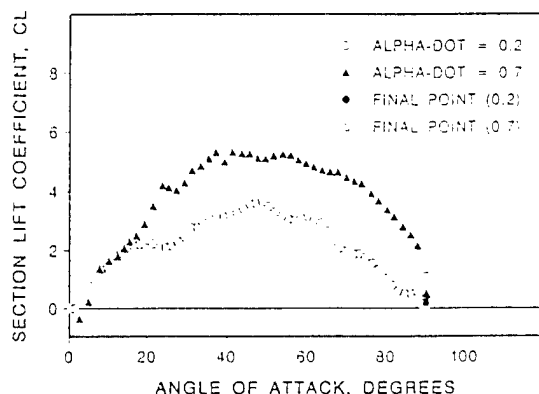


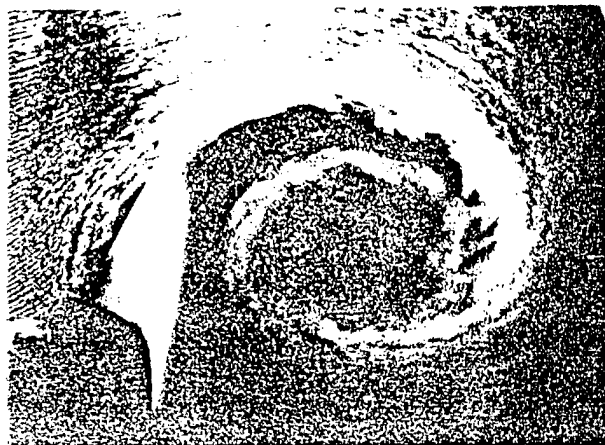
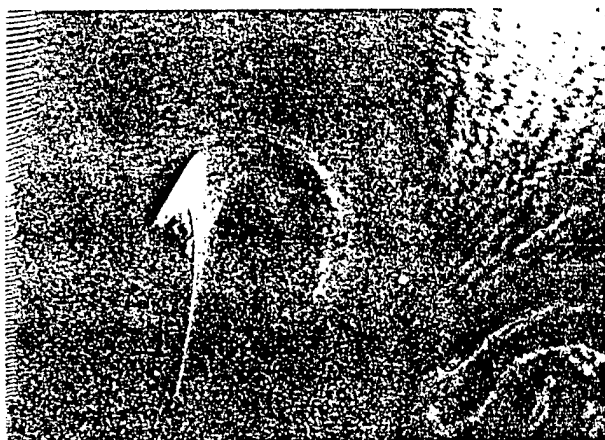
Fig. 2 Lift time history.

using a NACA 0015 airfoil. The point is that motion history effects can have a profound influence on the resulting flowfields, even when there are identical onset conditions. In fact, history effects are completely reflected in the wake structure.

Consider two angle-of-attack time histories, as shown in Fig. 1, which are interpreted as two distinct reference motions. (Graham<sup>3</sup> investigated "poststall maneuvers" that returned to zero angle of attack after holding at high  $\alpha$ ; however, the point is better illustrated by examining only a portion of the complete motion.) Flowfields at the termination of each maneuver ( $\alpha = 90$  deg) are shown in Figs. 3. The flow is left to right and the view is spanwise from the root, slightly above and behind the wing section. Thus, only the upper surface of the wing section is visible; the leading edge is to the top of the picture. For the rapid pitch-up ( $\alpha \dot{=} 0.7$ ), the "dynamic stall" vortex is less diffuse, more tightly wrapped, and closer to the airfoil upper surface than for  $\alpha \dot{=} 0.2$ . Note also that at  $\alpha \dot{=} 0.7$  the starting vortex associated with the onset of the pitch-up motion (lower right) has not had time to be swept downstream and can still exert an appreciable influence on airfoil response. Furthermore, if  $\alpha$  is held constant at this point, these distinctly different vortex systems will also exhibit unique diffusion and convection properties. Correspondingly large differences in lift are observed (Fig. 2). Clearly, motion history effects can be important. Therefore, the reference motion is required to establish appropriate flow conditions from which to measure the corresponding indicial response. The  $\alpha_2$  motion then establishes the change in response due to a small perturbation in  $\alpha$ .

As shown by Tobak and Chapman,<sup>1</sup> the dependence of nonlinear indicial responses on reference motion requires that they be expressed mathematically as a functional, i.e.,

$$C_{L_1}[\alpha(\xi); t, \tau] = \lim_{\Delta \alpha \rightarrow 0} \frac{C_L[\alpha_2(t)] - C_L[\alpha_1(t)]}{\Delta \alpha} \quad (1)$$

Fig. 3a Flow visualization,  $\alpha \dot{=} 0.2$ .Fig. 3b Flow visualization,  $\alpha \dot{=} 0.7$ .

where the step onset is at  $t = \tau$ . The functional dependency on prior motion  $\alpha(\xi)$  distinguishes the nonlinear indicial response from its linear counterpart.

Equation (1) defines the Fréchet derivative of the functional  $C_L[\alpha_1(t)]$ , as noted by Tobak and Chapman.<sup>1</sup> They also suggest that bifurcations of physically realizable (asymptotically stable to small perturbations) steady-state solutions corresponding to  $\alpha_1$  are signaled by loss of Fréchet differentiability. Such occurrences are of considerable interest to the study of hysteresis effects.

Possible simplifications to the functional representation for indicial responses have been suggested by Tobak and Schiff.<sup>2</sup> Suppose that the motion  $\alpha(\xi)$  is analytic (in the strict mathematical sense) over the interval  $-\infty < t < \tau$ . In this case,  $\alpha(\xi)$  may be replaced by its Taylor series expansion about  $\xi = \tau$ . Therefore,

$$C_{L_1}[\alpha(\xi); t, \tau] = C_{L_1}[t, \tau; \alpha(\tau), \dot{\alpha}(\tau), \ddot{\alpha}(\tau), \dots] \quad (2)$$

where the independent variables  $\alpha(\tau), \dot{\alpha}(\tau), \ddot{\alpha}(\tau), \dots$  are the coefficients of the Taylor expansion. On physical grounds, the distant past is expected to be less important to the step response than motion characteristics just prior to onset, suggesting, perhaps, that only a few Taylor series coefficients need to be retained.

Simplifications based on unsteady aerodynamic characteristics for thin two-dimensional airfoils in an inviscid and incompressible fluid are studied in the following section. This approach allows the nonlinear indicial response model to be examined in a context where assumptions may be controlled and justified. However, results reported herein are not applicable to the extreme conditions evident in the example just

presented. Notably large-scale separated flows with corresponding time-dependent equilibrium states are excluded.

Nonlinear thin-airfoil characteristics were obtained by using NLWAKE, a computer code developed by Scott and McCune.<sup>4</sup> NLWAKE provides numerical solutions for a nonlinear version of Wagner's integral equation, which relates the quasisteady bound vorticity to wake vorticity. To do this, the shed vorticity is discretized and the wake allowed to distort under the influence of both bound vorticity and other wake elements. Since NLWAKE disallows separation, only nonlinear wake distortion effects are included. NLWAKE cannot be used to investigate hysteresis effects.

### Two-Dimensional Airfoil with Wake Distortion

Nonlinear step responses computed with NLWAKE are shown in Figs. 4 and 5. The required Fréchet derivatives were computed numerically based on positive and negative step heights of 0.1 deg. Figure 4 shows indicial responses for constant angle of attack prior to onset. In Fig. 5,  $\alpha(\xi)$  is ramped at constant rate (positive and negative) to the same onset  $\alpha$  values. Motion history effects caused by wake distortion have an appreciable influence on the indicial response. However, history effects predicted by NLWAKE correlate very well with onset angle of attack; onset rate having a negligible influence up to quite large values. Thus, for the two-dimensional airfoil in the absence of separation, indicial response functionals may be adequately approximated by a function only of  $\alpha(\tau)$  and elapsed time from onset  $t - \tau$ . This approximation is used in the following development although separation effects are probably important at lower onset rates than shown in Fig. 5.

NLWAKE cannot predict nonlinearities in the static lift-curve slope. However, for completeness, this possibility is included, although coupling between quasisteady characteristics and indicial response time history cannot be explored. Also, there are situations (e.g., following a Hopf bifurcation)

where the response is time dependent even in the limit as elapsed time (since step initiation) approaches infinity. However, a steady-state condition is assumed to exist. In these cases, it is convenient to introduce the "deficiency function"  $F$ :

$$F[\alpha(\tau), t - \tau] = C_{L\alpha}[\alpha(\tau), \infty] - C_{L\alpha}[\alpha(\tau), t - \tau]$$

where the first term on the right side is the steady-state lift-curve slope,

$$C_{L\alpha}[\alpha(\tau), \infty] = \lim_{t - \tau \rightarrow \infty} C_{L\alpha}[\alpha(\tau), t - \tau]$$

and the indicial response is expressed as a function of onset angle of attack and elapsed time as suggested above. Thus Eq. (2) becomes

$$\begin{aligned} C_{L\alpha}[\alpha(\xi); t - \tau] &\approx C_{L\alpha}[\alpha(\tau), t - \tau] \\ &= C_{L\alpha}[\alpha(\tau), \infty] - F[\alpha(\tau), t - \tau] \end{aligned} \quad (3)$$

In addition, for uncambered airfoils (consistent with NLWAKE restrictions), both the deficiency function and static lift-curve slope are even functions of  $\alpha$ . Furthermore, except for possible bifurcation points, both terms on the right side of Eq. (3) are expected to be analytic. Thus, expanding them in Taylor series about zero of angle of attack, retaining only even powers of alpha, Eq. (3) becomes

$$\begin{aligned} C_{L\alpha}[\alpha(\xi); t - \tau] &\approx C_{L\alpha}[\alpha(\tau), t - \tau] \\ &= C_{L\alpha}(0, \infty) + 0.5 \frac{\partial^2}{\partial \alpha^2} [C_{L\alpha}(0, \infty)] \alpha^2(\tau) + \dots \\ &\quad - F_0(0, t - \tau) - 0.5 F_2(0, t - \tau) \alpha^2(\tau) + \dots \end{aligned} \quad (4)$$

where

$$F_0(0, t - \tau) = F[\alpha(\tau), t - \tau] \big|_{\alpha(\tau) = 0}$$

and

$$F_2(0, t - \tau) = \frac{\partial^2}{\partial \alpha^2} \{ F[\alpha(\tau), t - \tau] \} \big|_{\alpha(\tau) = 0}$$

$C_{L\alpha}(0, \infty)$  and  $F_0(0, t - \tau)$  are the classical linear terms because they are independent of onset conditions. Note that if additional onset parameters are included, multivariate Taylor series will be required and mixed partial derivatives will appear.

$F_2$  was computed from NLWAKE step responses at steady-state onset conditions of  $\pm 1.0$  deg and is shown in Fig. 6. Figure 4 shows the comparison between steps initiated at 4.0-deg alpha as calculated directly from NLWAKE and as

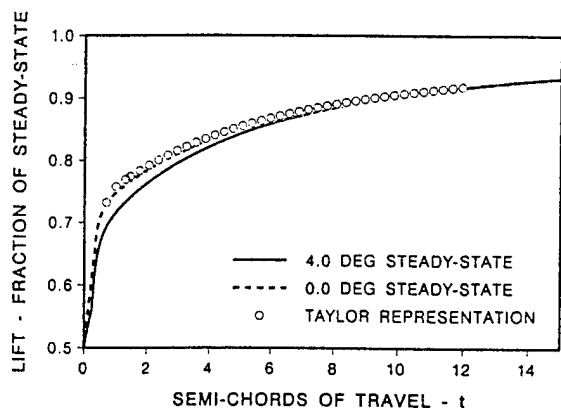


Fig. 4 Onset angle-of-attack effect on step response.

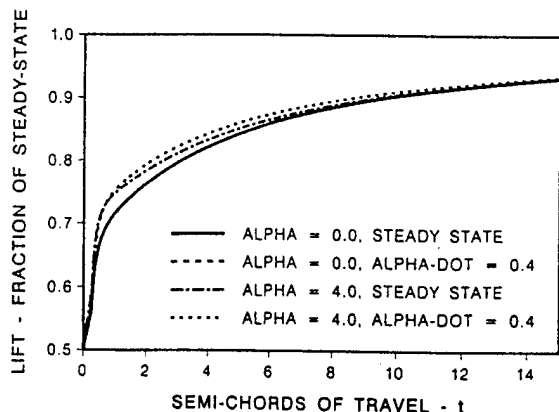


Fig. 5 Onset rate effect on indicial response.

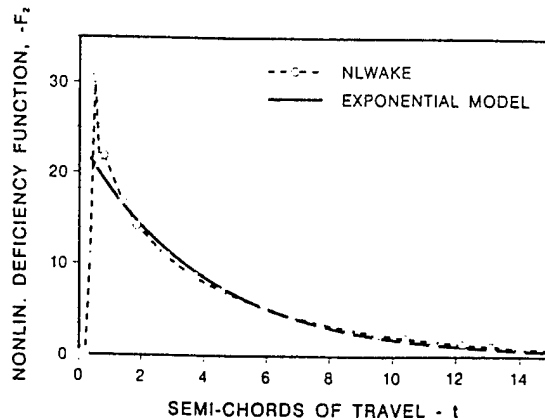


Fig. 6 Alpha-squared contribution to step response.

given by Eq. (4), dropping all terms higher than second order and retaining only the linear lift-curve slope. This is nearly an exact representation, and higher-order terms are not needed.

When Eq. (4) is used to construct lift responses to arbitrary inputs, as discussed in the following section, various integrals of  $F_0$  and  $F_2$  will be required. To this end, it is useful to have analytical models for each. Exponential approximations for the two-dimensional airfoil linear deficiency function abound in the literature. Jones' expression, as given by Fung,<sup>5</sup> is used herein. An exponential approximation for  $F_2$ , based on a least-squares fit to NLWAKE data, is shown in Fig. 6. These approximations are of the form:

$$F_0 \approx a_1 e^{-a_2 \tau_1} + (\pi - a_1) e^{-a_3 \tau_1} \quad (5a)$$

$$F_2 \approx b_1 (1 - e^{-b_2 \tau_1}) e^{-b_3 \tau_1} \quad (5b)$$

where  $a_1 = 1.037$  (1/rad),  $a_2 = 0.0455$ ,  $a_3 = 0.300$ ,  $b_1 = -148.3$  (1/rad<sup>3</sup>),  $b_2 = 24.9$ , and  $b_3 = 0.254$ .

Equation (4) is the nonlinear indicial response form used throughout the remainder of the paper; principal limitations on its use are the following:

- 1) Reference motions must be analytic. Indicial response functionals can then be represented as functions of onset motion parameters.
- 2) The indicial responses are assumed to approach a steady-state condition as elapsed time since onset becomes large.
- 3) In quantitative results, terms above second order in  $\alpha$  have been neglected based on comparisons with NLWAKE output (see Fig. 4). This has been justified only for attached-flow conditions and results are implicitly restricted to a relatively small angle-of-attack range.
- 4) The deficiency function and the static lift-curve slope have been expanded in Taylor series about  $\alpha = 0$  and a symmetric airfoil is considered; only even terms are retained. This leads to a simpler presentation and clearly shows that the classical linear theory is contained as a special case. Both terms can be expanded about nonzero values of  $\alpha$ , if desired.

### Response to Arbitrary Motion

#### Superposition Integral

As shown by Tobak and Chapman,<sup>1</sup> responses to arbitrary motion inputs can be calculated by using a generalized superposition integral. If a bifurcation in the steady-state response occurs at  $t = \tau_c$ , the integral has the form

$$C_L(t) = C_L[t, \alpha(0)] + \lim_{\epsilon \rightarrow 0} \left\{ \int_0^{\tau_c - \epsilon} C_{L_s}[\alpha(\xi); t, \tau] \frac{d\alpha}{d\tau} d\tau + \int_{\tau_c + \epsilon}^t C_{L_s}[\alpha(\xi); t, \tau] \frac{d\alpha}{d\tau} d\tau + \Delta C_L(t, \alpha_c) \right\} \quad (6)$$

where

$$\Delta C_L(t; \alpha_c) = C_L[\alpha(\xi); t, \tau_c + \epsilon] - C_L[\alpha(\xi); t, \tau_c - \epsilon]$$

Thus, the superposition integral is split to allow the solution to change discretely to a new equilibrium state (and to avoid the singularity). Since NLWAKE cannot support an investigation of hysteresis effects, it is assumed that no bifurcations take place over the time interval 0 to  $t$ . In this case, integration can proceed directly from  $\tau = 0$  to  $\tau = t$  and  $\Delta C_L = 0$ .

#### Simplified Forms

Approximating the nonlinear functional by Eq. (4) (dropping terms above second order) and changing the variable of integration to elapsed time from onset  $\tau_1 = t - \tau$ , Eq. (6)

becomes

$$C_L(t) = C_L[t, \alpha(0)] + C_{L_s}(0, \infty)[\alpha(t) - \alpha(0)] + C_{L_{ss}} \frac{\alpha^3(t) - \alpha^3(0)}{6} - \int_0^t F_0(0, \tau_1) g_0(t - \tau_1) d\tau_1 - 0.5 \int_0^t F_2(0, \tau_1) g_2(t - \tau_1) d\tau_1 \quad (7)$$

where

$$C_{L_{ss}} = \frac{\partial^2}{\partial \alpha^2} [C_{L_s}(0, \infty)], \quad g_0 = \dot{\alpha}, \quad g_2 = \alpha^2 \ddot{\alpha}$$

If Eq. (7) is used for dynamic analyses, the equations of motion become integro-differential equations because  $g_0$  and  $g_2$  appear under the integrals. Further simplification would be needed to avoid this complication. For linear systems, Etkin<sup>6</sup> proposed using "aerodynamic transfer functions" in conjunction with the Laplace transform of the equations of motion. One possible approach to the nonlinear problem is to represent Eq. (7) in the frequency domain by using higher-order Laplace transforms and George's association of variables technique (see Ref. 7). There would be, then, a potentially manageable algebraic problem with advantages similar to Etkin's linear system approach.

The objective here is limited to developing relationships between indicial response parameters and the response to arbitrary, but prescribed, motion. To this end, the integrals

$$\int_0^t F_i(\tau_1) g_i(t - \tau_1) d\tau_1; \quad i = 0, 2$$

may be integrated recursively by parts to give

$$\int_0^t F_i(\tau_1) g_i(t - \tau_1) d\tau_1 = g_i(0) I_{i1}(t) - g_i(t) I_{i1}(0) + \dot{g}_i(0) I_{i2}(t) - \dot{g}_i(t) I_{i2}(0) + \dots - \frac{d^{n-1}}{dt^{n-1}} [g_i(t)] I_{in}(0) + R_{i,n} \quad (8a)$$

where

$$I_{in}(t) = \int \dots \int_n F_i(\tau_1) d\tau_1 \dots d\tau_n \Big|_{\tau_1 = t} \quad (8b)$$

$$I_{in}(0) = \int \dots \int_n F_i(\tau_1) d\tau_1 \dots d\tau_n \Big|_{\tau_1 = 0} \quad (8c)$$

$$R_{i,n} = \int_0^t I_{in}(\tau_1) \frac{d}{d\tau_1^n} [g_i(t - \tau_1)] d\tau_1 \quad (8d)$$

Differentiability of  $g_0$  and  $g_2$  imposes no new restrictions since Eq. (2) requires  $\alpha(t)$  to have derivatives of all orders.

Finally, a series representation for the lift response to an arbitrary, but *specified*, motion input (in the absence of bifurcation) is given by substituting Eq. (8a) back into Eq. (7):

$$C_L = C_{L_{ss}} \ddot{\alpha}(t) + C_{L_s}(0, \infty) \alpha(t) + C_{L_{ss}} \frac{\alpha^3(t)}{6} + \sum_{n=0}^{\infty} \left( I_{n+1}(0) \left[ \frac{d^n g_0}{dt^n}(t) \right] - I_{n+1}(t) \left[ \frac{d^n g_0}{dt^n}(0) \right] + 0.5 \left\{ J_{n+1}(0) \left[ \frac{d^n g_2}{dt^n}(t) \right] - J_{n+1}(t) \left[ \frac{d^n g_2}{dt^n}(0) \right] \right\} \right) \quad (9)$$

where a steady-state initial condition has been assumed and

$$I_n = I_{0n} \quad \text{and} \quad J_n = I_{2n}$$



Note that an apparent mass term  $C_{L_{am}}\dot{\alpha}(t)$  must be included to account for the noncirculatory part of the lift response. The incompressible apparent mass reaction is instantaneous; therefore, the indicial response requires an impulse at step onset. Neither  $F_0$  nor  $F_2$  includes the impulse. However, it can be included as a Dirac delta function embedded in the indicial response representation.<sup>8</sup> Subsequent integration across the delta function produces an apparent mass term proportional to the instantaneous value of alpha dot. In the linear compressible case, Leishman<sup>9</sup> gives exponential models for the noncirculatory terms.

Note also on the right side of Eq. (9) the top line (apparent mass excluded) gives the quasisteady response. The last two lines account for the transition from the initial quasisteady state to the steady-state condition; i.e.,  $I_n(t)$  and  $J_n(t)$  describe the transient response and vanish for large  $t$ .  $I_n(0)$  and  $J_n(0)$  provide the dynamic response.

If a bifurcation in possible steady-state solutions occurs inside the time interval, the superposition integral must be split in accordance with Eq. (6). The integration procedure outlined earlier remains valid; the impact will be felt in two ways. First, by definition, static lift-curve slope terms will differ on each side of the bifurcation (corresponding changes in the deficiency functions are expected). Second, because  $\tau_c$  appears in the limits of integration (and in  $\Delta C_L$ ), terms like  $g_i(t - \tau_c)I_{in}(\tau_c)$  will appear. Since, for arbitrary motion,  $\tau_c$  is not known a priori, the time-domain solution becomes awkward for flight mechanists. Aerodynamic reaction models, as proposed by Hanff,<sup>10</sup> avoid this difficulty.

#### Properties of the Series Representation

Equation (9) has the distinct advantage of separating motion variables from indicial function characteristics. More specifically, the integrals are now independent of motion input; i.e., only multiple integrals of  $F_0$  and  $F_2$  are required. This property leads directly to the desired relationships between specific indicial response onset parameters, stability derivatives, and steady-state response to oscillatory motion inputs. However, simplification has been obtained at the cost of generality. Properties of both series (linear effects given in terms of  $I_n$  and nonlinear effects given in terms of  $J_n$ ) are examined later.

First, a special word of caution is in order. It may be tempting to use Eq. (9), retaining higher-order terms to improve accuracy, directly in dynamic analyses. Even in the linear case, this can lead to disastrously false results. The reason is that expansion of the integrals alters the nature of the characteristic equation, changing it from transcendental to polynomial. Each additional term contains higher-order time derivatives and therefore increases the polynomial's degree. Inevitably, extraneous roots are introduced. Spurious roots can occur in awkward places (well into the right-half plane, for example) even if the approximation is quite good within the radius of convergence. For a discussion of this problem see Ref. 11 and the references cited therein. To reiterate, Eq. (9) is introduced simply as an analytical tool for studying relationships among indicial response characteristics and responses to prescribed motions such as those encountered in wind-tunnel testing.

Both series in Eq. (9) are asymptotic expansions [of the left side of Eq. (8a)] with respect to sequences defined by taking successive time derivatives of  $g_0$  and  $g_2$ . This implies that they are valid for "sufficiently slow" motions, as will be shown for the special case of harmonic oscillations about a constant mean angle of attack. The motion also has an arbitrary phase angle relative to a reference signal:

$$\alpha(t) = \alpha_0 + A \cos(kt + \phi) \quad (10a)$$

$$g_0(t) = -Ak \sin(kt + \phi) \quad (10b)$$

$$g_2(t) = -k \{ B_3 \sin[3(kt + \phi)] + B_2 \sin[2(kt + \phi)] + B_1 \sin(kt + \phi) \} \quad (10c)$$

where

$$B_1 = [A(4\alpha_0^2 + A^2)]/4, \quad B_2 = A^2\alpha_0, \quad B_3 = A^3/4$$

Now consider the sequences of functions

$$g_{i,n} = \frac{d^n}{dt^n} [g_i(t)]; \quad i = 0, 2 \quad (11)$$

where  $n = 0, 1, 2, 3, \dots$

The right side of Eq. (8a) is an asymptotic expansion if  $g_{i,n}$  is an asymptotic sequence and  $R_{i,n}$  is  $o(g_{i,n-1})$ ; that is, if

$$\lim_{k \rightarrow 0} \frac{g_{i,n+1}}{g_{i,n}} = 0 \quad \text{and} \quad \lim_{k \rightarrow 0} \frac{R_{i,n}}{g_{i,n-1}} = 0 \quad \text{for all } n \quad (12)$$

General expressions for  $g_{0,n}$  and  $g_{2,n}$  can be obtained by putting Eqs. (10b) and (10c) into Eq. (11). Similarly,  $I_n$  and  $J_n$  are evaluated by repeated integration of Eqs. (5a) and (5b) in accordance with Eqs. (8b) and (8c). Proof that the series satisfy Eq. (12) is then straightforward. For example, when  $n$  is odd,  $g_{2,n-1}$  is

$$k^n (3^n - 1) B_3 \sin 3\Omega + 2^{n-1} B_2 \sin 2\Omega + B_1 \sin \Omega$$

and the dominant terms of  $R_{2,n}$  vary with frequency as

$$\frac{k^{n+1} \cos 3\Omega}{k^2 + f_1}, \quad \frac{k^{n+1} \cos 2\Omega}{k^2 + f_2}, \quad \frac{k^{n+1} \cos \Omega}{k^2 + f_3}$$

where

$$\Omega = kt + \phi$$

Note that  $f_1$ ,  $f_2$ , and  $f_3$  are independent of  $k$ . Since  $\Omega$  approaches  $\phi$  in the limit, the nonlinear terms are easily shown to satisfy Eq. (12). A similar argument holds for even values of  $n$ .

The most important property of asymptotic expansions is that their partial sums have an error of the same order as the first term omitted. For all values of  $n$ , Eq. (12) guarantees that the error can be made arbitrarily small as  $k$  approaches zero. However, the quality of the approximation depends on the convergence properties of the series for fixed  $k$ . If partial sums decrease initially, useful approximations can be obtained even if the series ultimately diverge. Thus, the question of establishing a frequency limit for practical applications is best answered by examining the behavior of the first few terms.

To this end, steady-state lift response characteristics for an airfoil oscillating about zero mean angle of attack were computed. Motion variables are given by Eqs. (10a-c) with  $\alpha_0 = 0$ . There can be no response at the first harmonic frequency  $2k$  since  $B_2 = 0$  in this case.

Approximate lift responses were computed from Eq. (9) with  $I_n(0)$  and  $J_n(0)$  defined by Eqs. (5a), (5b), and (8c). Both  $I_n(t)$  and  $J_n(t)$  were set to zero since only the steady-state solution was desired. Corresponding exact steady-state solutions were computed directly from Eq. (7) also using Eqs. (5a) and (5b) for  $F_0$  and  $F_2$ , respectively. Nonlinearity in the quasisteady lift curve was neglected in both cases.

Partial sums of the series expansions, normalized by corresponding exact solutions, are presented in Figs. 7-9. In keeping with traditional dynamic testing practice, in-phase (cosine) and out-of-phase (sine) components are presented separately because they can be associated with static and dynamic stability derivatives. (Splitting the series is permissible, as the sum of two asymptotic expansions is also asymptotic, provided they are defined with respect to the same sequence.)

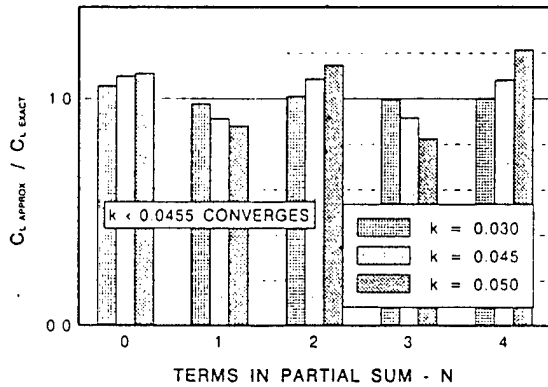


Fig. 7 Linear in-phase series convergence.

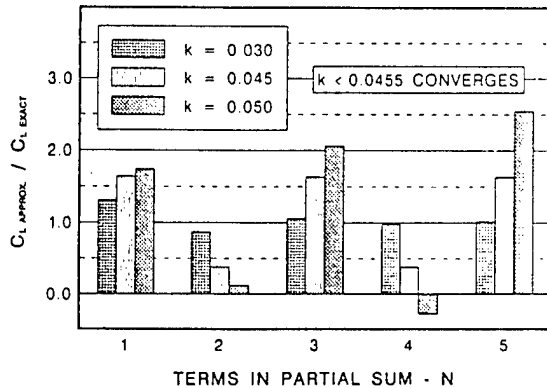


Fig. 8 Linear out-of-phase series convergence.

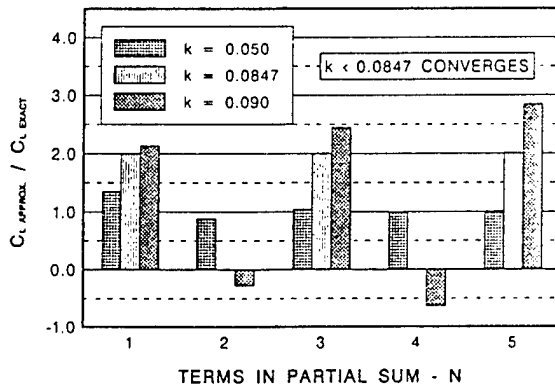


Fig. 9 Second harmonic in-phase series convergence.

Figure 7 shows partial sums representing the linear in-phase component as a function of frequency and the number of terms retained. Only the static lift-curve slope is included at  $N=0$ , while  $I_{2g,1}$  is added for  $N=1$ , and so on. As determined by the ratio test, series for the linear components converge for  $k < a_2 = 0.0455$ . Thus, characteristics just below, at, and just above the convergence frequency are illustrated. Asymptotic behavior is evident; accuracy is improved at any  $N$  as frequency decreases. At frequencies above the convergence frequency, however, the partial sums diverge immediately. If only the quasisteady term is retained, common practice for rigid-body dynamics, errors on the order of 10 and 11% will be incurred at reduced frequencies of 0.045 and 0.050, respectively. Finally, the static lift-curve slope is within 6% and convergence is rapid (to about 2% with one additional term) at the lowest frequency of 0.03.

Convergence properties for the linear out-of-phase components are shown in Fig. 8 and are quite similar to the linear in-phase component. Greater percentage errors for the initial term (31, 64, and 74% in order of increasing frequency) are expected since there is no quasisteady term common to both exact and approximate results.

Properties for the nonlinear in-phase contribution at  $3k$  are displayed in Fig. 9. In this case, divergence occurs at frequencies above  $3k = b_3 = 0.254$ . Therefore, computations were carried out at reduced frequencies of 0.050, 0.0847, and 0.090 to include the highest frequency shown for the linear case and to overlap the convergence frequency. Again, divergence is immediate outside the radius of convergence. At  $k = 0.050$  convergence is relatively fast, to within about 4% in three terms; however, the initial error is surprisingly high (35%) considering that this frequency is well removed from the divergence boundary of 0.0847.

Similar results could be shown for the remaining nonlinear contributions; but the point is that the series diverge for frequencies greater than the slowest varying exponential involved in the corresponding indicial response. That is, if for large  $t$ , the indicial response varies as  $e^{-at}$ , then the convergence frequency is given in terms of the indicial response time constant by

$$kT = 1$$

where

$$T = 1/a$$

For responses at harmonics of the forcing function, the harmonic frequency is to be used.

#### Relationship to Stability Derivatives

As Etkin<sup>12</sup> has shown, the conventional stability derivative representation can be derived easily from the premise that the aerodynamic reactions are functionals of the vehicle state variables. Two assumptions are required:

- 1) The motion is an analytic function of time.
- 2) Aerodynamic reactions are *analytic* functions of the instantaneous state variables and their time derivatives.

The first assumption allows the functional to be replaced by an ordinary function of the state variables and their derivatives; the second permits a multivariate Taylor series expansion of the function in terms of its arguments. The coefficients of the series are the classic stability derivatives. Only the linear terms are usually retained for small perturbation analyses; however, nonlinear derivatives are sometimes included. Alternatively, nonlinear effects can be included by treating the derivatives as functions of the variables.

Similarities between Etkin's development and the derivation of Eq. (4) are apparent. The significant difference is that the latter is an approximation to a functional representing the nonlinear indicial response rather than one representing the total response. In the absence of bifurcation, putting Eq. (4) into the superposition integral gives the total response to an analytic motion input, Eq. (7). In this section, the asymptotic approximation to Eq. (7), given by Eq. (9), is used to briefly examine the implicit limits of the stability derivative approach. First, to gain physical insight, Eq. (9) is used to replicate a previous result derived by Tobak and Schiff<sup>2</sup> for the case of slowly varying harmonic oscillations about constant mean values.

Recall that the infinite series in Eq. (9) are expansions for the left side of Eq. (8a) (with  $i=0$  and  $i=2$ , respectively) and that  $I_n(t)$  and  $J_n(t)$  tend to zero as  $t$  goes to infinity. Thus, taking a sufficiently large  $t$ , say  $t_a$ , and retaining only the leading terms ( $n=0$ ) of the series:

$$\begin{aligned} & \int_0^{t_a} F[x(t-\tau_1), \tau_1] \dot{x}(t-\tau_1) d\tau_1 \\ & \approx \int_0^{t_a} F[x(t_a-\tau_1), \tau_1] \dot{x}(t_a-\tau_1) d\tau_1 \\ & \approx -\dot{x}(t_a) [I_1(0) + 0.5J_1(0)x^2(t_a)] \end{aligned} \quad (13)$$

Comparing the last two lines of Eq. (13), the integral is dominated by the region near the lower limit ( $\tau_1 = 0$ ). This is to be expected on physical grounds since small  $\tau_1$  corresponds to the recent past and the asymptotic nature of the series requires the motion to be slow in some sense. This suggests that in the integrand  $\tau_1$  can be neglected compared to  $t_a$ , i.e.,

$$\int_0^{t_a} F[x(t_a - \tau_1), \tau_1] \dot{\alpha}(t_a - \tau_1) d\tau_1 \approx \dot{\alpha}(t_a) \int_0^{t_a} F[x(t_a), \tau_1] d\tau_1 \quad (14)$$

Finally, recalling that  $I_1(t_a)$  and  $J_1(t_a)$  are negligible and

$$F[x(t_a), \tau_1] = F_0(0, \tau_1) + 0.5F_2(0, \tau_1)\alpha^2(t_a)$$

the last lines of Eqs. (13) and (14) are easily shown to be identical.

Thus, to first order, lift due to  $\alpha$  dot is proportional to the area under the deficiency function *evaluated at the instantaneous angle of attack*, and thus

$$C_{L_z}[x(t)] = - \int_0^{t_a} F[x(t_a), \tau_1] d\tau_1 = I_1(0) + 0.5J_1(0)\alpha^2(t_a)$$

In keeping with the spirit of the Taylor series interpretation of the stability derivative concept, the following definitions are perhaps preferable:

$$C_{L_z} = I_1(0)$$

$$C_{L_{zzz}} = 0.5 \frac{\partial^3 C_{L_z}}{\partial \alpha^3} = 0.5J_1(0)$$

Of course, additional information is obtained by including higher-order terms in the series expansions. For example, the second-order terms reveal that  $\alpha$ -double-dot effects are related to the second integral of the deficiency function again evaluated at  $\alpha(t_a)$ , as shown by Eqs. (15):

$$C_{L_z} = I_2(0) \quad \text{and} \quad C_{L_{zzz}} = 0.5J_2(0) \quad (15)$$

However, both an additional term and an unexpected identity appear:

$$2C_{L_{zzz}} \equiv C_{L_{zzzz}} = 0.5J_2(0)$$

Thus, dynamic stability derivatives and the dynamic terms of the asymptotic expansions, terms involving  $I_n(0)$  and  $J_n(0)$ , are intimately related. When the asymptotic approximation to the superposition integral breaks down, the stability derivative concept does also. For harmonic motion and deficiency function forms given by Eqs. (5a) and (5b), this occurs at frequencies at or above the largest indicial function time constant as shown in the preceding section. When nonlinearities introduce harmonics, the harmonic frequency should be compared to the time constant for the corresponding nonlinear component of the deficiency function.

### Relationship to Steady-State Oscillatory Data

Direct measurement of nonlinear indicial responses is difficult at best. Furthermore, suitable parameter identification techniques to extract them from experimental data have not been discussed in the literature. However, an assessment of the usefulness of approximating the indicial-response functional in terms of onset parameters [Eq. (4)] needs to be accomplished for more general cases than studied here. The limited objective of identifying significant onset parameters from steady-state oscillatory data is discussed in this section.

Consider again a harmonic oscillation about a constant mean angle of attack, given by Eq. (10a). Substituting Eqs. (10b) and (10c) into Eq. (9), the steady-state lift response has the form

$$C_L = C_{L_0} = G_1 \cos \Omega + G_2 \cos 2\Omega + G_3 \cos 3\Omega + H_1 \sin \Omega + H_2 \sin 2\Omega + H_3 \sin 3\Omega \quad (16)$$

The time-invariant response arises from nonzero values of  $\alpha_0$  and is simply the average of the maximum and minimum quasisteady lift values:

$$C_{L_0} = \alpha_0 \{ [(2\alpha_0^2 + 3A^2)/12] C_{L_{zzz}} + C_{L_z}(0, \infty) \}$$

From Eq. (9), it can be shown that all of the in-phase contributions,  $G_1$  through  $G_3$ , are power series in  $k$  and contain a frequency independent quasisteady term. For example,

$$G_1 = A \{ C_{L_z}(0, \infty) - I_2 k^2 + I_4 k^4 - \dots \} + (B_1/2) \{ C_{L_{zzz}} - J_2 k^2 + J_4 k^4 - \dots \} \quad (17a)$$

$$G_2 = (B_2/4) \{ C_{L_{zzz}} - 4J_2 k^2 + 16J_4 k^4 - \dots \} \quad (17b)$$

where  $I_n$  and  $J_n$  are evaluated at  $\tau_1 = 0$ .

The out-of-phase components are similar except that the leading terms are first order in frequency and, as expected, contain no quasisteady terms; e.g.,

$$H_2 = -(B_2/2)k \{ J_1 - 4J_3 k^2 + \dots \} \quad (17c)$$

Now, suppose that additional terms are needed in Eq. (4) to represent adequately the indicial response. For example, if onset rate is important and its effect varies linearly with angle of attack, terms proportional to  $\alpha$  dot and the product of  $\alpha$  and  $\alpha$  dot should be considered. That is, two additional series are introduced in Eq. (9) involving the motion variables:

$$g_3(t) \equiv \dot{\alpha}^2 \quad \text{and} \quad g_4(t) \equiv \alpha \dot{\alpha}^2$$

From Eq. (10a),  $g_3$  contributes a time-invariant term and a first harmonic. Similarly,  $g_4$  contributes a constant term and components at the fundamental, first, and second harmonic frequencies. Thus, including these terms leaves the form of Eq. (16) undisturbed; however, its coefficients ( $G_1, H_1$ , etc.) then contain contributions from each of the  $g_i$ . As shown in Eqs. (17a-c), the effects of  $A$  and  $\alpha_0$  are separable from frequency effects; i.e., they may be written in the form

$$G_j = G_{0,j} c_{0,j} + G_{2,j} c_{2,j} + G_{3,j} c_{3,j} + G_{4,j} c_{4,j} \quad (18)$$

where

$$G_{i,j} = G_{i,j}(A, \alpha_0), \quad c_{i,j} = c_{i,j}(k); \quad j = 1, 2, 3$$

and  $i$  corresponds to onset parameter  $g_i$ .

Individual effects due to each of the three nonlinear  $g_i$  on mean lift  $G_{i,j}$  and  $H_{i,j}$  are summarized in Table 1. Note that each onset parameter has a unique signature and a test matrix can be designed to accentuate the differences.

Table 1 Influence of onset parameters

Coefficient	$g_2$	$g_3$	$g_4$
$C_{L_0}$	0	$A^2$	$A^2 \alpha_0$
$G_1, H_1$	$A^3 + 4A^2 \alpha_0$	0	$A^3$
$G_2, H_2$	$A^2 \alpha_0$	$A^2$	$A^2 \alpha_0$
$G_3, H_3$	$A^3$	0	$A^3$

Given a candidate set of onset parameters, the identification problem consists of solving for the unknown  $c_{i,j}$  on the right side of Eq. (18). Thus, a relatively simple harmonic analysis of data obtained by conventional techniques is sufficient to identify active onset parameters. Finally, note that this analysis requires no assumptions about the *form* of deficiency-function time history. It *does* assume, however, that no bifurcations occur within the test range and requires that the series in Eq. (9) converge.

### Concluding Remarks

Earlier, the nonlinear indicial response was introduced by Tobak, Chapman, and Schiff as a means of modeling aerodynamic responses in nonlinear flight mechanics problems. They have also suggested possible simplifications based on relating indicial response to motion variables (and their derivatives) evaluated at step onset.

In this paper, the implications of using a Taylor series expansion (with respect to onset parameters) of the deficiency function are examined. A particularly simple expansion is shown to be applicable to thin two-dimensional airfoils with wake distortion nonlinearities. Furthermore, given the series approximation to the indicial response, the generalized superposition integral can be approximated by an asymptotic expansion, valid for sufficiently slow motions. For harmonic motion, the expansions diverge for frequencies greater than the slowest varying exponential involved in the corresponding deficiency function. The combined approximations, for the indicial response function and for the superposition integral, lead directly to relationships between conventional stability derivatives and indicial response characteristics. In the absence of bifurcation, these relationships can be used to identify dominant onset parameters from steady-state oscillatory force and moment data.

Further work is needed, especially concerning bifurcation of steady-state responses to step inputs due to their importance to aerodynamic hysteresis. The usefulness of representing the indicial response as a function of onset motion parameters depends on obtaining sufficient accuracy with a

very limited number of terms. Assessments based on experimental data at realistic reduced frequencies should be made.

### Acknowledgments

Support for this work from the Air Force Office of Scientific Research is gratefully acknowledged. The author is also indebted to J. E. McCune for providing the NLWAKE code and to G. M. Graham for the use of his data.

### References

- <sup>1</sup>Tobak, M., and Chapman, G. T., "Nonlinear Problems in Flight Mechanics Involving Aerodynamic Bifurcations," *Unsteady Aerodynamics—Fundamentals and Applications to Aircraft Dynamics*, AGARD CP-386, Paper 25, May 1985.
- <sup>2</sup>Tobak, M., and Schiff, L. B., "Aerodynamic Mathematical Modeling—Basic Concepts," AGARD Lecture Series 114, Paper 1, March 1981.
- <sup>3</sup>Graham, G., and Yeow, K., "Two-Dimensional Post Stall Maneuver of a NACA 0015 Airfoil at High Pitching Rates," AIAA Paper 90-2810, Aug. 1990.
- <sup>4</sup>Scott, M. T., and McCune, J. E., "Nonlinear Aerodynamics of Two-Dimensional Airfoils in Severe Maneuver," AIAA Paper 88-0129, Jan. 1988.
- <sup>5</sup>Fung, Y. C., *An Introduction to the Theory of Aeroelasticity*, Dover, New York, 1969, p. 207.
- <sup>6</sup>Etkin, B., *Dynamics of Atmospheric Flight*, Wiley, New York, 1972, pp. 165–168.
- <sup>7</sup>Rugh, W. J., *Nonlinear System Theory*, Johns Hopkins Univ. Press, Baltimore, MD, 1981, pp. 53–73.
- <sup>8</sup>Etkin, B., *Dynamics of Flight*, Wiley, New York, 1959, pp. 181, 182.
- <sup>9</sup>Leishman, J. G., "Validation of Approximate Indicial Aerodynamic Functions for Two-Dimensional Subsonic Flow," *Journal of Aircraft*, Vol. 25, No. 10, 1988, pp. 914–922.
- <sup>10</sup>Hanff, E. S., "Dynamic Nonlinear Airloads Representation and Measurement," *Unsteady Aerodynamics—Fundamentals and Applications to Aircraft Dynamics*, AGARD CP-386, Paper 27, May 1985.
- <sup>11</sup>Tobak, M., "On the Minimization of Airplane Responses to Random Gusts," NACA TN-3290, Oct. 1957.
- <sup>12</sup>Etkin, B., *Dynamics of Atmospheric Flight*, Wiley, New York, 1972, pp. 158, 159.

# **Body-Axis Rolling Motion Critical States of a 65-Degree Delta Wing**

Jerry E. Jenkins, James H. Myatt, Ernest S. Hanff

Reprinted from

## **Journal of Aircraft**

Volume 33, Number 2, Pages 268-278



*A publication of the*  
American Institute of Aeronautics and Astronautics, Inc.  
370 L'Enfant Promenade, SW  
Washington, DC 20024-2518

# Body-Axis Rolling Motion Critical States of a 65-Degree Delta Wing

Jerry E. Jenkins\* and James H. Myatt†

U.S. Air Force Wright Laboratory, Wright–Patterson Air Force Base, Ohio 45433-7531  
and

Ernest S. Hanff‡

Institute for Aerospace Research, Ottawa, Ontario K1A 0R6, Canada

Dynamic wind-tunnel test results of a 65-deg swept delta wing are reviewed. These tests involved body-axis rolling motions at moderate (15- to 35-deg) angles of attack in both the Institute for Aerospace Research 2 × 3 m low-speed wind tunnel and the 7 × 10 ft Subsonic Aerodynamic Research Laboratory facility at Wright–Patterson Air Force Base. They included static, forced oscillation, and free-to-roll experiments with flow visualization. Multiple trim points (attractors) for body-axis rolling motions and other unusual dynamic behavior were observed. These data are examined in light of the nonlinear indicial response theory. The analysis confirms the existence of critical states with respect to roll angle. When these singularities are encountered in a dynamic situation, large and persistent transients are induced. Conventional means of representing the nonlinear forces and moments in the aircraft equations of motion, notably the locally linear model, are shown to be inadequate for these cases. Finally, the impact of these findings on dynamic testing techniques is discussed.

## Nomenclature

- $b$  = wingspan, ft
- $C_l, C_m$  = body-axis rolling moment and pitching moment coefficients, nondimensionalized with respect to  $qSb$  and  $qS\bar{c}$ , respectively
- $C_{l,dyn}$  = dynamic rolling moment coefficient,  $C_l(t) - C_{l,stat}$
- $C_{l,stat}$  = static rolling moment coefficient, i.e., equilibrium  $C_l$  corresponding to the instantaneous value of roll angle
- $C_{l,\alpha}(t)$  = nonlinear rolling moment indicial response, due to step input in roll angle
- $\bar{c}$  = mean aerodynamic chord, ft
- $k$  = reduced frequency,  $\omega b/2U_\infty$
- $q$  = freestream dynamic pressure, lb/ft<sup>2</sup>
- $Re$  = Reynolds number
- $S$  = wing area, ft<sup>2</sup>
- $t$  = time, s
- $U_\infty$  = freestream velocity, ft/s
- $x_{vb}$  = vortex breakdown position, fraction of root chord aft of wing vertex
- $\xi$  = running time variable denoting motion history,  $-\infty \leq \xi \leq \tau, s$
- $\sigma$  = total angle of attack, body-axis inclination with respect to  $U_\infty$ , deg
- $\tau$  = time at step onset, s
- $\phi$  = body-axis roll angle, deg
- $\phi_0$  = initial roll angle for free-to-roll experiments, also mean roll angle for harmonic motion experiments
- $\omega$  = circular frequency, rad/s

## Introduction

**D**YNAMIC coupling between aircraft motion and aerodynamic forces and moments acting on the aircraft is at the heart of stability and control. Maintaining sufficient fidelity in aerodynamic models for these interactions has become an increasingly difficult problem in the face of flight envelope expansion.

A theoretical method for studying the nonlinear aspects of the flight dynamics problem has been under development by Tobak<sup>1</sup> and his colleagues since the 1960s. Their initial approach<sup>2</sup> introduced two important new concepts: 1) a nonlinear indicial response and 2) a generalized superposition integral. As with linear indicial response methods, the idea is to represent aerodynamic responses (force or moment) due to arbitrary motion inputs as a summation of responses to a series of step motions. The nonlinear indicial response, as opposed to its linear counterpart, accounts for changes induced by the motion history leading up to step onset.

Subsequently, results from the growing body of nonlinear dynamical system theory were used to greatly strengthen the model.<sup>3,4</sup> The key idea of these extensions has been to accommodate the existence of critical states, i.e., specific values of the motion variables where discrete changes in static aerodynamic behavior occur. These are singular points that require special handling in the superposition integral. Critical states are important because potentially large and persistent transient aerodynamic effects can be anticipated when an aircraft encounters them in a dynamic situation.

Truong and Tobak<sup>5</sup> have also demonstrated that, for static aerodynamic characteristics that are time invariant, the nonlinear indicial response, together with the generalized superposition integral, can be derived directly from the Navier–Stokes equations. Thus, the theory has a sound mathematical basis and captures the flow physics as well. There is still much work to be done, especially for cases involving time-dependent equilibrium states. Nevertheless, the theory is rich in its ability to represent a wide range of important aerodynamic nonlinearities that can be encountered in maneuvering flight.

Independently, Hanff<sup>6</sup> proposed the reaction hypersurface model. As opposed to the time-domain indicial response model, the hypersurface is expressed in terms of a set of in-

Presented as Paper 93-0621 at the AIAA 31st Aerospace Sciences Meeting, Reno, NV, Jan. 11–14, 1993; received Sept. 14, 1994; revision received Aug. 29, 1995; accepted for publication Aug. 31, 1995. This paper is declared a work of the U.S. Government and is not subject to copyright protection in the United States.

\*Aerospace Engineer, WL/FIGC 2210 Eighth Street, Suite 21. Senior Member AIAA.

†Aerospace Engineer, WL/FIGC 2210 Eighth Street, Suite 21. Member AIAA.

‡Senior Research Officer, Applied Aerodynamics Laboratory. Member AIAA.

dependent variables consisting of the instantaneous values of the motion variables and their time derivatives. It was, at its inception, designed to be experimentally based and primarily intended for simulations of aircraft motion in nonlinear settings where the classical stability derivative approach breaks down.<sup>7</sup> More recent work<sup>8</sup> has been aimed at establishing the theoretical connection between the reaction hypersurface and nonlinear indicial response models.

Experiments designed to study either of these mathematical models demand a dynamic test capability that can efficiently collect the necessary nonlinear and time-dependent data. A large-amplitude high-rate roll oscillation system,<sup>9</sup> developed at the Canadian Institute for Aerospace Research (IAR), meets this requirement.

Hanff and Jenkins<sup>10</sup> used this rig to study the roll dynamics of both a 65-deg delta wing and an 80–65-deg double-delta wing at the IAR. Their experiments produced some extremely interesting results that require further explanation.

The 65-deg delta wing configuration was found to have multiple stable trim points in roll (depending on roll-axis inclination) as reported by Hanff and Ericsson.<sup>11</sup> Locations for these attractors are repeated here in Table 1. They argue (based on analysis of static rolling-moment data at  $\sigma = 30$  deg) that asymmetric vortex breakdown, induced by differing effective sweep angles on each wing panel, is the root cause. However, the dynamic behavior observed in free-to-roll experiments is harder to explain, although Hanff and Huang<sup>12</sup> have shown that the instantaneous loads are largely driven by the dynamics of leading-edge vortex breakdown.

In free-to-roll tests, the model is given an initial roll displacement, then released by disengaging a remotely actuated clutch. The model is then free to roll about its body axis, restrained only by a small amount of bearing friction in this degree of freedom. The inertia of the moving system was adjusted to ensure that the free-to-roll responses were in the same frequency range as the dynamic force measurements (about 7.7 Hz, see Table 2). Since frequency is inversely proportional to the reference length at fixed flight speed, corresponding full-scale vehicle frequencies are realistic.

Two free-to-roll time histories for the 65-deg configuration at  $\sigma = 30$  deg, plotted in the phase plane, are shown in Fig. 1. Note that the trajectory for the  $-58.3$ -deg release angle (solid curve) finds the stable equilibrium point at about 0-deg roll, while the 53.1-deg release angle trims at about 21 deg. Both trajectories pass quite close to attractors (21 and 0 deg, respectively) with very low rates, but do not trim there. This behavior was highly repeatable. Furthermore, the trajectories intersect at several points. Similar intersections of phase-plane trajectories (for wing-rock motions) have been observed only

when vortex breakdown occurs over the wing.<sup>13</sup> Clearly, some phenomenon, not explicitly accounted for in the two-dimensional phase-plane representation, affects the motion. Persistent motion history effects, perhaps related to vortex breakdown dynamics, that require more than a knowledge of the instantaneous roll angle and roll rate are a strong possibility.

Finally, forced-oscillation motions about a zero mean roll angle produce distinctly different rolling-moment responses than those measured for motions with mean roll angles of 7 deg or greater.<sup>10</sup> An analysis of the static and dynamic force data<sup>8</sup> suggested that this behavior can be explained by the existence of critical states. Indeed, large transient effects (with the magnitudes of the static and dynamic effects being of the same order) were noted in the response following encounters with the suspected critical states. These transients persist for at least a quarter cycle at  $k = 0.08$ .

Follow-on tests, designed to investigate the cause of the behavior noted earlier, were conducted in the Subsonic Aerodynamic Research Laboratory (SARL) wind tunnel at Wright-Patterson Air Force Base. An analysis of the static, dynamic, free-to-roll, and flow visualization data taken during these experiments is presented later. Relevant aspects of critical-state theory are discussed and data confirming the existence of roll-motion critical states are presented. The impact on dynamic testing techniques (including data collection and reduction) and application to the simulation and analysis of the flight dynamics problem are addressed in this article's final sections.

### SARL Experiments

IAR's high-amplitude, high-rate roll apparatus was also used in the SARL tests. A comprehensive experimental program involving over 800 runs was conducted using the 65-deg delta-wing configuration (Fig. 2). The test matrix is summarized in Table 2.

Since SARL is an open-return atmospheric tunnel, the IAR Mach number, Reynolds number, and reduced frequencies could not be matched simultaneously. However, test conditions were chosen to match those at the IAR as closely as possible. In addition, the model support systems and tunnel cross-section geometry are quite different in the two tunnels. Thus, the

Table 1 Roll attractor locations	
Angles, deg	
Sting	Roll
20	0
25	$\pm 1.5$
30	0, $\pm 21$
35	$\pm 11$
40	0

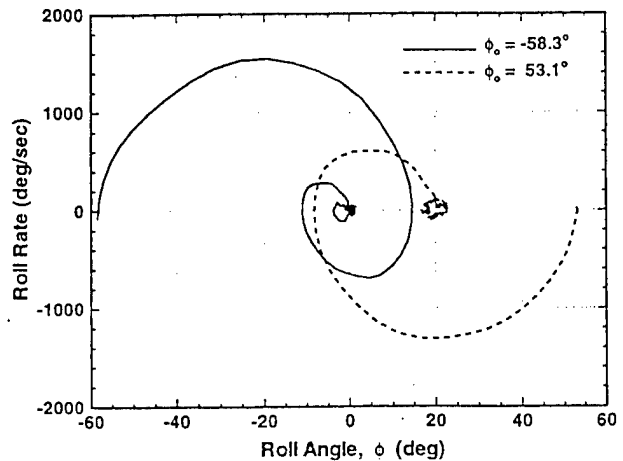


Fig. 1 Free-to-roll motions:  $\sigma = 30$  deg.

Table 2 SARL test conditions

Test type	Roll offset, deg	Amplitude, deg	Frequency, Hz	Total angle of attack, deg
Static force	-70–70	NA	NA	15, 30, 35
Dynamic force	0–42	5–40	1.1, 4.4, 7.7	15, 30, 35
Free-to-roll	-65–65	NA	7.7	30, 35
Flow visualization	0–42	5–40	0, 1.1, 4.4, 7.7	30, 35
Surface pressure	0–42	5–40	0, 1.1, 2.2, 4.4, 7.7	15, 30, 35

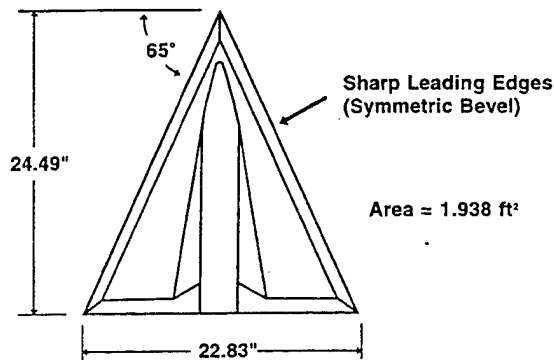


Fig. 2 Model geometry.

very good facility-to-facility repeatability eliminated the possibility of significant support and wall interference effects.

Dynamic force and moment measurements were taken with the model forced in constant amplitude harmonic motion. Data were taken at 4.4 and 7.7 Hz ( $k = 0.08$  and  $0.14$ ) to match IAR conditions. These results closely tracked static measurements except when the motion passed through small roll angles.<sup>8</sup> Thus, in the SARL experiments, dynamic tests were also conducted at 1.1 Hz ( $k = 0.02$ ) to determine how the extremely large dynamic effects, incurred at small roll angles, approach quasisteady behavior at low reduced frequency.

Laser-sheet flow visualization data and unsteady surface pressure measurements were also taken. Thus, an extensive data set was created that allows a coordinated study of vortex dynamics (including breakdown) and the resulting unsteady aerodynamic forces and moments.

Free-to-roll experiments were also repeated in the SARL tunnel. These data provide an independent check on the accuracy of the dynamic force measurements (and the mathematical model used to represent them) since the measured forces, together with the known model and test-rig inertia, can be used to predict the free-to-roll motion.

### Critical States, Theoretical Basis

A development of the nonlinear indicial response and critical states<sup>1,3,4</sup> is beyond the scope of this article. However, some key results, pertinent to the present discussion, are summarized:

1) The nonlinear indicial response (NIR) is represented mathematically as a functional to incorporate the motion history effect.

2) The NIR is a derivative, called the Fréchet derivative, of the functional representing an aerodynamic response in terms of its motion history. It is the limit, as step height goes to zero, of the incremental response (due to the step input) divided by step height. Following Tobak's notation,<sup>1</sup> the rolling moment due to an infinitesimal step in roll angle is written

$$C_l(t) = C_{l,\phi}[\phi(\xi); t, \tau]$$

where square brackets denote a functional; the first argument is the independent function defining the motion history (roll angle in this case); and arguments following the semicolon give, respectively, the times at which 1) the response is to be evaluated (observed) and 2) the step motion was initiated.

Therefore, the function  $\phi(\xi)$  is to be interpreted as the motion history from  $t = -\infty$  to step onset  $\tau$ , and the motion is to be held constant at  $\phi(\tau)$  thereafter. The long-term behavior of the aerodynamic response functional (after transients due to the motion have died away) is called the equilibrium state.

3) If the Fréchet derivative exists everywhere on a time interval (i.e., for the range of motion variables encountered on that interval), the generalized superposition integral may be

used to construct the net aerodynamic response (rolling moment in this case) over the interval. Thus,

$$C_l(t) = C_l[\phi(\xi); t, 0] + \int_0^t C_{l,\phi}[\phi(\xi); t, \tau] \frac{d\phi}{d\tau} d\tau$$

Following the notation introduced previously, the first term on the right-hand side (RHS) is the rolling moment at time  $t$  resulting from the roll-angle variation  $\phi(\xi)$ , which is the motion history prior to  $\xi = \tau = 0$ , and is held constant at  $\phi(0)$  for all  $\xi \geq 0$ . The functional in the second term is the NIR, as defined earlier. In this case,  $\tau$  is the variable of integration and the time at step onset. Thus, the integral sums the effects of all indicial responses over the interval 0 to  $t$ .

4) If, on the other hand, there are specific points  $\tau_c$  within the interval where Fréchet differentiability is lost (at a critical state  $\phi_c$ ), the integration may not be carried beyond the instant at which a critical state is encountered without acknowledging the existence of the singularity.

5) Loss of Fréchet differentiability is handled by allowing the equilibrium response to change discretely to a new state. Thus, the integral must be split to isolate the critical state, i.e.,

$$C_l(t) = C_l[\phi(\xi); t, 0] + \int_0^{\tau_c - \epsilon} C_{l,\phi}[\phi(\xi); t, \tau] \frac{d\phi}{d\tau} d\tau + \int_{\tau_c + \epsilon}^t C_{l,\phi}[\phi(\xi); t, \tau] \frac{d\phi}{d\tau} d\tau + \Delta C_l(t, \phi_c) \quad (1)$$

where

$$\Delta C_l(t, \phi_c) = C_l[\phi(\xi); t, \tau_c + \epsilon] - C_l[\phi(\xi); t, \tau_c - \epsilon] \quad (2)$$

$\Delta C_l$ , as given by Eq. (2), is the transient response associated with  $\phi_c$ . Note that it depends on the motion history from  $-\infty$  to just beyond  $\tau_c$ . However, its effect persists for times  $t > \tau_c$ .

6) Fréchet differentiability may be lost in several ways.<sup>1</sup> A very important case is when time-invariant equilibrium flows lose their analytic dependence on a motion parameter (body-axis roll angle in these experiments). There are at least two ways this can happen, both involving an exchange of stability among competing equilibrium flows:

a) Static aerodynamic responses (i.e., responses corresponding to solutions of the time-invariant form of the Navier-Stokes equations) can develop a fold at a critical value of the motion parameter, possibly an indirect result of a subcritical bifurcation. The response slope becomes infinite at the fold, invalidating the Fréchet derivative. Note that a subcritical bifurcation requires the existence of multiple (nonunique) steady-state solution curves on both sides of the parameter's critical value.<sup>14</sup> However, there is an exchange of stability among the available branches at the critical value. The initial or basic solution becomes unstable when the parameter is greater than the critical value. Any perturbation will force a transition to a new (and stable) equilibrium flow. The transition is seen as a discontinuous jump when plotted vs the motion parameter; however, its time history is given by Eq. (2).

b) Static aerodynamic responses can experience a supercritical bifurcation at a critical value of the motion parameter. Response-curve slopes become discontinuous at such points, again invalidating the Fréchet derivative. Nonunique steady-state solution curves are required in this case also.<sup>14</sup> The apparent discontinuous jump in slope is caused by a transition from the unstable basic solution to an intersecting (stable) equilibrium-solution curve as the motion parameter passes through the critical value. In general, the intersecting solution curves are smooth.



7) Changes in flow topology (a change in the number of singular points in either the external flow or in skin-friction lines) when the motion parameter reaches a critical value may signal the loss of Fréchet differentiability. Tobak et al.<sup>1</sup> anticipate that equilibrium responses could cease to be analytically dependent on the motion parameter at such points. They also state that there could also be "a significant increase in the time required for the ... response to reach a new equilibrium state."

NIR theory, as outlined previously, is used extensively to interpret the new experimental results. However, there are important restrictions implicit in the analysis. Static force data have been time averaged to remove the effects of model and/or sting vibrations, freestream fluctuations, etc., and also to stay within the NIR theoretical framework (which in its current form requires time-independent equilibrium states). Furthermore, the relationship between time-averaged force and moment behavior and topology changes in the corresponding mean flow deserves closer scrutiny since it is highly desirable to have definitive experimental evidence pointing to critical state locations. Therefore, the potential impact of time-averaging and mean-flow topology changes are examined in the following section. This is done by using a well-known flow as an example. In this case, the parameter controlling the flow-field evolution is Reynolds number (as opposed to an evolution with respect to a motion variable as discussed earlier).

### Flow About a Cylinder

Consider the two-dimensional flow about a circular cylinder at Reynolds numbers ranging from zero to values beyond the onset of vortex shedding. As  $Re$  is increased from zero, the force balance (initially between only pressure and viscous forces) must accommodate the increasing effects of inertial forces. At very low Reynolds numbers, the flow remains fully attached to the cylinder (as shown in Fig. 3a); the flowfield topology is characterized by two half-saddle points<sup>15</sup> located at the fore and aft stagnation points on the plane of symmetry. A separation bubble appears at  $Re \approx 7$  (based on the cylinder diameter) as shown in Fig. 3b. Associated with the bubble are three half-saddle points on the surface (an increase of two) plus a saddle point in the downstream flowfield that provides closure for the bubble. In addition, there are two nodes (degenerate foci, also called centers) that account for the closed streamlines within the bubble. Thus, both flows (with and without the standing eddies) conform to the topological rule<sup>15</sup> for the flow in a planar slice through a body:

$$\left( \sum_N + \frac{1}{2} \sum_S \right) - \left( \sum_S + \frac{1}{2} \sum_N \right) = -1$$

where  $\sum_N$  and  $\sum_S$  denote the number of nodes and saddle points, respectively, in the flowfield and  $\sum_N$  and  $\sum_S$  are the number of half-nodes and half-saddle points on the body surface, respectively.

Thus, there is a distinct change in flowfield topology at  $Re \approx 7$  (going from two topological singularities to a total of seven, including three off-surface singularities). However, the changeover is perfectly smooth. There are no competing (non-unique) equilibrium solutions for  $7 < Re < 50$ ; i.e., the topological change does not involve a flowfield instability and the possibility of a supercritical bifurcation must be ruled out. However, the appearance of separated flow behind the cylinder implies the existence of reverse-flow velocity profiles that are more susceptible to instability.

At a  $Re \approx 50$ , the flow within the bubble does become unstable and vortex shedding begins. The resulting equilibrium flow is time periodic, but there is a time-invariant mean flow. Numerous calculations for the steady flow in this  $Re$  range have been published.<sup>16</sup> However, experiments by Nishioka and Sato<sup>17</sup> (Fig. 4) clearly show that the separation bubble corre-

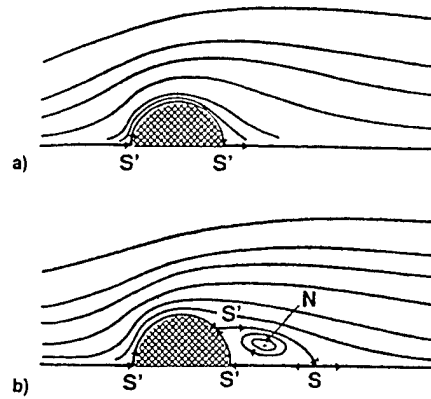


Fig. 3 Steady flow about a cylinder: a) attached flow,  $Re < 7$  and b) with separation bubble,  $Re > 7$ .

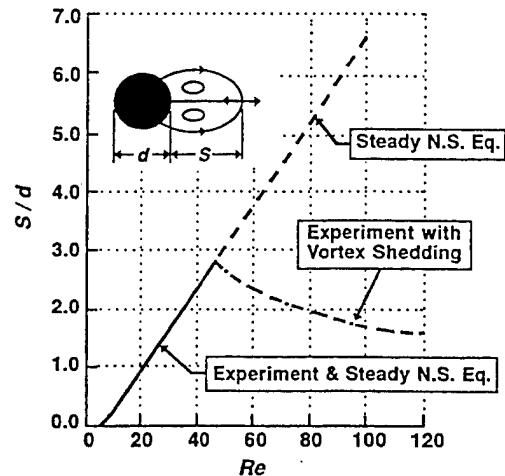


Fig. 4 Separation bubble length vs  $Re$  with and without unsteady vortex shedding.

sponding to the time-invariant mean flow when vortex shedding is present is very much shorter than it would have been in the absence of fluctuations. Furthermore, the change in bubble length begins abruptly at the critical  $Re$  (corresponding to the onset of shedding), and entails a discontinuous slope with respect to  $Re$ . A corresponding discontinuous change in the slope of the integrated load, i.e., the mean drag, should also be expected.

Note that there has been no change in the number and types of topological singularities present in the mean flow at  $Re \approx 50$  (although significant changes in topology are evident if the flowfield is frozen at any instant). Thus, two time-invariant equilibrium solutions are available above  $Re \approx 50$ , corresponding to the cases with and without vortex shedding. Therefore, the onset of a time-periodic equilibrium condition is seen as a supercritical bifurcation of the mean flow wherein the long bubble solution loses its stability. However, there is no corresponding change in mean-flow topology.

Recent computations by Chen et al.<sup>18</sup> strongly support the notions that 1) there are no bifurcations associated with the appearance of the separation bubble and 2) loss of stability in the steady flow, through a Hopf bifurcation, is associated with the onset of unsteady vortex shedding.

Thus, the conclusions are as follows:

1) Under normal conditions (only one equilibrium solution) a change in mean-flow topology cannot imply a loss of Fréchet differentiability; i.e., there is no corresponding critical state.

2) Supercritical bifurcations of the mean flow can occur (a critical state) without a coincident change in mean-flow topology when the equilibrium flow becomes time dependent.

3) The significance of a topological change in the mean flow is that if inflexible velocity profiles are created, then the resulting mean flow is more susceptible to instability.

These observations having been made, the discussion now returns to the rolling delta wing.

### Experimental Evidence

Based on the theory presented previously, aerodynamic data in the presence of critical states should exhibit the following traits:

1) Static (fixed vehicle attitude) flow visualization studies may show a change in flow structure at a critical state. If the visualization technique implicitly involves time averaging (e.g., oil-flow studies of skin-friction lines), a topology change is neither necessary nor sufficient for the existence of a critical state. However, a mean-flow topology change can indicate a susceptibility to instability and may be closely associated with a subsequent critical state, especially if flowfield variables (such as pressure gradient) are highly sensitive to small changes in the parameter.

2) Static force and moment data should exhibit nonanalytic behavior across critical states; i.e., there should be a discontinuity in the variation of the force data and/or their derivatives with respect to the motion variable if the equilibrium flow is time invariant. The discontinuity is located at the critical state. If the equilibrium response is not time invariant, a discontinuity may still be apparent in the mean (time-averaged) loads, as in the example presented earlier. This latter possibility is a likely consequence of the basic flow becoming unstable, thereby sending the unsteady equilibrium solution on a new and stable path.

3) Transient effects should be observed following dynamic critical-state encounters. The transient,  $\Delta C_i$  in Eqs. (1) and (2), will in general depend on motion history.

SARL data (for the rolling 65-deg delta wing) pertinent to each attribute are discussed later. All data discussed here were taken at the same condition (0.3 Mach number and  $\sigma = 30$  deg). For these discussions, the term static refers to the model being held fixed (within normal experimental constraints) with respect to the freestream and does not imply a time-invariant equilibrium state. All measurements taken under static conditions are time-averaged unless explicitly stated to be otherwise.

### Static Flow Structure

Equilibrium vortex breakdown locations for the left wing as a function of static roll angle, from Hanff and Huang,<sup>12</sup> are shown in Fig. 5. (For positive roll angles, the left wing is on the lee side; i.e., it has been rolled away from the freestream velocity vector. Conversely, it is the windward wing for neg-

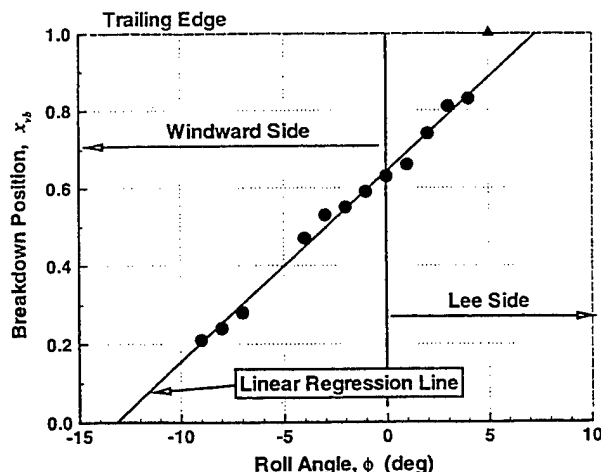


Fig. 5 Time-averaged vortex breakdown position: left wing panel,  $\sigma = 30$  deg.

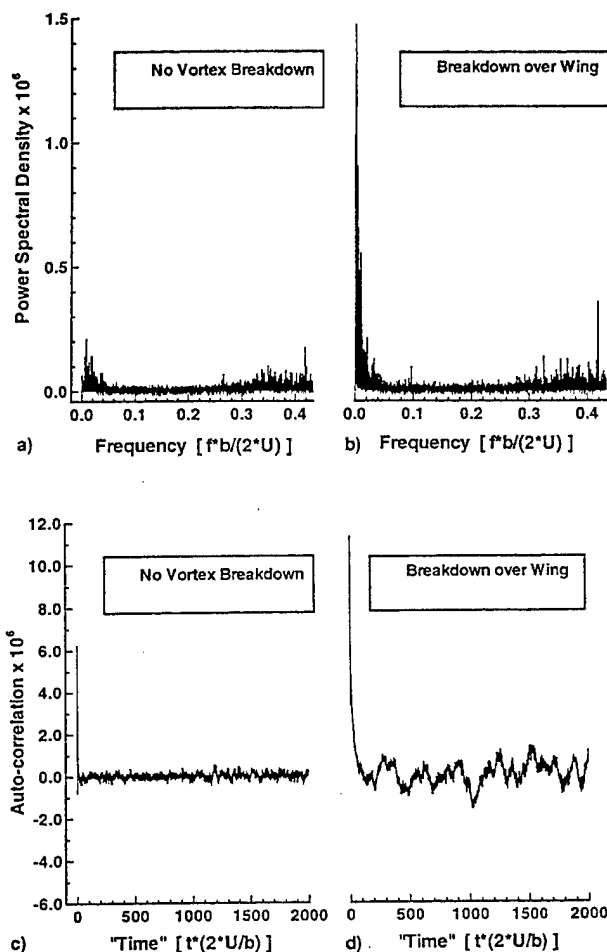


Fig. 6 Rolling-moment coefficient power spectral density: a)  $\phi = 20$  and b) 5 deg; and rolling moment coefficient autocorrelation: c)  $\phi = 20$  and d) 5 deg.

ative roll angles.) The solid line is a linear least-square-error fit to the circular data points (correlation coefficient 0.996). Note that the experimental point at  $\phi = 5$  deg (triangle) departs significantly from the linear fit. Thus, in agreement with Hanff and Huang's interpretation of Wentz's<sup>19</sup> data, breakdown location is seen to be a nonlinear (perhaps discontinuous) function of static roll angle in the 4- to 5-deg range. For  $\phi$  greater than 5 deg the breakdown point is well aft of the trailing edge. In addition, vortex breakdown reaches the vertex at about  $\phi = -13$  deg, as suggested by the linear extrapolation. When the leading-edge vortex structure on both wings is considered, the conditions  $|\phi| \approx 5$  and 13 deg are candidate critical states.

The first,  $|\phi| \approx 5$  deg, may be a critical state principally because a discontinuous rearward shift of the breakdown point on the lee wing would cause a jump (increase) in the equilibrium lifting pressures on that side (aft of about 80% chord from Fig. 5). Any discontinuities in the forces (or their derivatives) with respect to  $\phi$  would, of course, invalidate the Fréchet derivative. Time-averaged static force data supporting this view are discussed later.

Secondly,  $|\phi| \approx 13$  deg is almost certainly a critical state because, if the breakdown point reaches the vertex, the stagnation point in the vortex-core axial flow<sup>20</sup> is lost. The precise roll angle where this occurs is unknown due to flow visualization difficulties that require an extrapolation of the data to the apex. However, the breakdown point will unquestionably reach the vertex for a sufficiently large roll angle.

### Static Force and Moment Behavior

Unsteady aerodynamic force and moment measurements, taken under static conditions where vortex breakdown is ab-

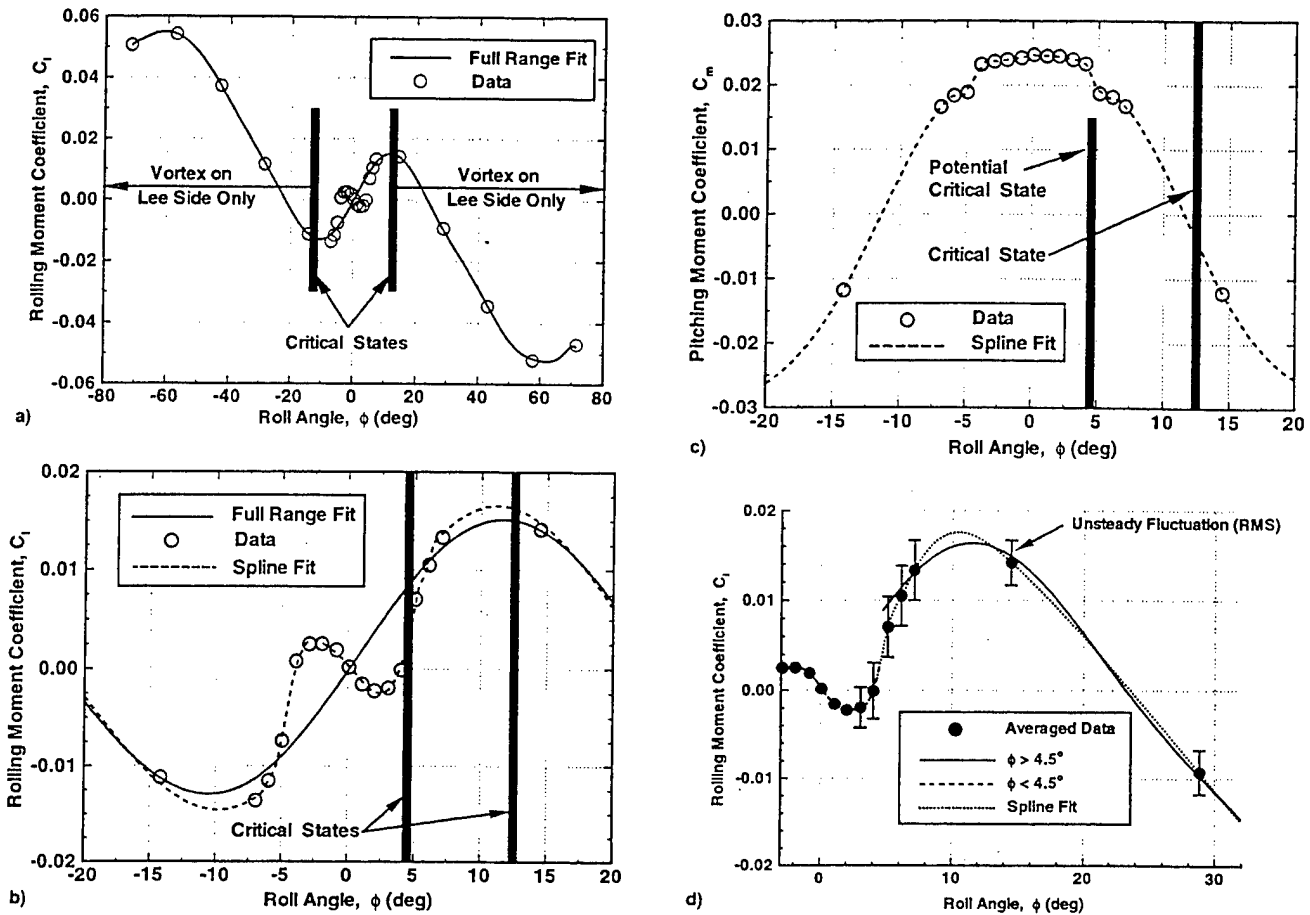


Fig. 7 a) Static (time-averaged) rolling-moment coefficient data,  $\sigma = 30^\circ$ ; b) full-range polynomial fit to rolling-moment data:  $\sigma = 30^\circ$ ,  $|\phi| < 20^\circ$ ; c) time-averaged pitching-moment coefficient data:  $\sigma = 30^\circ$ ,  $|\phi| < 20^\circ$ ; and d) polynomial fits for the ranges  $|\phi| < 4.5^\circ$  and  $|\phi| > 4.5^\circ$ .

sent, are characterized by relatively small, broad-band, random fluctuations about a well-defined mean value. (Mean values calculated for overlapping 13-s samples repeat quite well.) Power-spectral density (PSD) and autocorrelation plots for the rolling-moment coefficient for such a case ( $\sigma = 30^\circ$ ,  $\phi = 20^\circ$ ) are presented in Figs. 6a and 6c. When vortex breakdown is near the trailing edge of the left wing and at about 40% root chord on the right wing,  $\sigma = 30^\circ$  and  $\phi = 5^\circ$ , there is a marked increase in the low-frequency content of the PSD (Fig. 6b), i.e., for nondimensional frequencies,  $f b / (2U_\infty)$ , less than about 0.04. As a result, the rms value of the fluctuations goes from 0.0025 to 0.0033 (a 32% increase) and the autocorrelation, Fig. 6d, takes on a distinctly quasiperiodic appearance.

Time-averaged static rolling-moment coefficient vs. roll angle is presented in Fig. 7a. Also shown are the critical states locations corresponding to the loss of a coherent vortex on the windward wing (breakdown reaches the vortex). The degree of unsteadiness, in terms of the rms value of the fluctuations about the mean, is shown by error bars in Fig. 7d.

If critical states exist in the roll-angle range tested, then the function representing the rolling moment (or any other force/moment) cannot be analytic. Given only values for a function at a discrete number of points, it is impossible to prove that it is (or is not) an analytic function. However, a cursory investigation of its behavior is worthwhile.

If a function is analytic it can be represented by a Taylor series. Therefore, a stepwise regression analysis was used to look for a polynomial (least-squares fit) representing  $C_l$  as a function of  $\phi$  since the polynomial can be interpreted as a truncated Taylor series. Thirty-two terms (each an odd Legendre polynomial<sup>21</sup>) were included in the list of possible contrib-

utors to the regression equation. Test data points were interpolated (with a cubic spline) at 255 points distributed in a geometric sequence beginning at the origin and increasing in either direction; i.e., the ratio of  $\phi_{i+1}$  to  $\phi_i$  was held constant. The proportionality constant between successive interpolation points was systematically varied such that intervals between successive points ( $\phi_{i+1} - \phi_i$ ) at the extremes ranged from 2 to 40 times the interval at the origin  $\phi_1 - \phi_0$ . This was done to give additional weight to points near the origin, where the rolling moment is rapidly varying, while keeping enough density at the extremes to prevent the polynomial from oscillating. Values between 30–40 were used in the final results discussed later.

The solid curve (labeled Full Range Fit) in Fig. 7a is the polynomial fit over the complete roll-angle range. Thirteen terms were included in the final regression equation; the rest were rejected because they offered no improvement in the correlation. Note that the stable trim point at  $\phi = 0^\circ$  was not captured despite the heavy emphasis given to points in this region (160 of 255 points were within  $|\phi| < 16^\circ$ ). However, this result may be influenced by a gap in test data coverage on either side of the critical state at about  $13^\circ$  (raising questions about the validity of the spline fit in this region). Further static testing is required to determine the actual behavior.

An expanded view of the region  $-20^\circ \leq \phi \leq 20^\circ$  is presented in Fig. 7b. Also shown is the cubic spline fit and the possible critical state at  $\phi \approx 5^\circ$  (from flow visualization results). Note the separation of data points for  $|\phi| \leq 4^\circ$  and for  $5^\circ \leq |\phi| \leq 7^\circ$ . Moreover, Fig. 7c (pitching moment vs. roll angle) reinforces the notion that there is a discontinuity between the two groups. Both effects, a nose

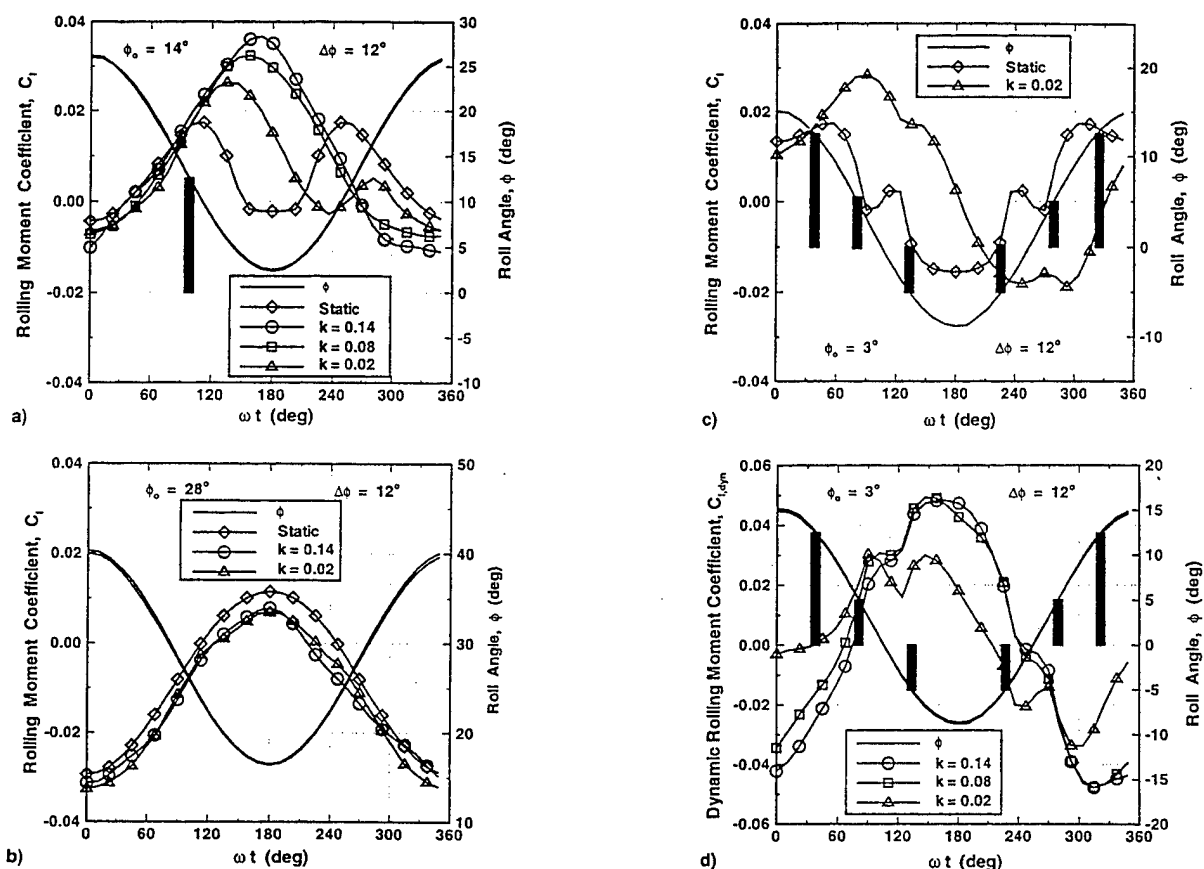


Fig. 8 Rolling-moment responses: harmonic motion, a) vertical bar denotes critical state, b) no critical state encounters, and c) vertical bars denote critical states; and d) dynamic rolling-moment responses: harmonic motion, vertical bars denote critical states.

down pitching moment increment and a positive (right wing down) rolling-moment increment as the roll angle increases from +4 to +5 deg, are consistent with the aft movement of the vortex breakdown point on the lee wing noted earlier.

Finally, as shown in Fig. 7d, considerable improvement in the polynomial fit is possible if the independent variable range is broken into regions and distinct polynomials are used for each of them. Interestingly, if breakpoints are included only at  $\phi = \pm 4.5$  deg to model apparent discontinuities there, the polynomial's slope at  $4.5^+$  deg contrasts sharply with test data at 5, 6, and 7 deg. An additional breakpoint for the critical state at approximately 13 deg would resolve this mismatch in slopes. In summary, the inability to perform polynomial fits (without breaking the interval into smaller pieces) supports the notion that critical states exist near the locations cited previously. Again, additional static data are needed to fully justify this conclusion.

Thus, for  $|\phi|$  decreasing through 5 deg (breakdown moving from the wake to a position over the wing), static flow visualization and force/moment data suggest that a change in flow topology is quickly followed by a subcritical bifurcation involving an oscillatory instability. (Chaderjian and Schiff's<sup>22</sup> computational results reinforce the view that there are large-scale fluctuations present in the equilibrium state.) However, as the vortex breakdown approaches the wing apex,  $|\phi| \approx 13$  deg, the bifurcation that occurs would appear to be supercritical.

#### Dynamic Forces and Moments

If the conditions outlined,  $|\phi| \approx 5$  and 13 deg, are indeed critical states, there may be discernible transients associated with them. A previous analysis<sup>8</sup> of IAR data suggested that at least one of these conditions contributed to significant dynamic effects. In this section, SARL rolling-moment measurements under dynamic conditions are examined for this behavior.

Recall that the dynamic data are steady-state responses to harmonic motion, i.e., starting transients have dissipated and the aerodynamic response for each cycle is identical. Thus, if time scales appropriate for the aerodynamic response are sufficiently large compared to the period of the motion, the measured responses represent an aggregate of effects that were initiated during earlier cycles. A significant frequency effect will be observed under these conditions. Furthermore, transient responses to single events occurring at discrete points during each cycle become apparent as the frequency of the motion is decreased.

Dynamic rolling-moment data taken for a 12-deg amplitude body-axis rolling motion, centered about a mean roll angle of 14 deg, is presented in Fig. 8a. The abscissa is the argument ( $\omega t$ ) of the cosine function that defines the motion. Thus, precisely one cycle of motion is presented regardless of frequency. Dynamic data taken at three reduced frequencies ( $k = 0.02$ , 0.08, and 0.14, respectively), are shown. In addition, the rolling-motion time history and static data (plotted as functions of the instantaneous roll angle) are presented for reference.

Note the dramatic differences in waveform between responses at the two highest reduced frequencies and the  $k = 0.02$  data (where distinct transients originating at critical states become more apparent). The critical-state encounter at an  $\omega t$  of about 95 deg (highlighted by the vertical bar) is readily discernable. However, later in the cycle, where transient effects overlap, a positive identification of distinct events is more difficult.

Significantly, responses for all three frequencies follow the static data closely for  $\omega t$  in the range 0 to about 95 deg ( $26 \text{ deg} \geq \phi \geq 13 \text{ deg}$ ), then depart from the static curve. In addition, dynamic responses at all frequencies approach the static value at the end of the cycle, the deviation increasing with frequency. Thus, the rolling-moment response appears to be essentially quasisteady when transients due to critical-state encounters have

had time to die out. This notion is supported by the data presented in Fig. 8b, which show static and dynamic rolling-moment data for 12-deg oscillations about a mean roll angle  $\phi_0$  of 28 deg. Roll angles traversed by this motion, 16–40 deg, preclude any encounters with suspected critical states. Differences between the static and dynamic data are likely within interpolation errors caused by the sparsely spaced static data in this region. Again, if there are no recent critical-state encounters, the rolling-moment behavior is quasisteady.

The situation shown in Fig. 8c is somewhat different; in this case, the motion (12-deg amplitude about a 3-deg offset) is centered between critical states. Therefore, the order, number, and elapsed times between encounters are different than those in Fig. 8a. Also, roll rates at  $|\phi| = 5$  deg are much higher than before (the converse is true at  $\phi = 12$  deg). Definite breaks in the rolling-moment response are evident at  $\phi = \pm 5$  deg. Again, a departure from quasisteady behavior is seen early in the cycle (at about  $\phi = 12$  deg).

When the static (equilibrium) flow is time-invariant, the NIR can be represented as the difference between its steady-state response and the deficiency function.<sup>2,23</sup> The deficiency function is defined as

$$F[\phi(\xi); t, \tau] = C_{l,\phi}[\phi(\xi); \infty, \tau] - C_{l,\phi}[\phi(\xi); t, \tau]$$

where, in this case, the steady-state part (first term on the RHS) is the derivative of the static rolling moment with respect to roll angle. (Also, the steady-state term on the RHS can be taken as the mean value of the static rolling-moment derivative when the equilibrium state is time dependent.)

Thus, the time-varying part of the NIR is represented by the deficiency function. When this form of the NIR is put into the superposition integral [Eq. (1)], the steady-state part integrates directly to give the change in the static coefficient between the limits of integration. Therefore, the steady-state parts of the initial condition,  $\Delta C_l$ , and the two integrals, sum to the instantaneous value for the static rolling-moment coefficient  $C_{l,stat}[\phi(t)]$ . Even in the nonlinear case, with critical states present, the total response under dynamic conditions may be separated into a static component (evaluated at the instantaneous roll angle) and a dynamic component.

The dynamic rolling moment coefficient  $C_{l,dyn}$  is shown in Fig. 8d for a roll-angle offset of a 3- and 12-deg amplitude (the same motion as Fig. 8c). Comparing Figs. 8c and 8d, note that the static and dynamic components are the same order of magnitude. Also, as shown in Fig. 8d, locations for critical states, identified from both static flowfield structure and static force behavior, correlate well with dramatic changes in the dynamic rolling-moment response.

The results discussed earlier for a limited number of motions apply over a wide range of test conditions as shown in Figs. 9a–9c. Each of these is a contour plot of the dynamic (total minus static) rolling-moment coefficient presented in the phase plane. Each represents  $k = 0.08$  data for the complete range of test amplitudes at a given roll-angle offset. A series of tests with fixed offset and frequency generates a family of ellipses, centered about the offset angle. As the rolling motion proceeds, the ellipses are traversed in the clockwise direction. Offsets for each of the figures are 0, 7, and 14 deg, respectively.

The contours were established by first finding a mathematical representation for the rolling-moment data. A regression procedure, similar to that reported in Ref. 8, was used to do this. A correlation coefficient of 0.97 was achieved for data covering all test conditions at  $k = 0.08$  and 0.14.

In all cases presented in Figs. 9a–9c, the contour lines turn rapidly, becoming essentially parallel to the roll-rate axis at  $\phi = \pm 5$  deg. Moving clockwise in the bottom half of the ellipse through  $\phi = -5$  deg, the contour lines again turn rapidly between  $-10$  and  $-15$  deg to run nearly parallel to the roll angle axis. Note that this turning point is less distinct than the first, perhaps because the static data have been faired

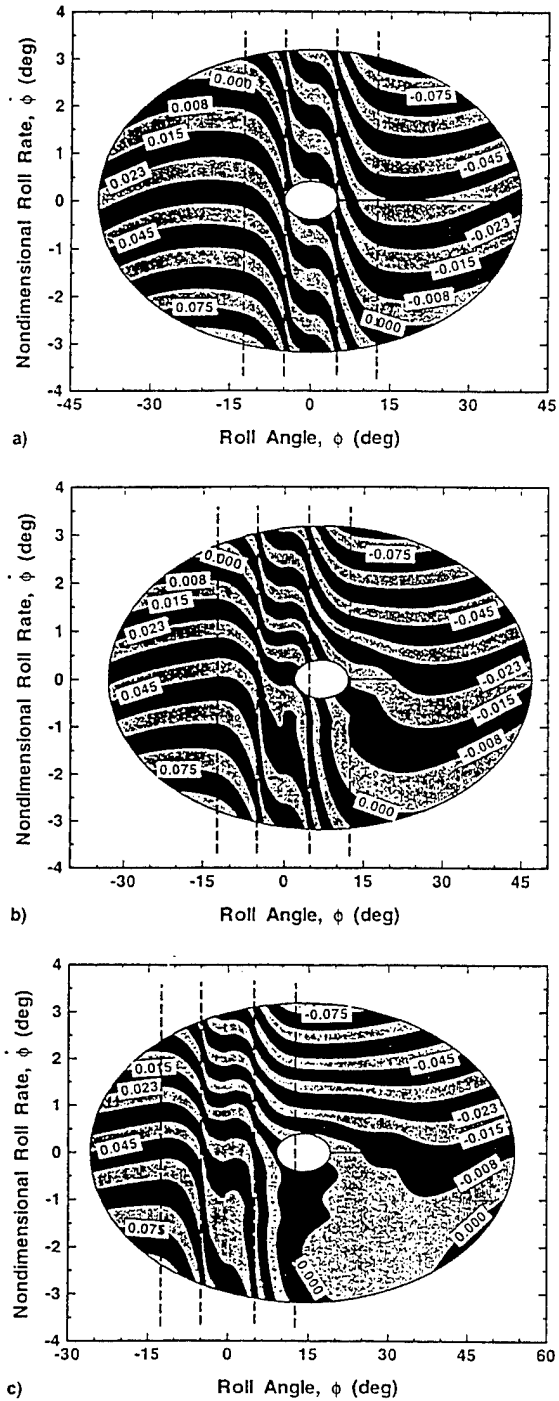


Fig. 9 Dynamic rolling-moment contours: a)  $k = 0.08$ ,  $\phi_0 = 0$  deg; b)  $k = 0.08$ ,  $\phi_0 = 7$  deg; and c)  $k = 0.08$ ,  $\phi_0 = 14$  deg.

through this region. The pattern repeats in the upper half of the figure. Significantly, the loci of turning points are independent of roll rate, further evidence that they are critical states because they are determined by equilibrium conditions.

Following a critical-state encounter, the dynamic response becomes weakly dependent on roll angle (contour lines nearly parallel to the roll-angle axis). Contours in this region are likely the result of expressing time variations implicitly in the phase plane (rather than an actual dependence on roll angle or roll rate).

Finally, note that as the offset roll angle is increased (allowing more time to elapse between the critical-state encounter near 13 deg with positive roll rate and the next 13-deg critical-state encounter with negative roll rate) the region of negligible

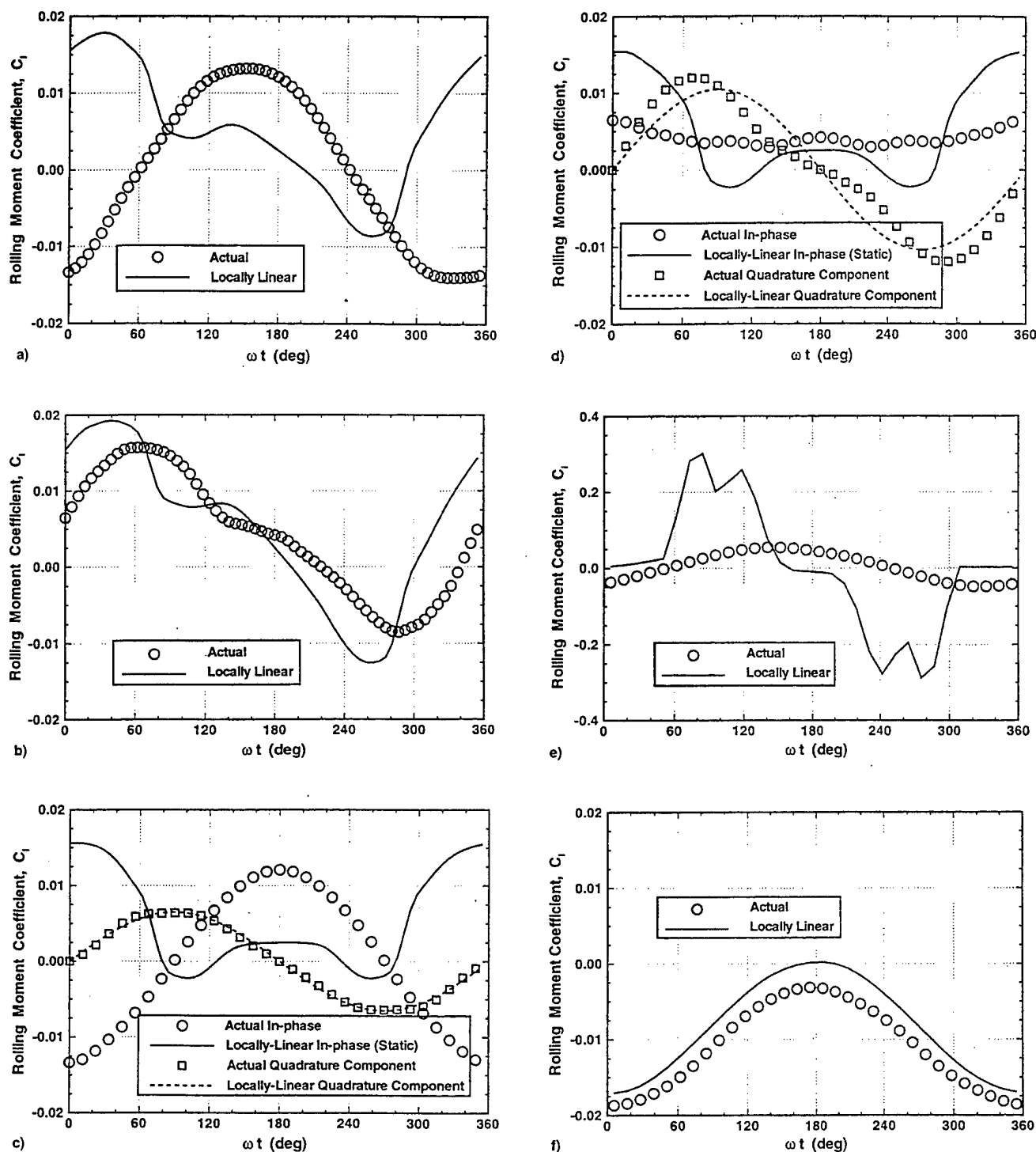


Fig. 10 Comparison between actual data and locally linear model: a)  $k = 0.14$ ,  $\phi_0 = 3$  deg, and  $\Delta\phi = 5$  deg and b)  $k = 0.02$ ,  $\phi_0 = 3$  deg, and  $\Delta\phi = 5$  deg; in-phase and quadrature component comparisons: c)  $k = 0.14$ ,  $\phi_0 = 3$  deg, and  $\Delta\phi = 5$  deg and d)  $k = 0.02$ ,  $\phi_0 = 3$  deg, and  $\Delta\phi = 5$  deg; e) effect of extrapolating low-frequency derivatives to high rates,  $k = 0.14$ ,  $\phi_0 = 3$  deg, and  $\Delta\phi = 18$  deg; and f) locally linear model vs actual data: no critical states,  $k = 0.14$ ,  $\phi_0 = 28$  deg, and  $\Delta\phi = 5$  deg.

dynamic rolling moment in the lower-right quadrant expands. There is more time for the transient to decay.

### Significance of Results

Locally linear models are often used to represent aerodynamic forces and moments in nonlinear flight simulations. In this model, static forces and moments are represented by nonlinear functions of instantaneous values of angle of attack and sideslip. Dynamic effects are calculated by using locally linear damping derivatives (linearized about the instantaneous

vehicle state). Dynamic nonlinearities are accounted for by allowing derivatives to be functions of angle of attack and sideslip.

Linearization of the testing technique used is often a consequence of the damping derivatives used to measure them. Small-amplitude harmonic vehicle motions are used and only the quadrature component of the loads at the frequency of the oscillation is considered. Although this procedure is acceptable in the absence of significant nonlinearities (as is the case in many small amplitude motions), it leads to results that cannot,

in general, be legitimately extrapolated in terms of rate, which is precisely what locally linear models do.

To check the validity of locally linear damping derivatives in the current case, forced oscillation data were reduced in this manner, i.e., nonlinear static rolling-moment data were used together with roll-damping derivatives, obtained from 5-deg amplitude tests at different offset angles.<sup>10</sup> Only the out-of-phase rolling moment at the forcing frequency was retained, although up to 20 harmonics were recorded. Thus, the result is a derivative linearized about the mean roll angle of the motion. The locally linear model was then used to predict the measured rolling moment (with all harmonics) over the same motion as used to determine the damping derivative.

Comparisons between the model and measured responses are shown in Figs. 10a–10f. In Figs. 10a–10d and 10f, the damping derivative is taken to be constant (consistent with the small amplitude, 5 deg, over which it was determined). However, in Fig. 10e the damping derivative was represented by a nonlinear function of roll angle (owing to the larger amplitude, 18 deg).

Figures 10a and 10b show results for  $\phi_0 = 3$  deg and reduced frequencies of  $k = 0.14$  and  $0.02$ , respectively. The correlation presented in Fig. 10a is totally unacceptable. Over much of the cycle, the model predicts a positive rolling moment, while the actual response is the opposite. At the lowest reduced frequency ( $k = 0.02$  in Fig. 10b), there is much better agreement, but the result is still inadequate. Even at this extremely low reduced frequency, there is a lag in the actual response that is not captured by the locally-linear model.

Further insight is provided by Figs. 10c and 10d, which should be compared to Figs. 10a and 10b, respectively. In-phase (circular symbols) and quadrature (squares) components of the actual responses are compared to the corresponding components according to the locally-linear model; i.e., static rolling moment and linearized damping terms, respectively. At  $k = 0.14$ , linearization of the damping term (based on experimental data taken at this frequency) is certainly valid over the range of roll rates encountered in Fig. 10c. However, significant errors are introduced by approximating the in-phase component with the static data.

Similarly, at  $k = 0.02$ , most of the locally linear model's error is again seen to be due to a poor prediction of the in-phase component as shown in Fig. 10d. However, some nonlinear effects are now seen in the quadrature component. The latter problem is compounded if damping derivatives based on small-amplitude, low-frequency ( $k = 0.02$ ) data are used to extrapolate to higher angular rates. Such a case is shown in Fig. 10e where the prediction for  $k = 0.14$  with 3-deg offset and 18-deg amplitude is compared with the corresponding observed rolling moment. Note that the 5-deg amplitude, the smallest used in this test series, is two to three times larger than that used in typical low-amplitude tests. Derivatives based on larger amplitude data (with their associated higher rates) can therefore be expected to yield better predictions when extrapolated to the high rates. Even so, the results are totally unacceptable; the in-phase component errors are completely swamped by those in the damping term. Note that the peaks in the prediction are centered about  $\omega t$  values of 90 and 270 deg where the rate is the highest.

Finally, note the good agreement in Fig. 10f. In this case, the offset roll angle of 28 deg and the 5-deg amplitude ensure that the critical states cannot be reached. The discrepancies here are likely the result of interpolation errors in the static component. Thus, the principal difficulty with the locally linear model noted here is when the motion includes critical states.

Similar effects can be observed in Fig. 11 where trajectories corresponding to three free-to-roll releases are superimposed on a phase-plane portrait constructed with the locally linear model. Obviously the latter is totally incapable of representing the dramatic motion history effects and nonlinearities that prevail following critical-state encounters. Therefore, testing tech-

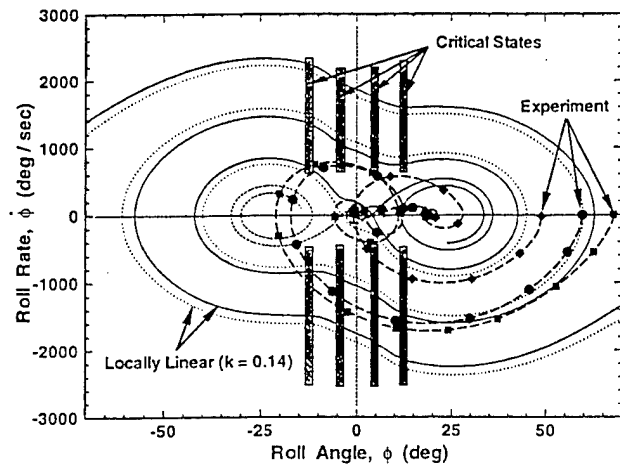


Fig. 11 Actual free-to-roll motions vs locally linear phase portrait.

niques must involve model motions capable of eliciting the transient responses not observable with small-amplitude low-rate experiments. Instantaneous values for aerodynamic loads must be measured to permit observations of these transients. Furthermore, changes in skin-friction and flowfield topology (together with a careful interpretation of static data) may indicate values for flow and motion parameters where critical states are likely to occur.

Clearly, significant errors result if the effects of critical-state encounters are not handled correctly. Therefore, aerodynamic models that can account for the existence of critical states and the transients induced by them are required.

### Acknowledgments

This work was conducted under a Joint Research Program of the U.S. Air Force Office of Scientific Research, Wright Laboratory, the Institute for Aerospace Research, and the Canadian Department of National Defence. The support of these organizations is gratefully acknowledged. The authors are also indebted to Murray Tobak whose counsel (particularly regarding the effects of time-averaged data on the analysis) was indispensable to the interpretation and presentation of these results.

### References

- <sup>1</sup>Tobak, M., Chapman, G. T., and Unal, A., "Modeling Aerodynamic Discontinuities and Onset of Chaos in Flight Dynamical Systems," *Annales des Telecommunications*, Tome 42, Nos. 5 and 6, 1987, pp. 300–314; also NASA TM-89420, Dec. 1986.
- <sup>2</sup>Tobak, M., Chapman, G. T., and Schiff, L. B., "Mathematical Modeling of the Aerodynamic Characteristics in Flight Mechanics," *Proceedings of the Berkeley-Ames Conference on Nonlinear Problems in Control and Fluid Dynamics*, Math Sci Press, Brookline, MA, 1985, pp. 435–450; also NASA TM-85880, Jan. 1984.
- <sup>3</sup>Tobak, M., and Chapman, G. T., "Nonlinear Problems in Flight Dynamics Involving Aerodynamic Bifurcations," *AGARD Symposium on Unsteady Aerodynamics—Fundamentals and Applications to Aircraft Dynamics*, CP-386, AGARD, 1985, pp. 25-1–25-15.
- <sup>4</sup>Tobak, M., and Unal, A., "Bifurcations in Unsteady Aerodynamics," NASA TM-88316, June 1986.
- <sup>5</sup>Truong, K. V., and Tobak, M., "Indicial Response Approach Derived from Navier-Stokes Equations: Part 1—Time-Invariant Equilibrium State," NASA TM-102856, Oct. 1990.
- <sup>6</sup>Hanff, E. S., "Dynamic Nonlinear Airloads—Representation and Measurement," *AGARD Symposium on Unsteady Aerodynamics—Fundamentals and Applications to Aircraft Dynamics*, CP 386, AGARD, 1985, pp. 27-1–27-14.
- <sup>7</sup>Hanff, E. S., "Large Amplitude Oscillations," *Special Course on Aircraft Dynamics at High Angles of Attack: Experiments and Modelling*, AGARD Rept. 776, 1991, pp. 4-1–4-19.
- <sup>8</sup>Jenkins, J. E., and Hanff, E. S., "Non-Linear Airloads Hypersur-

face Representation—A Time Domain Perspective," *Manoeuvring Aerodynamics*, CP 497, AGARD, 1991, pp. 7-1-7-9.

<sup>9</sup>Hanff, E. S., Kapoor, K., and Anstey, C. R., "Large-Amplitude High-Rate Roll Oscillation System for the Measurement of Non-Linear Airloads," AIAA Paper 90-1426, 1990.

<sup>10</sup>Hanff, E. S., and Jenkins, S. B., "Large-Amplitude High-Rate Roll Experiments on a Delta and Double-Delta Wing," AIAA Paper 90-0224, Jan. 1990.

<sup>11</sup>Hanff, E. S., and Ericsson, L. E., "Multiple Roll Attractors of a Delta Wing at High Incidence," *AGARD Symposium on Vortex Flow Aerodynamics*, CP 494, AGARD, 1990, pp. 31-1-31-10.

<sup>12</sup>Hanff, E. S., and Huang, X. Z., "Roll-Induced Cross-Loads on a Delta Wing at High Incidence," AIAA Paper 91-3223, Sept. 1991.

<sup>13</sup>Arena, A. S., Jr., Nelson, R. C., and Schiff, L. B., "An Experimental Study of the Nonlinear Dynamic Phenomenon Known as Wing Rock," *AIAA Atmospheric Flight Mechanics Conference*, AIAA, Washington, DC, 1990, pp. 173-183 (AIAA Paper 90-2812).

<sup>14</sup>Sattinger, D. H., "Bifurcation and Symmetry Breaking in Applied Mathematics," *Bulletin (New Series) of the American Mathematical Society*, Vol. 3, No. 2, 1980, pp. 779-819.

<sup>15</sup>Tobak, M., and Peake, D. J., "Topology of Three-Dimensional Separated Flows," *Annual Review of Fluid Mechanics*, Vol. 14, 1982, pp. 61-85.

<sup>16</sup>Dennis, S. C. R., and Chang, G., "Numerical Solutions for Steady Flow Past a Cylinder at Reynolds Numbers up to 100," *Journal of Fluid Mechanics*, Vol. 42, Pt. 3, 1970, pp. 471-489.

<sup>17</sup>Nishioka, M., and Sato, H., "Mechanism of Determination of the Shedding Frequency of Vortices Behind a Cylinder at Low Reynolds Numbers," *Journal of Fluid Mechanics*, Vol. 89, Pt. 1, 1978, pp. 49-60.

<sup>18</sup>Chen, J.-H., Pritchard, W. G., and Tavener, S. J., "Bifurcation for Flow Past a Cylinder Between Parallel Planes," *Journal of Fluid Mechanics*, Vol. 284, Feb. 1995, pp. 23-41.

<sup>19</sup>Wentz, W. H., and Kohlman, D. L., "Vortex Breakdown on Slender Sharp-Edged Delta Wings," AIAA Paper 69-778, July 1969.

<sup>20</sup>Payne, F. M., and Nelson, R. C., "An Experimental Investigation of Vortex Breakdown on a Delta Wing," *Vortex Flow Aerodynamics—Vol. I*, 1985, pp. 135-161 (NASA CP 2416).

<sup>21</sup>Conte, S. D., *Elementary Numerical Analysis*, McGraw-Hill, New York, 1965, p. 140.

<sup>22</sup>Chaderjian, N. M., and Schiff, L. B., "Navier-Stokes Prediction of a Delta Wing in Roll with Vortex Breakdown," AIAA Paper 93-3495, Aug. 1993.

<sup>23</sup>Jenkins, J. E., "Simplification of Nonlinear Indicial Response Models: Assessment for the Two-Dimensional Airfoil Case," *Journal of Aircraft*, Vol. 25, No. 2, 1991, pp. 131-138.



# **Critical States and Flow Structure on a 65-Deg Delta Wing**

Charles E. Jobe, Alexander H. Hsia,  
Jerry E. Jenkins, Gregory A. Addington

Reprinted from

## **Journal of Aircraft**

Volume 33, Number 2, Pages 347-352



*A publication of the*  
American Institute of Aeronautics and Astronautics, Inc.  
370 L'Enfant Promenade, SW  
Washington, DC 20024-2518

# Critical States and Flow Structure on a 65-Deg Delta Wing

Charles E. Jobe,\* Alexander H. Hsia,† Jerry E. Jenkins,‡ and Gregory A. Addington†  
*U.S. Air Force Wright Laboratory, Wright–Patterson Air Force Base, Ohio 45433*

Swept and delta wings maneuvering at moderate and high angles of attack produce highly nonlinear and often discontinuous aerodynamic forces and moments that are difficult to model. The nonlinear indicial response (NIR) methodology and the concept of critical states accompanied by changes in the flow structure and topology could provide a rational framework for the analyses and modeling of these flows. The analysis of surface oil-flow photographs and laser light sheet high-speed video images of smoke flow has been performed. The correlation of the structural and topological changes in the flow with force and moment data follows. Critical states are often accompanied by changes in the flow topology and not all topological changes produce measurable changes in the forces and moments, however, a useful relationship may exist.

## Introduction

AIRCRAFT with delta wings have flown since the early 1950s (Vulcan, F-102, Mirage III, MiG-21, B-58, XB-70, Eurofighter 2000 prototype, etc.), when the jet engine with its higher speed capability replaced propellers and piston engines. The drag reduction for thinner wings with increased sweep was well known and leads to the delta planform with greater structural rigidity, gradual stall characteristics, and high lift at maneuvering and landing attitudes and speeds. The triangular delta wing was, however, not without disadvantages that required stability augmentation and double-delta, straked delta, and other closely related planforms to correct. While primarily used for high-performance fighter aircraft, these planforms also have found application to the Concorde supersonic transport and proposed High Speed Civil Transport designs.

The nonlinear lift increase at low speeds is generated by leeward vortices produced by the rolling up of the shear layers emanating from the leading edges. These vortices, while producing the desirable lift increase, considerably complicate the flowfield and its prediction. The flowfield is symmetric and predictable at moderate angles of attack for symmetric flight conditions. Unpredictable changes in the static forces and moments occur during high angle-of-attack maneuvers and during even moderate asymmetric flight conditions when vortex burst may occur over the planform. Vortex burst or vortex breakdown is characterized by the sudden expansion of the highly organized core into bubbles or spirals along the core axis. Shortly downstream, the bubbles or spirals diffuse into a disorganized, swirling turbulent flow. Vortex burst normally occurs first in the wake, proceeding upstream toward the wing's apex as angle of attack, sideslip (windward wing only), or aspect ratio increase. Associated with the forward motion of the burst point are loss of lift, pitchup and nonlinear, often discontinuous, pitching and rolling moment characteristics.<sup>1</sup>

Beginning in 1987, the Canadian Institute for Aerospace Research (IAR) and the Flight Dynamics Directorate of Wright

Laboratory have been pursuing a collaborative research program on unsteady and vortex-dominated flows. The need being addressed is the lack of appropriate mathematical modeling techniques to represent the interaction between the vehicle motion and the forces and moments created by these flows. The requirements for aerodynamic modeling arise in at least three areas: 1) for aerodynamic understanding and design, 2) for control system design, and 3) for flight simulation.

A theoretical method for studying the nonlinear aspects of the flight dynamics problem has been under development by Tobak and his colleagues<sup>2–4</sup> at NASA Ames Research Center since the early 1960s. Their approach introduced two important new concepts: 1) a nonlinear indicial response (NIR) and 2) a generalized superposition integral.

The NIR approach, which has been derived from the Navier–Stokes equations for a time-invariant equilibrium state,<sup>4</sup> allows that critical states may be signaled by changes in the static flow topology, often manifest in the position and behavior of vortices within the flow. The movement of the leading-edge vortex burst point onto the planform and the introduction of secondary and tertiary vortices are examples of topological changes, as are changes in the number of singular points in the skin-friction lines. In principle, the NIR is not restricted to a time-invariant equilibrium state; however, the details of the proof have not been completed and published.

As with linear indicial response methods, the arbitrary motion is represented as a summation of responses to a series of step motions. The NIR, as opposed to its linear counterpart, accounts for changes induced by the motion history leading up to step onset. Under a wide variety of circumstances, the summation of indicial responses approaches the generalized superposition integral in the limit.

The formulation also allows for critical states where the aerodynamic response loses analytical dependence on the motion variable, such as when aerodynamic bifurcations occur.<sup>3</sup> A critical state is accommodated by splitting the generalized superposition integral at the critical state and including a transient response term. Its location is defined by the values of a set of variables that characterize the instantaneous motion.

A critical state is a flight condition where large and persistent transients may be introduced into the aerodynamic loads, invalidating the linear and locally linearized aerodynamic models traditionally used for flight mechanics predictions. For example, the result of roll-angle and roll-rate-induced velocities at the leading edge of a delta wing is an unsymmetrical vortex lift that produces a highly nonlinear (perhaps discontinuous) change in the rolling moment.

A critical state is often associated with a change in the number of critical points in the static time-averaged surface flow

Presented as Paper 94-3479 at the AIAA Atmospheric Flight Mechanics Conference, Scottsdale, AZ, Aug. 1–3, 1994; received Sept. 7, 1994; revision received Oct. 11, 1995; accepted for publication Oct. 12, 1995. This paper is declared a work of the U.S. Government and is not subject to copyright protection in the United States.

\*Aerospace Engineer, Building 146, Room 305, 2210 Eighth Street, Suite 11. Associate Fellow AIAA.

†Aerospace Engineer, Building 146, Room 305, 2210 Eighth Street, Suite 11. Member AIAA.

‡Aerospace Engineer, Building 146, Room 305, 2210 Eighth Street, Suite 11. Senior Member AIAA.

topology as shown later. Physically realizable flows produce streamlines and skin friction line patterns in oil flows that must satisfy topological rules based entirely on kinematics and the differential equations of streamlines. A stagnation point is a critical point, also called singular point and equilibrium point,<sup>3</sup> in the flow as is a point where the skin friction vector is zero. Critical points are classified as nodes or saddles depending on their appearance and mathematical properties. Nodes are further subdivided into nodal points of attachment or separation, foci, and centers. All skin-friction lines or streamlines intersect at the node and are directed away from a node of attachment and toward a node of separation. The focus or spiral node has all of the lines spiraling inward or outward around the critical point. If the trajectories form closed paths around the focus, it is a center. The saddle has two oppositely directed lines that intersect at the critical point. All other lines curve away in each quadrant to avoid this critical point.

The correspondence between critical states and static flow topology changes is controversial, especially when time-averaged data (e.g., surface oil flow studies) are involved (see Ref. 6). The analytic dependence of the aerodynamic response may be lost at a change in flow topology, i.e., when a change in the number of critical points is observed.<sup>3</sup> A current consensus is that critical states are often signaled by changes in the flow topology; however, some changes in the flow topology do not produce measurable force and moment transients. A complete discussion of the controversy and how vortex formation in the wake of a circular cylinder at low Reynolds number provides a counterexample has been given by Jenkins et al.<sup>6</sup>

### Experimental Program

The flow about delta wings is highly sensitive to very small differences in model geometry, motion variables, and flow conditions making analysis and correlation of the vast amounts of available data difficult. The experimental program eliminated many of these variables by testing the same model in two wind tunnels at similar flow conditions with overlapping ranges of the motion variables and different support systems. The program is continuing with previous measurements identifying regions of particular interest for succeeding tests.

The common model is a 65-deg swept triangular wing with sharp leading edges (10-deg symmetric nonconical bevel on all three edges) and centerbody (Fig. 1). It was especially designed and constructed to be lightweight, with low inertia to attain the desired motions, yet strong enough to withstand the loads encountered at the high pitch and roll rates required to match full-scale aircraft reduced frequencies (see Hanff and Jenkins<sup>7</sup> for details).

Static and dynamic tests of this model have been a particularly rich source of nonlinearities and other unusual dynamic behavior. The extensive experimental database allows concurrent study of vortex dynamics and the resulting unsteady aero-

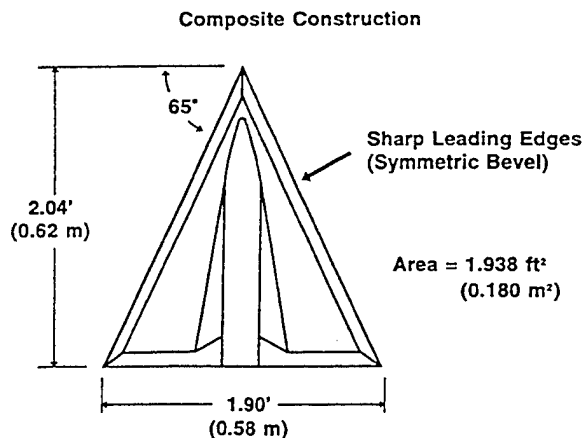


Fig. 1 Model geometry.

dynamic forces and moments. The correct identification of changes in the flow physics and topology is crucial to further understanding the NIR methodology and its application to this series of wind-tunnel test data.

The IAR experimental program, conducted in the National Aeronautical Establishment 6 × 9 ft low-speed wind tunnel, has been described by Hanff and Jenkins<sup>7</sup> and Huang et al.<sup>1</sup> The Wright Laboratory 7 × 10 ft Subsonic Aerodynamic Research Laboratory and the experimental data has been described by Jenkins and various coauthors.<sup>6,8,9</sup> IAR personnel conducted all dynamic testing using their roll rig. The most extensive data set was taken at Mach number 0.3, Reynolds number  $3.6 \times 10^6$  based on the centerline chord of 2.04, (0.622 m) sting angle of 30 deg, with various static and mean roll angles  $\phi$ , and roll rates. The static roll response is highly nonlinear,<sup>10</sup> with three distinct static roll attractors. Further, forced-oscillation and free-to-roll data exhibited strong nonlinearities that cannot be modeled using locally linear models.<sup>6</sup>

### Critical States and Topology

Analysis of the static and dynamic force and moment data<sup>6</sup> indicated critical states near  $\phi = 5$  and 11.3 deg, based on slope changes and discontinuities in the static time-averaged pitching and rolling moments and transients in the dynamic data. Additional evidence confirming the existence of these critical states has been provided by a wealth of subsequent experimental data<sup>8,9</sup> and analyses.<sup>1,11</sup> The following analysis correlates the changes in static forces and moments with the topology changes described by Huang et al.<sup>1</sup> The changes in the forces are small because the vortex flow patterns contribute

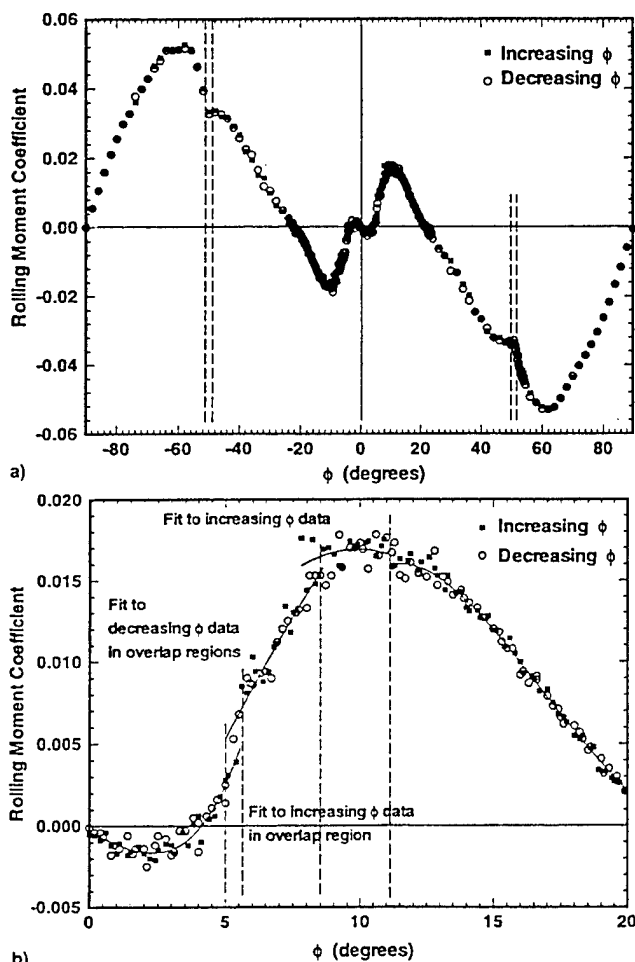


Fig. 2 Rolling moment coefficient: a) full range,  $-90 \leq \phi \leq 90$  deg and b) expanded scale,  $0 \leq \phi \leq 20$  deg.

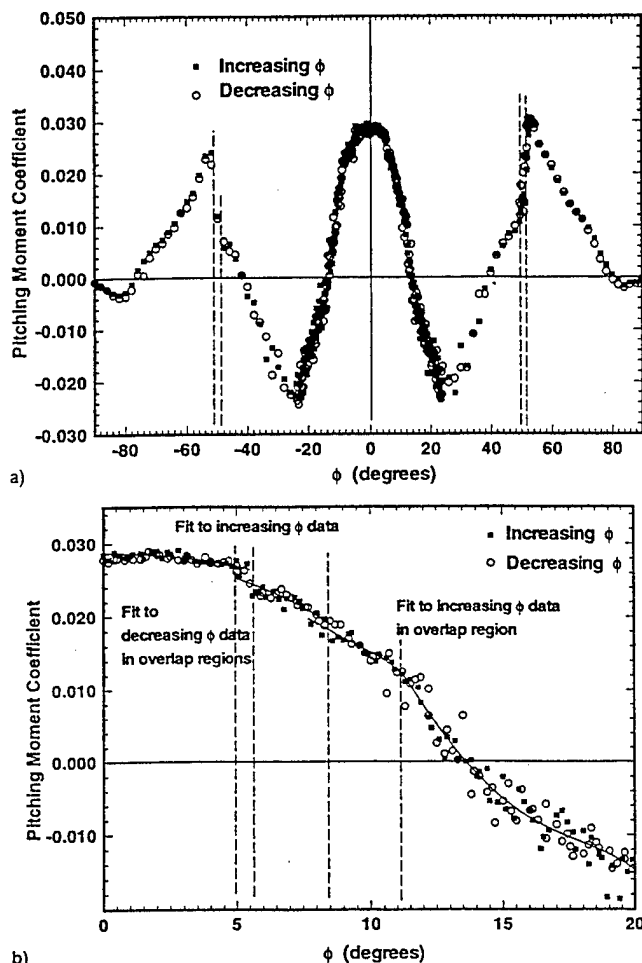


Fig. 3 Pitching moment coefficient: a) full range,  $-90 \leq \phi \leq 90$  deg and b) expanded scale,  $0 \leq \phi \leq 20$  deg.

less than 10% of the total lift at 30-deg angle of attack, zero roll angle for this aspect ratio 1.86 wing. Thus, changes in the vortex flows rarely obviate trends established by the attached flow, as will be discussed subsequently. Critical states, however, lead to large deviations from the static characteristics, especially in the moments.

Experimental data for the entire roll angle range ( $-90$  to  $+90$  deg) and to an expanded scale emphasizing the 5 and 11.3 deg (to be discussed later) critical states are shown in Figs. 2–5. The force and moment coefficients are based on the dynamic pressure and the wing area of  $1.94 \text{ ft}^2$  ( $0.180 \text{ m}^2$ ). Reference lengths are the mean aerodynamic chord of  $1.36 \text{ ft}$  ( $0.415 \text{ m}$ ) for the pitching moment coefficient and the wing span of  $1.90 \text{ ft}$  ( $0.58 \text{ m}$ ) for the body-axis rolling moment coefficient. Dashed vertical lines indicate the critical state locations. The data has been sorted and plotted according to the direction the wing was rolling toward (increasing or decreasing  $\phi$ ) when the particular roll angle was attained. This is contrary to previous analyses<sup>6,8,9</sup> based on rather sparse static data and permits a more detailed examination for discontinuities, slope changes, and hysteresis that indicate the crossing of critical states.

The full-range data plots, Figs. 2a, 3a, 4a, and 5a, show proper symmetry. Time-averaged force and moment behavior at the previously determined critical states at large roll angles<sup>9</sup> ( $-51.3$ ,  $-49.5$ ,  $50.1$ , and  $51.4$  deg), are also shown on these figures as dashed vertical lines. The data density on this scale precludes definite identification of the critical states at either  $\phi = 5$  or  $11.3$  deg. All data were fit using Legendre polynomials and stepwise regression analysis as reported previously<sup>6,9</sup> on the earlier sparse data sets.

### Five-Deg Critical State

The discontinuity near 5-deg roll angle in Figs. 2b, 3b, and 4b is clearly a critical state. It is associated with the leeward (port for positive roll angles) wing vortex burst rapidly crossing the trailing edge during extremely small roll angle increases, as shown by previous authors.<sup>6,8,9</sup> This is in agreement with the topological maps of Huang et al.<sup>1</sup> that show the primary vortex burst is over the leeward wing at  $\phi = 4$  deg and is absent at  $\phi = 7$  deg. It is only the secondary and tertiary vortices that lift off [shown as whorls or foci (spiral nodes) in the skin-friction topology] at  $\phi = 7$  deg.

Figure 6a shows the vortex burst of the leeward leading-edge vortex is 10–15% chord aft of the trailing edge at  $\phi = -5.4$  deg, while Fig. 6b shows the vortex burst has moved upstream onto the planform at  $\phi = -5.0$  deg. Note the rapid forward progression to 10–15% chord ahead of the trailing edge in only 0.4-deg roll angle change. This is the discrete change that defines the critical state.

The increase in positive rolling moment as  $\phi$  increases (Fig. 2b) is consistent with the formation of the coherent vortex over the entire leeward wing. As the vortex burst point moves aft, off the wing, the extended, concentrated vortex core decreases the pressures on the leeward wing upper surface and contributes an additional destabilizing moment. The additional force near the trailing edge also contributes a nose-down, stabilizing increment to the pitching moment (Fig. 3b). The axial force (Fig. 4b) shows an increase, consistent with the known drag increase attendant with lifting leading-edge vortices. The normal force is decreasing because of the sideslip increase.

The regression analysis performed on data in this region was split into two separate domains, increasing and decreasing  $\phi$ ,

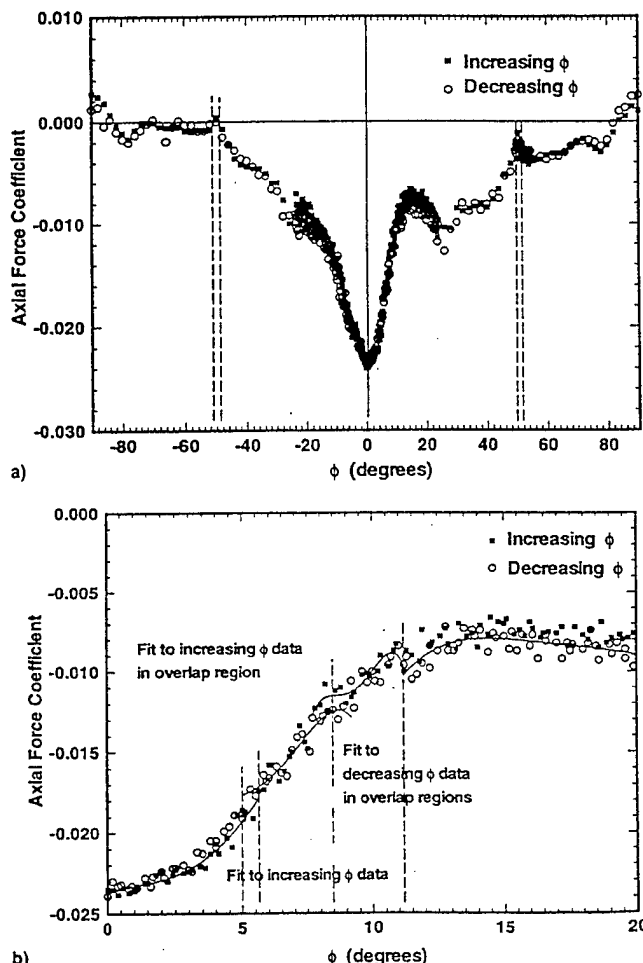


Fig. 4 Axial force coefficient: a) full range,  $-90 \leq \phi \leq 90$  deg and b) expanded scale,  $0 \leq \phi \leq 20$  deg.

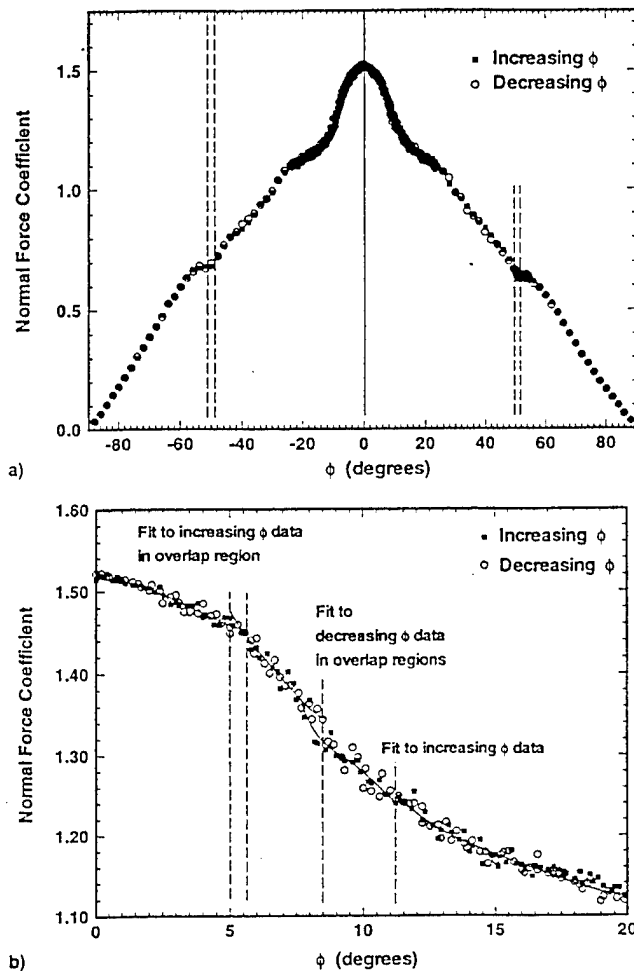


Fig. 5 Normal force coefficient: a) full range,  $-90 \leq \phi \leq 90$  deg and b) expanded scale,  $0 \leq \phi \leq 20$  deg.

between  $\phi = 5.0$ – $5.7$  deg. Only the increasing  $\phi$  data were used in this region for the regression fitting the lower branch in this region, while only decreasing  $\phi$  data were used for the upper branch. This partitioning of data is consistent with the definition of a static hysteresis, and shows that a narrow hysteresis loop apparently exists in this region. Further, two critical states must exist here, one at the terminus of each branch. Past and present analyses of experimental data suggest such a possibility. The analysis of Addington and Jenkins<sup>8</sup> show that the leeward leading-edge vortex burst point crosses the trailing edge from being over the planform at approximately  $\phi = 5$  deg. Huang et al.<sup>1</sup> analysis confirms this finding, as well as suggests that an additional topological change occurs in this region.

Several correlations have been devised to predict the movement of vortex burst points with leading-edge sweep angle, angle of attack, and roll angle. The predicted roll angle for vortex breakdown at the trailing edge is 7 deg based on a linear regression fit<sup>8</sup> of the static data of Hanff and Huang<sup>12</sup>; 8.8 deg based on Ericsson and Hanff's<sup>10</sup> method (using Wentz and Kohlman's<sup>13</sup> vortex breakdown correlations, vortex breakdown occurs at the trailing edge at 19-deg angle of attack for  $\phi = 0$  deg); and 13.7 deg from the revised Huang and Hanff<sup>14</sup> method. Their correlations are a better approximation to experimental data<sup>11,14</sup> for the 60- and 70-deg swept wings than for the 65-deg swept wing, again indicating unusual behavior<sup>9,10</sup> at this combination of roll and sweep angles. None of these vortex breakdown prediction methods account for the rapid jump in vortex position because they assume smooth functions to correlate the experimental data.

### 11.3-Deg Critical State

The tentatively associated change in flow topology near  $\phi = 12$  deg, the vortex breakdown point reaching the windward (starboard) wing's apex,<sup>6</sup> was shown to be erroneous<sup>8</sup> by analysis of the subsequent static and forced-oscillation dynamic wind-tunnel data called for by Jenkins et al.<sup>6</sup> The assumption of vortex breakdown reaching the apex of the windward wing near  $\phi = 12$  deg was not unfounded, particularly in light of the lack of detailed flow visualization data available at the time. The linear regression data fit of Addington and Jenkins<sup>8</sup>

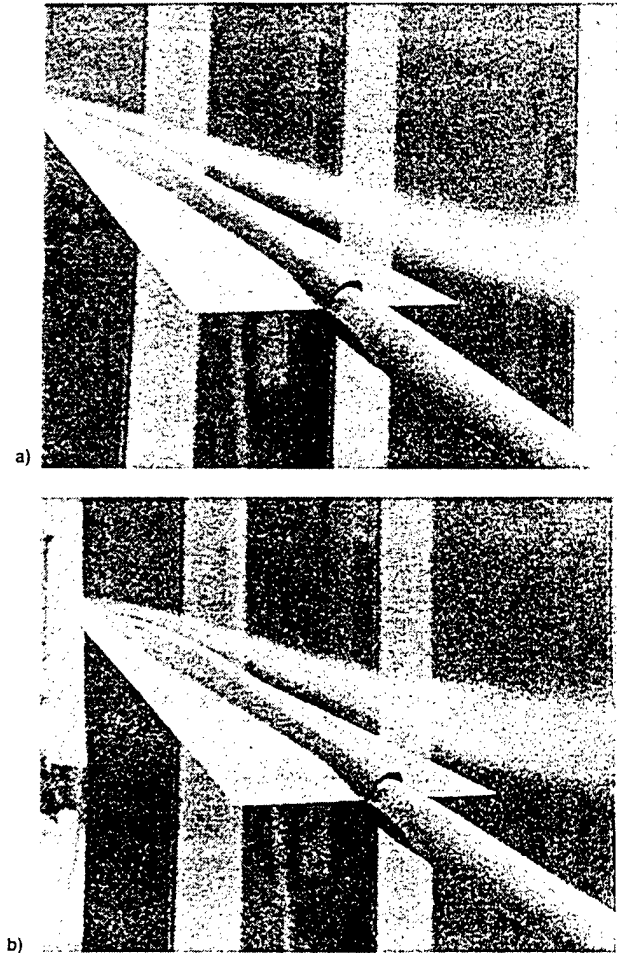


Fig. 6 Leeward leading-edge vortex burst: a) in the wake,  $\phi = -5.4$  deg and b) over the planform,  $\phi = -5.0$  deg.

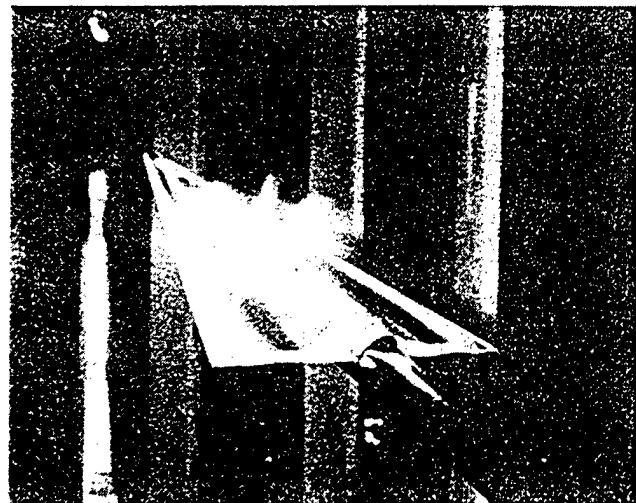


Fig. 7 Laser light sheet flow visualization.

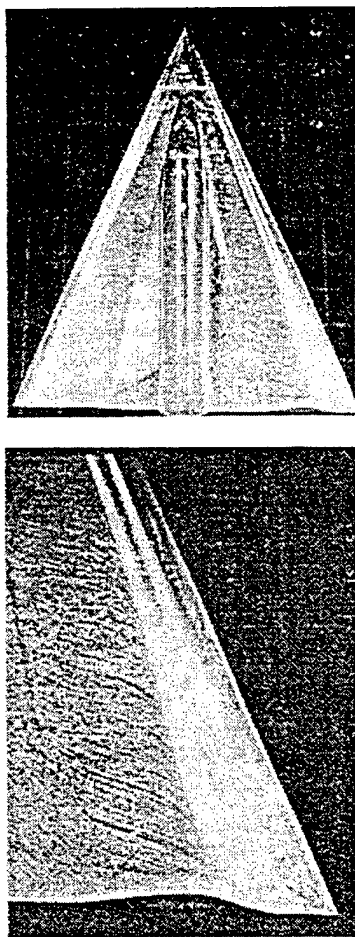


Fig. 8 Surface oil flow,  $\phi = -7$  deg.

predicted  $\phi = 13$  deg, whereas the methods of Ericsson and Hanff<sup>10</sup> and Huang and Hanff<sup>14</sup> predicted 12.6 and 12.15 deg, respectively. Vortex breakdown would occur aft of the trailing edge on the leeward wing and could not cause the observed force and moment transients. The preceding analysis methods generally agree with the original association of vortex breakdown at the apex. However, analysis of the previous dynamic and new high-resolution static data taken in the same wind tunnel using the same model (the sting and instrumentation were different, which permitted additional verification of the data through correlations at selected tie-in conditions) clearly shows that the critical state is not associated with vortex breakdown advancing to the apex at  $\phi = 11.3$  deg.

The experimental setup with the laser light sheet is shown in side view in Fig. 7. The laser light sheet has progressed to aft of the midchord and the leading-edge vortex over the entire leeward wing is evident at  $\phi = 14.5$  deg. The light sheet shows the shear layer from the windward wing has moved across the centerbody at this chordwise station, in agreement with the observations of Hsia et al.<sup>9</sup> Video recordings of the fore and aft sweeps of the laser light sheets show that the flow becomes unsteady as the critical roll angle is approached and returns to steady motion as this roll angle is exceeded. While a still image suitable for publication could not be captured by our equipment, the videotapes clearly show a vortex near the apex of both the windward and leeward wings at  $\phi = 15$  deg. Both vortices are evident at all roll angles less than 15 deg, while the vortex over the windward wing is not apparent at  $\phi = 18$  deg. The vortex persists over the entire leeward wing at this roll angle.

Surface oil flows near the trailing edge at nearly the same test conditions (30-deg roll angle and 0.3 Mach number) are shown in Figs. 8 and 9 at roll angles of  $-7$  and  $-14$  deg. A

description of the model and experimental setup is contained in Hanff et al.<sup>15</sup> The change in flow topology is evident. Two vortex whorl patterns are evident over the leeward wing at a roll angle of  $-7$  deg, while one is evident at  $\phi = -14$  deg. These patterns correspond to the liftoff of the tertiary vortex (Fig. 8) and to liftoff of both the secondary and tertiary vortices (Fig. 9) on the planform. The flow pattern and topology sketches from Huang et al.<sup>1</sup> show this topology change occurs between roll angles of  $-7$  and  $-14$  deg, but the precise roll angle and triggering mechanism are unknown. According to Huang et al.,<sup>1</sup> the change in flow pattern corresponds to a critical state crossing; however, additional images and analysis are needed to fill these experimental data gaps.

From Huang et al.,<sup>1</sup> between 10- and 14-deg roll angle, the flow on the windward wing changes from an organized vortex flow with the tertiary vortex lifting off the surface to a topology representative of primary vortex breakdown advancing toward, but not attaining, the wing apex. This creates a disorganized spiraling flow aft of the breakdown, exhibiting reverse flow partly swept across from the leeward wing, and a loss of vortex lift on the windward wing. The leeward wing undergoes a topological change indicative of reattachment of the secondary vortex near the wingtip as the roll angle increases. The organized, spiraling flow beneath this secondary vortex increases the normal force on the area near the wingtip and produces force and moment changes similar to the 5-deg case, albeit smaller. The force and moment changes are also influenced by the vortex lift loss over the windward wing.

Returning to Figs. 2-5, at  $\phi = 11.3$  deg, the negative slope of the rolling moment curve becomes less negative because of the additional destabilizing moments contributed by both the windward and leeward wings (Fig. 2b). The nose-up pitching moment slope is increased by the additional force near the leeward wing trailing edge (Fig. 3b), causing the discontinuity in slope. The scatter in the axial force data (Fig. 4b) and the magnitude of the changes precludes definitive conclusions;

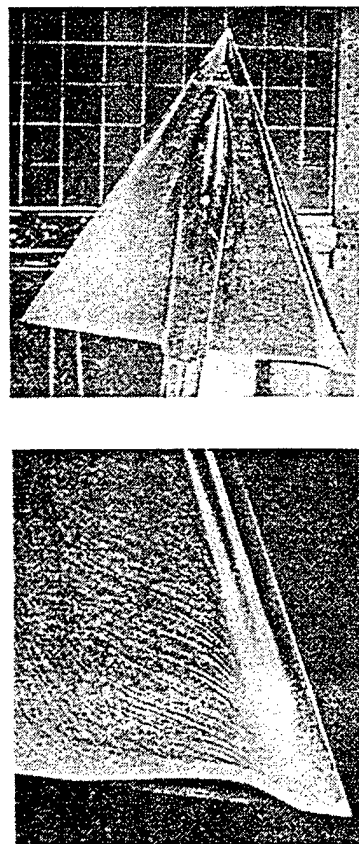


Fig. 9 Surface oil flow,  $\phi = -14$  deg.

however, a discontinuity in slope is evident. The overall normal force is decreasing (Fig. 5b) because of increasing roll angle and the additional force caused by the leeward vortex is somewhat counteracted by the reduced vortex lift over the windward wing. The rate of lift decrease is slowed and causes the slope discontinuity.

### 8.5-Deg Critical State

A suspected critical state is marked at  $\phi = 8.5$  deg in Figs. 2b–5b. The topological change shown by Huang et al.<sup>1</sup> reinforces the evidence obtained by separately fitting the roll angle increasing or decreasing data.

The polynomial regression fit of the experimental force and moment data for increasing and decreasing roll angle is shown as solid lines in Figs. 2b, 3b, 4b, and 5b. Two distinct branches near  $\phi = 8.5$  deg are evident in each data set. The use of an overlapping domain (from  $\phi = 7.7$  to 9.2 deg) to fit the data increases the correlation coefficient compared to strictly monotonic data fits.

Huang et al.<sup>1</sup> report that a topology change occurs between  $\phi = 7$  and 10 deg. This change is associated with global flow separation occurring over the windward (starboard) wing as roll angle increases. The force and moment discontinuities occurring; increase in rolling moment, decrease in nose-up pitching moment, and decrease in axial and normal forces are consistent with the loss of suction because of the disappearance of the leading-edge vortex over the windward wing.

### Discussion

The previous correlations agree with the topological analysis of Huang et al.<sup>1</sup> that is based on oil flow pictures and video images taken at discrete roll angles every 3 or 4 deg. Additional anomalies in the force and moment data create the possibility of additional topological changes. The separate analysis of roll angle increasing or decreasing data indicates the possibility of hysteresis at the 5-deg critical state (Fig. 2b) that would require two critical states, one near 5.0 deg and one near 5.7 deg. Hysteresis is also evident in the pitching moment data (Fig. 3b) and an additional discontinuity appears near  $\phi = 8$  deg, where flow visualization data were not recorded.

A presently unexplained anomaly appears in these data. The branches in the force and moment data at  $\phi = 8.5$  deg cannot form a hysteresis loop. The increases or decreases in the coefficients are either in the opposite direction or at opposite ends of where they would occur in a hysteresis loop. Furthermore, only one topology change is observed between  $\phi = 7$ –10 deg in the mean surface oil flows. The lack of data in this roll angle range does not permit resolution of this anomaly, however, several possible explanations are 1) additional topological changes occur in the surface flow, 2) topological changes occur in the streamlines of the off-body flow, or 3) the flow becomes unsteady through a Hopf bifurcation.

Current analyses are based on surface oil flows related to static force and moment data. The time-averaging property of this flow visualization method precludes inference of the unsteady effects necessary to further elucidate the relationship between critical states in the aerodynamic response and changes in the number of critical points in the flow.

Certainly a wealth of interesting possibilities occurs that cannot be confirmed based on presently available data, but point to the need for specific high resolution data to resolve these questions. The high resolution available from Navier–

Stokes numerical simulations<sup>16</sup> of these experiments cannot be equaled for directing attention to, and clarifying, otherwise confusing or unnoticed flow features. It is currently too expensive to perform simulations at all of the points needed. The need for additional testing to fill these gaps is evident.

Correlation of critical states and topology changes is exceedingly difficult and time consuming because of the precision and resolution required in both the static and dynamic data. The static force and moment data across suspected discontinuities and hysteresis loops should be used, along with flow visualization, to identify conditions for critical states. Subsequent dynamic experiments should focus on these conditions to identify critical-state transient characteristics.

### Acknowledgments

This work was conducted under a Joint Research Program of the U.S. Air Force Office of Scientific Research, their support is gratefully acknowledged as are the efforts of the Canadian Institute of Aerospace Research personnel.

### References

- Huang, X. Z., Hanff, E. S., Jenkins, J. E., and Addington, G., "Leading-Edge Vortex Behavior on a 65° Delta Wing Oscillating in Roll," AIAA Paper 94-3507, Aug. 1994.
- Tobak, M., and Pearson, W. E., "A Study of Nonlinear Longitudinal Dynamic Stability," NASA TR R-209, Sept. 1964.
- Tobak, M., Chapman, G. T., and Unal, A., "Modeling Aerodynamic Discontinuities and Onset of Chaos in Flight Dynamical Systems," *Annales Des Telecommunications*, Vol. 42, Nos. 5–6, 1987, pp. 300–314; also NASA TM-89420, Dec. 1986.
- Truong, K. V., and Tobak, M., "Indicial Response Approach Derived from Navier-Stokes Equations Part 1, Time Invariant Equilibrium State," NASA TM 102856, Oct. 1990.
- Kaplan, W., *Ordinary Differential Equations*, 1st ed., Addison-Wesley, Reading, MA, 1958, pp. 414–470.
- Jenkins, J. E., Myatt, J. H., and Hanff, E. S., "Body-Axis Rolling Motion Critical States of a 65-Degree Delta Wing," AIAA Paper 93-0621, Jan. 1993.
- Hanff, E. S., and Jenkins, S. B., "Large-Amplitude High-Rate Rolling Experiments on a Delta and Double Delta Wing," AIAA Paper 90-0224, Jan. 1990.
- Addington, G., and Jenkins, J., "Flow Visualization of a Rolling Delta Wing and Its Pertinence to the Nonlinear Indicial Response Model," AIAA Paper 93-3469, Aug. 1993.
- Hsia, A. H., Myatt, J. H., and Jenkins, J. E., "Nonlinear and Unsteady Aerodynamic Responses of a Rolling 65-Delta Wing," AIAA Paper 93-3682, Aug. 1993.
- Ericsson, L., and Hanff, E. S., "Further Analysis of High-Rate Rolling Experiments of a 65 Deg Delta Wing," AIAA Paper 93-0620, Jan. 1993.
- Huang, X. Z., and Hanff, E. S., "Prediction of Leading-Edge Vortex Breakdown on a Delta Wing Oscillating in Roll," AIAA Paper 92-2677, June 1992.
- Hanff, E. S., and Huang, X. Z., "Roll-Induced Cross-Loads on a Delta Wing at High Incidence," AIAA Paper 91-3223, Sept. 1991.
- Wentz, W. H., and Kohlman, D. L., "Vortex Breakdown on Slender Sharp-Edged Wings," *Journal of Aircraft*, Vol. 8, No. 3, 1971, pp. 156–161.
- Huang, X. Z., and Hanff, E. S., "Prediction of Normal Force on a Delta Wing Rolling at High Incidence," AIAA Paper 93-3686, Aug. 1993.
- Hanff, E. S., Kapoor, K., Anstey, C. R., and Prini, A., "Large-Amplitude High-Rate Roll Oscillation System for the Measurement of Non-Linear Airloads," AIAA Paper 90-1426, June 1990.
- Chaderjian, N., and Schiff, L., "Navier-Stokes Prediction of Large-Amplitude Forced and Free-to-Roll Delta Wing Oscillations," AIAA Paper 94-1884, June 1994.

# **Temporal Evolution of Three-Dimensional Vortex Breakdown from Steady, Axisymmetric Solutions**

Jeffrey C. Tromp and Phillip S. Beran

Reprinted from

## **AIAA Journal**

Volume 34, Number 3, Page 632-634



*A publication of the*  
American Institute of Aeronautics and Astronautics, Inc.  
370 L'Enfant Promenade, SW  
Washington, DC 20024-2518



# Temporal Evolution of Three-Dimensional Vortex Breakdown from Steady, Axisymmetric Solutions

Jeffrey C. Tromp\* and Philip S. Beran†

U.S. Air Force Institute of Technology,  
Wright-Patterson Air Force Base, Ohio 45433-7521

## Introduction

THE emergence and consequences of asymmetries in swirling flows that are initially steady and axisymmetric are examined. The strength of an isolated vortex in a tube is increased in a parametric fashion through a critical value, where stability to three-dimensional disturbances is lost. The flow behavior undergoes a bifurcation at the critical value from steady and axisymmetric flow to unsteady and three-dimensional flow. Other computations of bifurcation phenomena in swirling flows have been presented by Leibovich and Kribus,<sup>1</sup> Beran and Culick,<sup>2</sup> and Lopez.<sup>3</sup> These works are limited to bifurcations that only involve axisymmetric flows.

Axisymmetric base flows serve as initial conditions to a three-dimensional time-integration algorithm. The minimum axial velocity component  $Q(t)$  is computed and compared with the initial value. Of particular interest is the characterization of the stability loss and the relationship between the appearance of asymmetries and the associated changes in  $Q$ .

The computational approach is as follows. First, a pseudo-arclength continuation (PAC) algorithm<sup>2</sup> provides the steady, axisymmetric initial condition for a specified vortex strength  $\mathcal{V}$ . The Mach number  $M$  and Reynolds number  $Re$  (based on vortex core radius) are held fixed at 0.3 and  $2.5 \times 10^2$ , respectively. No nonunique axisymmetric solutions are found at  $Re = 2.5 \times 10^2$ , consistent with Ref. 2. The two-dimensional solution is then interpolated onto the three-dimensional mesh using a fourth-order-accurate cubic spline scheme.<sup>4</sup> Then time integration is carried out by the time-accurate Navier-Stokes (TANS) model. The TANS model is a special-purpose, time-integration algorithm developed specifically for this work and is described in Ref. 5. The TANS model employs fourth-order compact, or Padé, operators<sup>6</sup> to discretize spatial derivatives, thus allowing for fewer grid nodes while maintaining sufficient accuracy. A multiblock grid is used to allow for a nearly rectilinear arrangement of nodes near the tube centerline, while near orthogonality is maintained at the tube wall. The PAC algorithm is implemented with the same boundary conditions and tube geometry as the TANS model, using a simple algebraic grid.

The physical domain consists of a two-stage cylindrical tube of circular cross section and varying radius.<sup>2</sup> The first stage contains a constriction that controls the upstream movement of the breakdown region. The tube radius (nondimensionalized by vortex core radius) at the inlet station is fixed at  $R_0 = 2$ . The number of nodes in the computational coordinate directions are  $(n_x, n_y, n_z)$ , where  $n_x$  defines streamwise spacing and  $n_y$  and  $n_z$  are equal and define cross-plane spacing in the  $y$  and  $z$  directions, respectively. Three grids are employed in this work. Grid G1 consists of  $98 \times 41^2$  nodes, grid G2 contains  $122 \times 61^2$  nodes, and grid G3 uses  $146 \times 41^2$

nodes. The nondimensional tube length  $L$  for grids G1 and G2 is 20, whereas the tube length for grid G3 is 30. Grid G2 uses axial clustering in the breakdown region to achieve a minimum axial spacing of about 0.1 at  $x = 5$ . The time step  $\Delta t$  for runs using grids G1 and G3 is 0.04, whereas runs on the finer grid G2 have a time step of 0.025.

Axisymmetric, columnar conditions are specified at the inflow boundary plane. The inlet axial velocity is chosen to be uniform. The swirl velocity component  $\hat{v}$  is modeled from a Burger vortex and is appropriate for modeling the profiles obtained from a swirl-vane apparatus<sup>7</sup>:

$$\hat{v}(0, r, \theta) = \mathcal{V}r^{-1}(1 - e^{-r^2}) \quad (1)$$

where  $r$  and  $\theta$  denote the radial and azimuthal coordinate directions and  $\mathcal{V}$  is the vortex strength. A nonuniform inflow density profile based on columnar flow is prescribed as a Dirichlet condition.<sup>5</sup> Slip is allowed along the tube wall surface, yielding an impermeability boundary condition that relates the axial and radial velocities. Outflow conditions reflect an assumed columnar flow state.

## Results

Between  $\mathcal{V} = 1.0$  and 1.5, the initially steady, two-dimensional flow does not evolve in time to an asymmetric flow state. However, as  $\mathcal{V}$  is increased slightly to 1.53, the flow becomes three dimensional and time periodic. As  $\mathcal{V}$  is further increased, the magnitude of the asymmetry also increases. This change in stability is attributed to the crossing of a supercritical Hopf bifurcation point somewhere between  $\mathcal{V} = 1.5$  and 1.53.

The deviations from the two-dimensional initial conditions are illustrated in Fig. 1, where  $Q$  (solid lines of Figs. 1a–1d) is plotted vs time for  $\mathcal{V} = 1.5, 1.53, 1.55$ , and 1.65. In Fig. 1a ( $\mathcal{V} = 1.5$ ), it is evident that no appreciable deviation from the initial condition is present. This is confirmed by monitoring the maximum solution correction at each iteration. At  $\mathcal{V} = 1.53$  (Fig. 1b), the solution departs from the initial condition, as evident by the increase in  $Q$  as time increases. The term  $Q(t)$  eventually becomes time periodic, but this behavior is not discernible from the scales of the figure. Periodicity is confirmed using phase plots of the three velocity components at a fixed centerline node near  $x = 7$ . At  $\mathcal{V} = 1.55$  and 1.65 (Figs. 1c and 1d), much larger deviations are evident.

The effect of grid resolution, time step, and tube length are also illustrated in Fig. 1. Figures 1a–1c show how grid refinement from G1 to G2 affects  $Q$ . At  $\mathcal{V} = 1.5$ , resolving the grid from G1 to G2 results in a slight decrease in the time-asymptotic value of  $Q$ . However, the flow remains steady and axisymmetric. At  $\mathcal{V} = 1.53$ , grid refinement results in a more pronounced transient response,

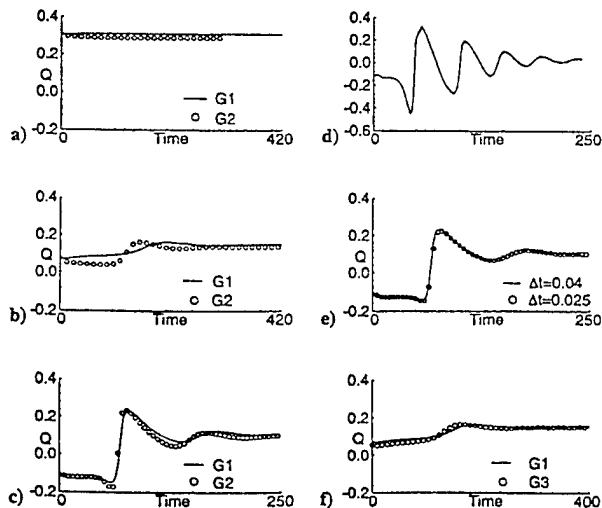


Fig. 1 Temporal behavior of  $Q$ , grid and time-step sensitivity and tube length  $L$  sensitivity: a)  $\mathcal{V} = 1.5$  (G1: coarse grid, G2: fine grid,  $L = 20$ ), b)  $\mathcal{V} = 1.53$ , c)  $\mathcal{V} = 1.55$ , d)  $\mathcal{V} = 1.65$ , e) effect of time step for  $\mathcal{V} = 1.55$ , and f) effect of tube length for  $\mathcal{V} = 1.53$  (G3: coarse grid,  $L = 30$ ).

Received Jan. 31, 1995; revision received May 16, 1995; presented as Paper 95-2310 at the AIAA 26th Fluid Dynamics Conference, San Diego, CA, June 19–22, 1995; accepted for publication Nov. 14, 1995. This paper is declared a work of the U.S. Government and is not subject to copyright protection in the United States.

\*Graduate Student, Department of Aeronautics and Astronautics; currently Research Aerospace Engineer, Flight Control Division, U.S. Air Force Wright Laboratory, 2210 Eighth Street, Suite 11. Member AIAA.

†Associate Professor, Department of Aeronautics and Astronautics. Member AIAA.

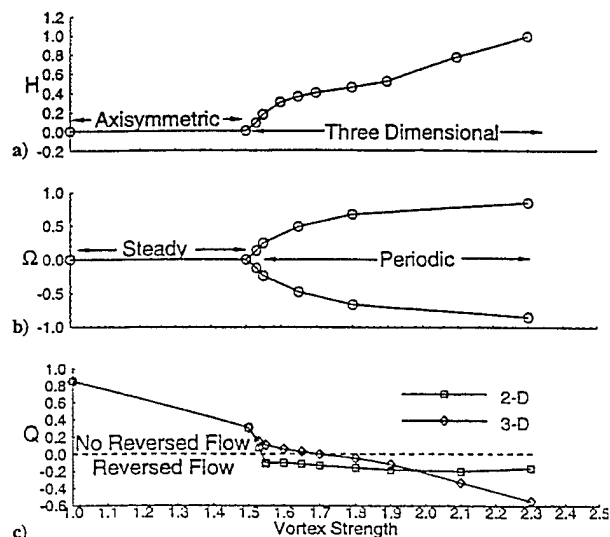


Fig. 2 Evidence of a supercritical Hopf bifurcation.

possibly representing a slight shift of the Hopf point to smaller values of vortex strength. The sensitivity to grid refinement appears to diminish as vortex strength is increased away from the Hopf point, as evident in Fig. 1c. Figure 1e shows that reducing the time step from 0.04 to 0.025, with grid G1, has a negligible influence on the transient behavior of  $Q$ . This suggests that the differences in  $Q$  evident in Figs. 1a–1c are due primarily to grid refinement and not to the reduction of the time step. Finally, the effect of tube length is shown in Fig. 1f, where increasing the tube length  $L$  from 20 to 30 appears to have a small but negligible effect on  $Q$ .

The nature of the Hopf bifurcation is illustrated in Fig. 2. To identify the onset of three-dimensionality, a global parameter  $H$  is constructed and is defined to be the maximum absolute value of  $d\hat{v}/d\theta$ . The term  $H$  is nonzero when the flow is asymmetric. In Fig. 2a,  $H$  abruptly departs from zero between  $V = 1.5$  and 1.53. Within this range of  $V$ , fully three-dimensional solutions bifurcate from the branch of two-dimensional solutions when the two-dimensional solutions become physically unstable. Flow unsteadiness and asymmetry are characterized by another parameter  $\Omega$ , which is defined as the minimum and maximum values of the sum of the cross-plane velocity components along the tube centerline. By definition,  $\Omega$  is zero for an axisymmetric flow. In addition, since the cross-plane velocity components are unsteady, periodic functions (past  $V = 1.5$ ),

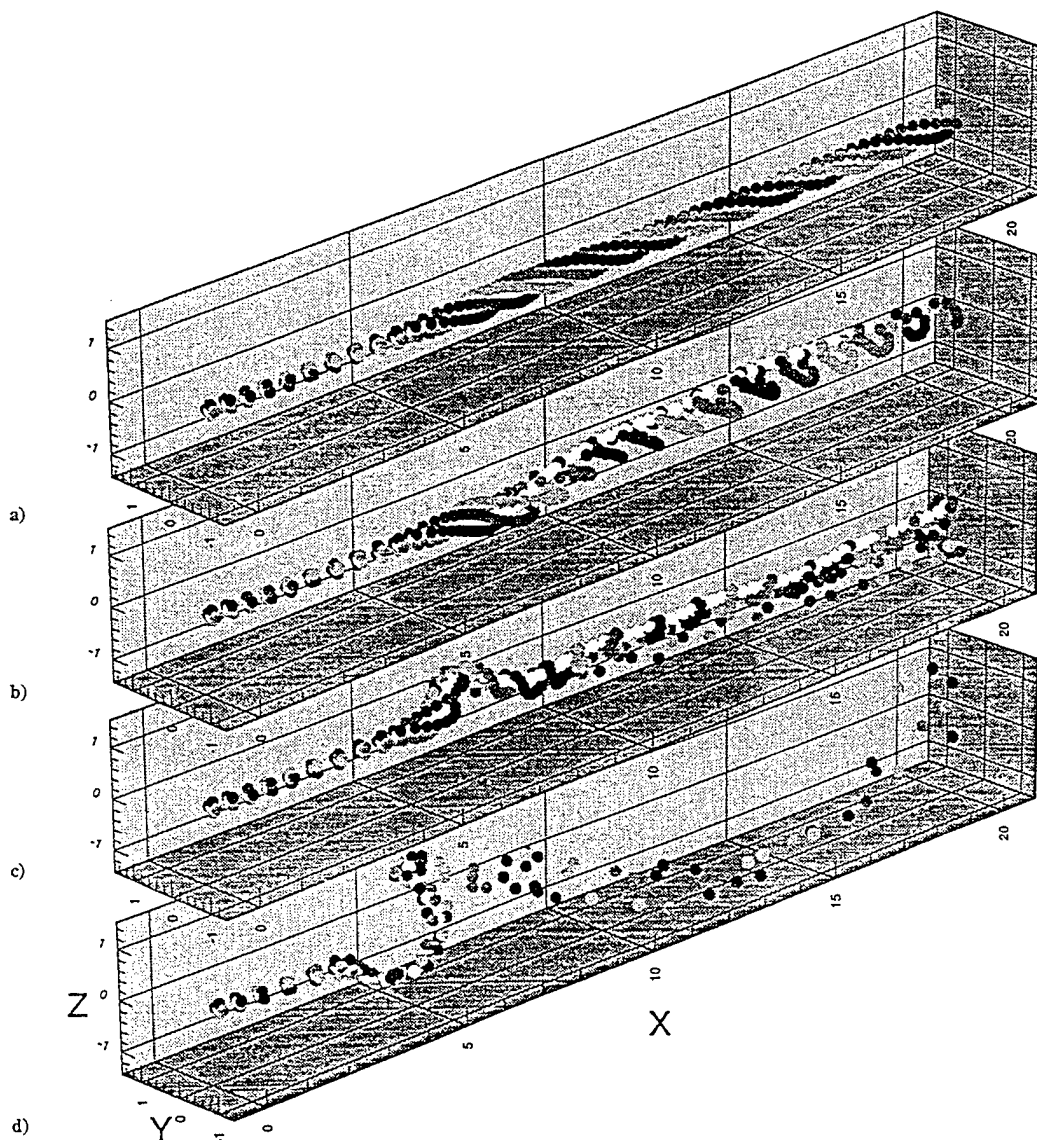


Fig. 3 Particle traces showing development of three-dimensionality with increasing vortex strength: a)  $V = 1.5$ , b)  $V = 1.53$ , c)  $V = 1.65$ , and d)  $V = 2.3$ .

$\Omega$  characterizes the degree of flow unsteadiness by representing the largest amplitude of the cross-plane velocity sum along the centerline. Figure 2b shows that  $\Omega$  departs from zero at the same value of  $V$  that the flow becomes asymmetric. Thus, Figs. 2a and 2b demonstrate that flow unsteadiness and asymmetry are intimately linked. The loss of stability to time-periodic flow is evidence for a Hopf bifurcation. The bifurcation is supercritical,<sup>8</sup> since the amplitude of the disturbance, characterized by  $\Omega$ , grows from zero as  $V$  is increased past the Hopf point. The initial and final values of  $Q$  are shown in Fig. 2c. A region in  $V$  exists where two-dimensional flows with bubble-type breakdown evolve into three-dimensional, unsteady flows with no reversed flow. Also, it is of interest to note that the Hopf point and the appearance of reversed flow occur at different values of  $V$ . Thus, loss of stability is not a consequence of a gross structural change in the flowfield. Other examples in which changes in flowfield topology are dissociated from hydrodynamic bifurcations are given by Lopez.<sup>3</sup>

The observed increase in  $Q$  as the flow transitions from two- to three-dimensional flow is correlated to a particular asymmetric term in the governing equations. Details of this analysis can be found in Ref. 5. The correlation requires concepts put forth by Brown and Lopez<sup>9</sup> and Darmofal.<sup>10</sup> Brown and Lopez<sup>9</sup> established a necessary condition between the production of negative azimuthal vorticity  $\hat{\eta}$  and the extent of axial flow deceleration. Consequently, the authors anticipated that the minimum azimuthal vorticity for the three-dimensional flow would be greater (less negative) than that of the initial two-dimensional flow, since  $Q$  is greater in these cases. This is indeed the case. At  $V = 1.5$ , before the Hopf bifurcation, the minimum values of  $\hat{\eta}$  computed from both the two- and three-dimensional models are virtually the same. However, just beyond the Hopf point, the minimum  $\hat{\eta}$  is significantly greater in the three-dimensional flow. A numerical evaluation of asymmetric terms in the azimuthal vorticity equation is then performed.<sup>5</sup> This equation relates the total derivative of  $\hat{\eta}$  to vorticity stretching and tilting terms.<sup>10</sup> Through this evaluation, it is found that the effect of three-dimensionality on radial vorticity is the principle contributor to the increase in  $\hat{\eta}$ . A region consisting of a positive net change in radial vorticity exists that serves to attenuate the axial deceleration process.

Flowfield visualization is performed by calculating the numerical equivalent of streaklines. Five material points are introduced into the flowfield at the inflow boundary. The white point lies initially on the tube centerline, whereas the grey scaled points lie on the  $y$  and  $z$  axes at nondimensional distances of  $\pm 0.1$  from the centerline. The material point positions are computed in time from the evolving velocity field using a first-order-accurate Euler time integration.<sup>4</sup> Snapshots of the time-asymptotic streaklines are shown in Fig. 3; the tube geometry is omitted for clarity. Figure 3 shows the development of three-dimensional flow as  $V$  is increased past the Hopf bifurcation point. At  $V = 2.3$  (Fig. 3d), the material points deflect off-axis in a well-defined helical-type structure, consistent with spiral-type breakdown. Further discussion of the flow visualization can be found in Ref. 5.

### Conclusions

Time integration of the three-dimensional, compressible Navier-Stokes equations reveals that when the vortex strength is increased past a critical value, the time-asymptotic flow changes from axisymmetric and steady to asymmetric and time periodic, indicating a supercritical Hopf bifurcation. The three-dimensional flows form a solution branch that bifurcates from the path of two-dimensional solutions at the bifurcation point. The authors' interpretation of this result is that the mechanism for the existence of a least one family of three-dimensional solutions, which possess reversed flow at sufficiently large values of vortex strength, is the loss of stability of the axisymmetric base flows. Minimum values of axial velocity  $Q$  are observed to increase as flow asymmetries develop just beyond the Hopf point. Furthermore, a small range of  $V$  exists where two-dimensional solutions exhibit vortex breakdown but three-dimensional solutions do not. This attenuation of axial deceleration is found by the authors to be the result of a positive net production of radial vorticity as flow asymmetries develop.

### References

- <sup>1</sup>Leibovich, S., and Kribus, A., "Large-Amplitude Wavetrains and Solitary Waves in Vortices," *Journal of Fluid Mechanics*, Vol. 216, July 1990, pp. 459-504.
- <sup>2</sup>Beran, P. S., and Culick, F. E. C., "The Role of Non-Uniqueness in the Development of Vortex Breakdown in Tubes," *Journal of Fluid Mechanics*, Vol. 242, Sept. 1992, pp. 491-527.
- <sup>3</sup>Lopez, J. M., "On the Bifurcation Structure of Axisymmetric Vortex Breakdown in a Constricted Pipe," *Physics of Fluids*, Vol. 6, No. 11, 1994, pp. 3683-3693.
- <sup>4</sup>Tromp, J. C., "The Dependence of the Time-Asymptotic Structure of 3-D Vortex Breakdown on Boundary and Initial Conditions," Ph.D. Dissertation, Dept. of Aeronautics and Astronautics, U.S. Air Force Inst. of Technology, Wright-Patterson AFB, OH, 1995.
- <sup>5</sup>Tromp, J. C., and Beran, P. S., "Temporal Evolution of Three-Dimensional Vortex Breakdown from Steady, Axisymmetric Solutions," AIAA Paper 95-2310, June 1995.
- <sup>6</sup>Lele, S. K., "Compact Finite Difference Schemes with Spectral-Like Resolution," *Journal of Computational Physics*, Vol. 103, Nov. 1992, pp. 16-42.
- <sup>7</sup>Faler, J. H., and Leibovich, S., "Disrupted States of Vortex Flow and Vortex Breakdown," *Physics of Fluids*, Vol. 20, No. 9, 1977, pp. 1385-1400.
- <sup>8</sup>Seydel, R., *From Equilibrium to Chaos: Practical Bifurcation and Stability Analysis*, Elsevier, New York, 1988.
- <sup>9</sup>Brown, G., and Lopez, J., "Axisymmetric Vortex Breakdown, Part 2: Physical Mechanisms," *Journal of Fluid Mechanics*, Vol. 221, Dec. 1990, pp. 553-576.
- <sup>10</sup>Darmofal, D. L., "The Role of Vorticity Dynamics in Vortex Breakdown," AIAA Paper 93-3036, July 1993.

# The role of nonunique axisymmetric solutions in 3-D vortex breakdown

J. C. Tromp and P. S. Beran

*Department of Aeronautics and Astronautics, U.S. Air Force Institute of Technology,  
Wright-Patterson Air Force Base, Ohio 45433*

(Received 19 January 1996; accepted 11 December 1996)

The three-dimensional, compressible Navier–Stokes equations in primitive variables are solved numerically to simulate vortex breakdown in a constricted tube. Time integration is performed with an implicit Beam–Warming algorithm using fourth-order compact operators to discretize spatial derivatives. Initial conditions are obtained by solving the steady, compressible, and axisymmetric form of the Navier–Stokes equations with Newton’s method. The effects of three-dimensionality on flows that are initially axisymmetric and stable to 2-D disturbances are examined. Stability of the axisymmetric base flow is assessed through 3-D time integration. Axisymmetric solutions at a Mach number of 0.3 and a Reynolds number of 1000 contain a region of nonuniqueness. Within this region, 3-D time integration reveals only unique solutions, with nonunique axisymmetric initial conditions converging to a unique solution that is steady and axisymmetric. Past the primary limit point, which approximately identifies the appearance of critical flow (a flow that can support an axisymmetric standing wave), the solutions bifurcate into 3-D time-periodic flows. Thus this numerical study shows that the vortex strength associated with the loss of stability to 3-D disturbances and that of the primary limit point are in close proximity. Additional numerical and theoretical studies of 3-D swirling flows are needed to determine the impact of various parameters on dynamic behavior. For example, it is possible that a different flow behavior, leading to a nearly axisymmetric vortex breakdown state, may develop with other inlet profiles and tube geometries. [S1070-6631(97)02804-3]

## I. INTRODUCTION

Vortex breakdown is a hydrodynamic feature of swirling flows in which the rotational vortex core stagnates, resulting in a dramatic increase in the core size. Breakdown can occur in tornadoes, in swirling flows inside tubes, in wing trailing vortices, and in the vortical flows produced over delta wings at high incidence.

Many numerical studies of vortex breakdown rely on the assumption of a steady flow which is symmetric about the vortex-core axis. This simplification allows researchers to study the nearly axisymmetric bubble form of breakdown found in tube experiments,<sup>1</sup> while avoiding the computational burden of solving 3-D flowfields. Some of the more recent studies of axisymmetric breakdown are by Buntine and Saffman,<sup>2</sup> Wang and Rusak,<sup>3,4</sup> Lopez,<sup>5</sup> Darmofal and Murman,<sup>6</sup> and Beran and Culick,<sup>7</sup> hereafter denoted as BC.

Three-dimensional vortex breakdown computations have also been reported. These computations have provided valuable information on the topological structure of the various 3-D breakdown forms. Most notably, calculations have been performed for flows in unconfined domains<sup>8–10</sup> and over delta wings.<sup>11</sup> These works provide descriptions of the various time-asymptotic breakdown structures encountered, such as the spiral and bubble forms. Spall and Gatski<sup>10</sup> compute other flow disturbances in addition to the spiral and bubble breakdowns, as documented in the tube experiments of Faler and Leibovich.<sup>1</sup>

An interesting feature of axisymmetric swirling flows is the appearance of nonunique solutions for a fixed set of flow parameters. Táasan<sup>12</sup> and Leibovich and Kribus<sup>13</sup> computed solutions to the Euler equations and found multiple solutions stemming from bifurcations of columnar flows. BC further

demonstrated that nonunique flows exist as solutions of the Navier–Stokes equations. These results also indicate a connection between the appearance of reversed flow and the passage of a limit point. The stability of the BC solutions were confirmed by Lopez<sup>5</sup> and Beran<sup>14</sup> by solving the time-dependent form of the 2-D governing equations. Lopez<sup>5</sup> concluded that the appearance of multiple solutions precludes the possibility of predicting breakdown solely from knowledge of the upstream flow. Rusak and Wang<sup>15</sup> recently applied a global variational analysis to incompressible, inviscid flows. They proved that both a columnar flow and a flow with a large stagnation zone can coexist within a specified range of vortex strength. These two solutions, which are stable to small axisymmetric disturbances, are connected by an unstable branch of solutions.

Nonuniqueness in 3-D swirling flows has also been reported. The tube experiments of Sarpkaya<sup>16</sup> show hysteresis resulting from the existence of both the bubble and spiral forms of breakdown under identical flow conditions. Similar experiments by Faler and Leibovich<sup>1</sup> show spontaneous switching between the spiral and bubble forms without hysteresis. Nonuniqueness in delta-wing flow computations is discussed by Visbal.<sup>11</sup>

The role of nonunique axisymmetric solutions in the development of 3-D swirling flows is the subject of this work. The authors have previously investigated the stability of unique axisymmetric solutions to three-dimensional disturbances.<sup>17</sup> A unique feature of this work and the current work is that solutions to the steady, axisymmetric governing equations are used as initial conditions for time-integration of the 3-D equations of motion. Thus transient solutions which deviate away from the initial condition do so as a

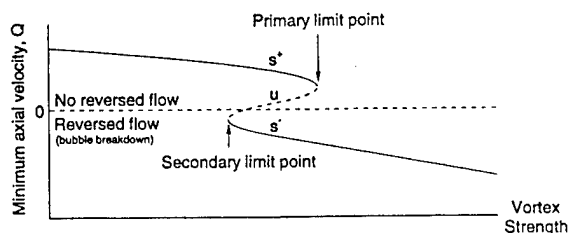


FIG. 1. A representative solution branch of axisymmetric solutions: stable branch (solid lines); unstable branch (dashed line).

direct consequence of three-dimensional disturbances. Time-asymptotic 3-D solutions are compared, under identical parameter settings, to the 2-D initial condition. In this way, the relevancy of 2-D solutions is revealed. A cylindrical tube geometry is used, since it should naturally give rise to an axisymmetric flow for a sufficiently low vortex strength. This allows for a clean identification of the emerging vortex core asymmetries and an understanding of their role in the development of breakdown.

A characterization of nonunique solutions for viscous, steady and axisymmetric flow is shown in Fig. 1, plotted in terms of the (global) minimum axial velocity component,  $Q$ , and the vortex strength,  $\mathcal{V}$ . The solid lines represent solutions that are stable to axisymmetric disturbances, while the dashed line represents unstable ( $u$ ) solutions. As the vortex strength is increased, a fold in the solution space occurs along the upper stable branch ( $s^+$ ), resulting in a primary limit point denoted as  $\mathcal{V}_p$ . As the vortex strength is slightly increased from  $\mathcal{V}_p$ ,  $Q$  abruptly changes from positive to negative, indicating the formation of bubble breakdown. For flows with breakdown along the lower stable branch ( $s^-$ ), decreasing the vortex strength results in generally larger (less negative) values of  $Q$  until the secondary limit point,  $\mathcal{V}_s$ , is encountered. The nonuniqueness of solution paths as the vortex strength is increased and then decreased results in a hysteresis loop. Between  $\mathcal{V}_s$  and  $\mathcal{V}_p$ , nonunique axisymmetric solutions exist.

The primary limit point in an axisymmetric solution space has been associated with the appearance of critical flow—a flow state which supports standing axisymmetric waves.<sup>18</sup> A supercritical flow therefore refers to a flow which can only support the downstream propagation of axisymmetric waves, while subcritical flows can support either upstream or downstream wave propagation. BC found that for sufficiently high Reynolds numbers, a parabolized version of the axisymmetric governing equations, known as the quasi-cylindrical (QC) equations, agree well with solutions of the Navier–Stokes equations when the vortex strength is below the primary limit point. However, the solutions fail to converge as the vortex strength is increased towards the primary limit point. The failure point of the parabolic QC equations is believed by Hall<sup>19</sup> to be the approximate point at which critical flow develops. Thus, the works of BC and Hall<sup>19</sup> suggest that the flow transitions from supercritical flow to subcritical flow at a vortex strength which is approximately equal to  $\mathcal{V}_p$ . More recently, a noncolumnar flow criticality analysis

has been reported by Wang and Rusak<sup>4</sup> for 2-D, inviscid flow. Their results indicate that the critical vortex strength for a finite length tube is a point of exchange of stability for both columnar and noncolumnar solution branches, and that this critical point corresponds<sup>3</sup> to a transcritical bifurcation point of the inviscid solution branches. Furthermore, an extension of their work to flows with slight viscosity<sup>15</sup> confirms the existence of limit-point behavior found previously in numerical solutions of the Navier–Stokes equations. The primary limit point forms at a slightly lower vortex strength than the transcritical bifurcation point, with the spacing between the two determined largely by the magnitude of the viscosity. The primary limit point is also expected<sup>15</sup> to be a point of exchange of stability to axisymmetric disturbances.

The computational approach of the current study is as follows. First, a numerical algorithm provides the axisymmetric initial condition for a specified vortex strength,  $\mathcal{V}$ , given fixed values of the freestream Mach number,  $M$ , and the Reynolds number,  $Re$ . The axisymmetric solution is then interpolated onto a 3-D mesh using a fourth-order-accurate cubic-spline scheme.<sup>20</sup> Then, time-integration is carried out by a 3-D time-integration algorithm. Initial conditions are computed using the pseudo-arclength continuation (PAC) model of BC modified for compressible flow. The PAC model is capable of computing solution paths with folds, providing a one-parameter (vortex strength) family of axisymmetric solutions. The nominal Mach number,  $M=0.3$ , was chosen to provide “near incompressibility” while avoiding convergence problems associated with computing at low Mach numbers. The 3-D time-integration model, referred to as the Time-Accurate Navier–Stokes (TANS) model, is developed specifically for this work and is described in the next section and in the Appendix.

## II. NUMERICAL MODEL

The TANS model incorporates two unique features. First, it uses a multiblock grid structure in the crossflow plane. The multiblock structure allows for a nearly Cartesian arrangement of nodes in the vicinity of the centerline, while maintaining near orthogonality at the circular tube wall. This is done for two reasons: (1) to allow for nearly constant grid resolution near the centerline, where the vortex core may migrate off-center during spiral breakdown; and (2) to avoid an approximate numerical treatment at the tube centerline. Second, the TANS model incorporates fourth-order compact operators into an approximate factorization, Beam-Warming solution procedure. The compact scheme discretizes explicit spatial derivatives to fourth-order accuracy. Central-difference discretizations are typically second-order accurate. The net reduction in CPU time using the compact scheme over central differencing, assuming fewer required nodes to achieve similar levels of accuracy, is about 42%.

### A. Tube geometry and grid

A Cartesian ( $x, y, z$ ) and a cylindrical ( $\hat{z}, r, \theta$ ) coordinate system are referenced such that positive  $x$  and  $\hat{z}$  are aligned with the tube centerline and pointed downstream. The  $y$  and  $z$  directions lie in a crossplane normal to  $x$  and form a right-

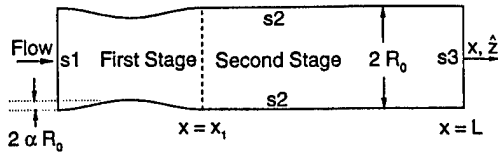


FIG. 2. Schematic of tube geometry in an arbitrary  $(\hat{z}, r)$  plane.

handed system. The Cartesian velocity components are denoted by  $V = (u, v, w)^T$ . The  $r$  and  $\theta$  directions are oriented such that  $\theta = 0$  corresponds to  $r = +y$ . The axial, radial and azimuthal velocity components are denoted by  $(\hat{w}, \hat{u}, \hat{v})$ , respectively.

The physical domain consists of a two-stage cylindrical tube of circular cross-section and varying radius<sup>7</sup> (Fig. 2). The radius of the inlet station is denoted as  $R_0$ . The radius of the first stage is given by

$$R(x) = R_0 + \alpha R_0 [\cos(2\pi x/x_1) - 1] \quad (0 \leq x \leq x_1), \quad (1)$$

where  $x_1$  is the length of the first stage. The parameter  $\alpha$  controls the amount of tube contraction. The values of  $\alpha$  and  $x_1$  are fixed for this work at 0.05 and 6.18, respectively. The second stage of the tube has a constant tube radius of  $R_0$ . The domain boundaries are denoted by s1, s2, and s3; corresponding to the inflow, wall, and outflow boundaries, respectively (Fig. 2). A generalized mapping transforms the physical coordinates  $(x, y, z)$  to the computational coordinates  $(\xi, \eta, \zeta)$ . Node indices in the  $(\xi, \eta, \zeta)$  coordinates are denoted by  $(i, j, k)$ , respectively. The number of nodes in the  $(\xi, \eta, \zeta)$  coordinate directions are  $(n_x, n_y, n_z)$ , respectively.

A crossplane of the multiblock grid is shown in Fig. 3(a) for  $n_y = n_z = 41$ . The grid consists of an inner block surrounded by four outer blocks [Fig. 3(b)]. The outer blocks are physically connected to each other but contain two edges each that are considered as branch cuts in the computational domain. These cuts are labeled 1–4 in Fig. 3(b). The 2-D crossplane grid is generated with the GRIDGEN (Ref. 21) software package. The 3-D grids are generated by scaling the crossplane grid to the local tube radius. Clustering is allowed in the  $x$  direction. The axial node locations are computed from  $x_i = x_{i-1} + \Delta x_i$ , where

$$\Delta x_i = \Delta x_0 (1 + \beta [\cos(2\pi x_{i-1}/x_2) - 1]) \quad (0 \leq x \leq x_2). \quad (2)$$

The parameters  $\beta$  and  $x_2$  control the amount and axial extent of clustering, respectively. For  $x = 0$  and  $x > x_2$ ,  $\Delta x_i = \Delta x_0$ .

## B. Governing equations

The nondimensional vector form of the Navier–Stokes equations is written below. The fluid density and pressure are denoted by  $\rho$  and  $p$ , respectively, to define the solution vector  $U \equiv (\rho, u, v, w, p)^T$ . For algorithm efficiency, the equations are written in nonconservative form, limiting the scheme to subsonic flow. The reference length is the inlet radius of the vortex core. The reference velocity is the (uniform) inflow axial velocity and the reference pressure is twice the reference dynamic pressure

$$U_t + \mathcal{A}U_\xi + \mathcal{B}U_\eta + \mathcal{C}U_\zeta = D/\rho,$$

$$\mathcal{A} = I_1 \xi_x, \quad \mathcal{B} = I_1 \eta_x + I_2 \eta_y + I_3 \eta_z,$$

$$\mathcal{C} = I_1 \zeta_x + I_2 \zeta_y + I_3 \zeta_z,$$

$$I_m = \begin{bmatrix} V_m & \rho \delta_{1m} & \rho \delta_{2m} & \rho \delta_{3m} & 0 \\ 0 & V_m & 0 & 0 & \delta_{1m}/\rho \\ 0 & 0 & V_m & 0 & \delta_{2m}/\rho \\ 0 & 0 & 0 & V_m & \delta_{3m}/\rho \\ 0 & \gamma p \delta_{1m} & \gamma p \delta_{2m} & \gamma p \delta_{3m} & V_m \end{bmatrix},$$

where  $\delta_{lm}$  is the Kronecker delta function for  $l, m = 1, 2, 3$  and  $D = [0, \nabla \cdot \vec{\tau}, \rho \{(\gamma - 1)\Phi - \nabla \cdot \vec{q}\}]^T$ . The nondimensional shear stress tensor,  $\vec{\tau}$ , is defined assuming Stokes' hypothesis.  $\Phi$  and  $\vec{q}$  represent the nondimensional viscous dissipation and heat flux vector, respectively. The auxiliary equations necessary to close the system of equations come from the assumption of a perfect gas and Sutherland's formula.

Axisymmetric conditions are specified at the inflow boundary plane, s1. The inlet axial velocity,  $u = \hat{w}$ , is chosen to be uniform. Boundary conditions on  $v$  and  $w$  are obtained by specifying appropriate profiles for  $\hat{v}$  and  $\hat{u}$ . The following swirl velocity profile is characteristic of a Burger type vortex and is appropriate for modeling the profiles obtained from a swirl-vane apparatus:<sup>1</sup>

$$\hat{v}(0, r) = \mathcal{V} r^{-1} (1 - e^{-r^2}) = \Gamma r^{-1},$$

where  $\mathcal{V}$  is the vortex strength along s1 and  $\Gamma$  is the circulation (divided by  $2\pi$ ). The radial velocity,  $\hat{u}$ , is assumed to vanish to reflect a columnar flow state. A nonuniform inflow density profile based on columnar flow is prescribed as a Dirichlet condition. The profile is obtained by solving the axisymmetric Navier–Stokes equations with the PAC algorithm in a straight tube of short axial extent ( $L = 0.01$ ). Inflow and outflow conditions are enforced that dictate columnar flow. These conditions consist of fixed velocity components (given above) with  $p_x = p_z = 0$ . The resulting columnar solution for density is then used as a Dirichlet boundary condition. A boundary condition on pressure is obtained by solving the steady form of the axial momentum equation along the inflow plane. The constriction in the first stage of

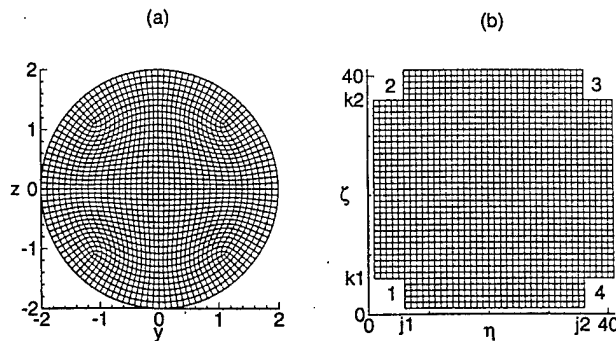


FIG. 3. Crossplane grid: (a) physical, (b) computational.

the tube provides a favorable pressure gradient in the converging section, while an adverse gradient forms aft of the throat. Thus the constriction keeps the breakdown from occurring near  $s1$ , where columnar conditions are enforced. A second inlet condition of zero azimuthal vorticity is briefly considered, implying a vanishing axial derivative of radial velocity for a uniform axial velocity profile. This condition relaxes the columnar flow assumption, allowing for a comparison of results between two inflow conditions. The columnar conditions are assumed unless otherwise noted. Surface  $s2$  is assumed to be a slip-wall, yielding an impermeability boundary condition which relates the axial and radial velocities. Two other conditions, based on the compressible Bernoulli equation and the assumption of constant wall circulation, lead to three Dirichlet conditions for the velocity components at the wall. A fixed wall temperature is also assumed. The wall pressure is determined by solving the steady form of the  $y$  and  $z$  momentum equations. The  $y$  momentum equation is solved in the  $\eta$  sweep and the  $z$  momentum equation is solved in the  $\zeta$  sweep. Solution sweeps are discussed in the Appendix. Outflow conditions at  $s3$  are chosen to reflect an assumed columnar flow state. Details of the boundary condition formulation can be found in Ref. 20.

### III. RESULTS

The following results show that steady solutions occur when the vortex strength is prescribed to be less than the primary limit point. In particular, the specification of three nonunique, axisymmetric initial conditions (at a vortex strength between the primary and secondary limit points) lead to three apparently identical time-asymptotic solutions which are steady and axisymmetric. When the vortex strength is prescribed to be greater than the primary limit point, a time-periodic, three-dimensional solution develops. The change in solution behavior is attributed to a Hopf bifurcation, which is found to lie in very close proximity to the primary limit point.

A Reynolds number of 1000 is considered following the results of BC, who show that nonunique 2-D solutions exist for incompressible flow when  $Re > 360$ . Consistent results are found for  $M = 0.3$ . Only unique axisymmetric solutions were evident in previous results at  $Re = 250$ ,<sup>17</sup> while a region of nonunique solutions are found at  $Re = 500$  (Ref. 20) and  $Re = 1000$ . The vortex strength difference between primary and secondary limit points is 0.0019 and 0.015 for  $Re = 500$  and  $Re = 1000$ , respectively. BC report limit point separations for  $M = 0$  of about 0.012 and 0.04 for  $Re = 500$  and  $Re = 1000$ , respectively, which are greater than those found here for  $M = 0.3$ . Thus compressibility effects appear to diminish the region of nonuniqueness for a given Reynolds number.

#### A. Grid requirements

Grid requirements for 2-D swirling flows have been discussed in previous work by BC, Lopez,<sup>5</sup> and Darmofal and Murman.<sup>6</sup> Each of these works, along with the current study, consider the constricted tube geometry defined by BC. More specifically, the outer tube radius is governed by Eq. (1),  $\alpha = 0.05$  and  $R_0 = 2$ . Darmofal and Murman<sup>6</sup> also consider a

second tube constriction near the outflow boundary. BC demonstrate solution insensitivity by prescribing  $27 \times 301$  nodes for  $R_0 = 2$  and  $L = 30$ . Some sensitivity between tube lengths  $L = 30$  and  $L = 60$  are noted at  $Re = 2000$ , which is higher than the  $Re = 1000$  flows considered here. Similarly, Lopez<sup>5</sup> used  $31 \times 301$  nodes for  $R_0 = 2$  and  $L = 30$ . Further resolution of this grid to  $61 \times 601$  removed the appearance of spatially developing "wiggles" in contours of azimuthal vorticity. However, Lopez<sup>5</sup> points out that the differences between the  $31 \times 301$  solutions and the  $61 \times 601$  solutions are not significant for  $Re \leq 1000$ . In particular, plots of the streamfunction and circulation for the two grids were described as being virtually indistinguishable. BC also found that reducing the number of axial nodes from 301 to 151 axial nodes had very little effect on the solution paths, except that solution convergence suffered near the secondary limit point. Darmofal and Murman<sup>6</sup> used  $31 \times 151$  nodes for  $R_0 = 2$  and  $L = 30$  to compute solutions at  $Re = 1000$ .

Grid requirements are obviously greater for the current 3-D flows. However, using the fourth-order compact operators provides some relief by allowing similar accuracy levels with fewer nodes. In this study a fine grid is constructed with  $61 \times 61 \times 172$  nodes for  $R_0 = 2$  and  $L = 30$ . This grid is equivalent in crossplane resolution to the above grids. Grid clustering in the axial direction is employed [ $\Delta x_0 = 0.206$ ,  $\beta = 0.25$ , and  $x_2 = 10$ ; Eq. (2)] near the aft portion of the throat such that the spacing at  $x = 5$  is one-half the spacing achieved with equally spaced nodes. Thus the minimum grid spacing in the breakdown region is comparable to the spacing achieved with 301 equally spaced nodes. Using the fourth-order compact operators further enhances accuracy. Results in Ref. 20 show that this level of axial resolution is adequate for  $Re \leq 1000$ . A time step of  $\Delta t = 0.025$  is used, based on time-accuracy requirements identified in Ref. 20.

Varying the tube length from  $L = 20$  to  $L = 30$  results in large differences in  $Q$  when the vortex strength is greater than the primary limit point and when  $Re = 1000$ . However, a tube length of  $L = 20$  was found to be adequate for  $Re = 250$ ,<sup>17</sup>  $Re = 500$ ,<sup>20</sup> and for sufficiently low values of vortex strength at  $Re = 1000$ . The observed sensitivity to tube length prompted all runs computed for  $Re = 1000$  to be run with  $L = 30$ . A further extension of the tube to  $L = 40$  shows that only small deviations in  $Q$  occur from the  $L = 30$  solution.<sup>20</sup>

Values of tube radius other than  $R_0 = 2$  are not considered in this study. BC found that paths of axisymmetric solutions near the primary limit point are insensitive to tube radius between  $R_0 = 2$  and  $R_0 = 3$  for Reynolds numbers ranging from 250 to 2000. However, some sensitivity in the bifurcation point locations of inviscid, axisymmetric solution branches to the vortex core/tube radius ratio have been reported.<sup>22</sup> At vortex strengths much higher than the primary limit point ( $\mathcal{Q}$  as high as 2.3), 3-D flows were computed<sup>20</sup> at  $Re = 250$ , without the anticipated formation of the bubble form of breakdown.<sup>1</sup> Bubble breakdowns were instead only observed as transient solutions, and ultimately transformed to one of the asymmetric (spiral) modes. Evidence of the transient bubble form suggests that the level of grid resolution is adequate to resolve the bubble breakdown. Instead,



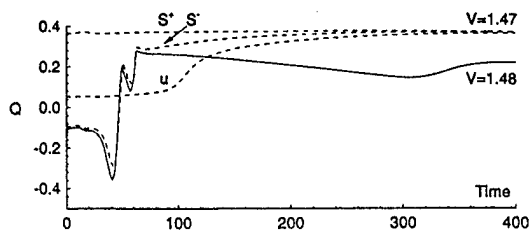


FIG. 4.  $Q$  versus time:  $\mathcal{V} < \mathcal{V}_p$  (dashed),  $\mathcal{V} > \mathcal{V}_p$  (solid).  $\mathcal{V}_p = 1.47435$ .

the authors speculate that the relatively small value of the tube radius,  $R_0 = 2$ , is insufficient to produce a 3-D time-asymptotic bubble form of breakdown at high vortex strengths. The basis for this belief is the observation that flowfield perturbations near the tube wall are larger for 3-D solutions than for 2-D solutions. Thus, further computations with the model should consider larger values of tube radius to determine if the wall is preventing the occurrence of the 3-D bubble breakdown at large values of  $\mathcal{V}$ . It is of interest to note that a small, but steady, axisymmetric bubble was computed with the TANS model for a much lower Reynolds number of 50.

## B. Temporal behavior

Six axisymmetric initial conditions are time-integrated with the TANS model for  $Re = 1000$ . Three of these initial conditions lie before the primary limit point at  $\mathcal{V}_p = 1.47435$ . These nonunique solutions lie on the upper stable branch ( $\mathcal{V} = 1.47^{s+}$ ), the unstable branch ( $\mathcal{V} = 1.47^u$ ), and the lower stable branch ( $\mathcal{V} = 1.47^{s-}$ ). The remaining solutions are obtained at  $\mathcal{V} = 1.48$ ,  $\mathcal{V} = 1.5$ , and  $\mathcal{V} = 1.6$ , which are all greater than  $\mathcal{V}_p$ .

The temporal behavior of  $Q$  for  $\mathcal{V} = 1.47$  and  $1.48$  is shown in Fig. 4. It is evident that the flow temporally evolves from a negative to a positive value of  $Q$  for  $\mathcal{V} = 1.47^{s-}$ ,  $\mathcal{V} = 1.47^u$  and  $\mathcal{V} = 1.48$ , indicating the elimination of a reversed flow region. Furthermore, the three runs computed before the primary limit point (dashed lines in Fig. 4) all migrate to apparently identical solutions near the initial condition at  $\mathcal{V} = 1.47^{s+}$ . This behavior signifies the loss of 2-D solution nonuniqueness in the presence of three-dimensional disturbances. When  $\mathcal{V}$  is increased slightly to  $1.48$ , the temporal behavior of  $Q$  departs from the behavior at  $\mathcal{V} = 1.47^{s-}$  near  $t = 70$ . The time-asymptotic value of  $Q$  ( $0.195$  at  $t = 1000$ ) for  $\mathcal{V} = 1.48$  is lower than the time-asymptotic values computed before the primary limit point at  $\mathcal{V} = 1.47$ , but is higher than the initial 2-D value. Thus, the initially steady, axisymmetric bubble breakdown solution is replaced by a flow without breakdown when three-dimensionality is allowed.

The dynamics of the  $\mathcal{V} = 1.47^{s-}$  case is examined to better understand the evolution from axisymmetric bubble breakdown to nearly columnar flow. The numerical equivalent of streaklines are computed for this run to provide a visual representation of the flowfield. Five "material points" are introduced into the flowfield at the inflow boundary. One point (black) lies initially on the tube centerline, the others (gray scaled) lie on the  $y$  and  $z$  axes at a fixed offset from the

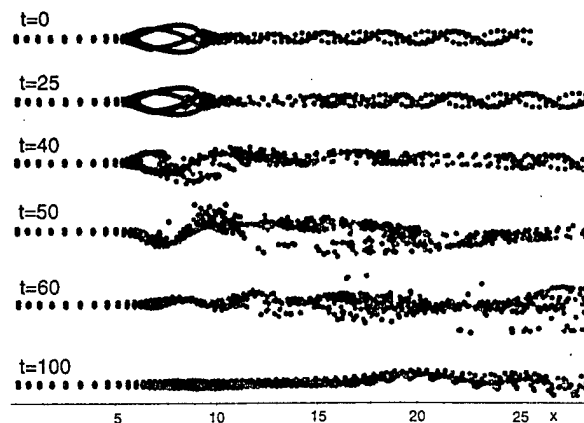


FIG. 5. Streaklines showing transition from axisymmetric bubble breakdown to nearly columnar flow:  $\mathcal{V} = 1.47^{s-}$ ,  $Re = 1000$ .

centerline. Five new material points are periodically introduced into the flowfield where the first five points were initialized, thereby simulating a numerical equivalent of die-injection in experiments. Material point positions are computed in time from the evolving velocity field using a first-order-accurate Euler time integration.<sup>20</sup> Initial streaklines ( $t = 0$ ) are computed from the initially steady flowfield. When the material points are initially offset from the centerline a nondimensional distance of  $0.1$ , the resulting streaklines convect over the bubble breakdown region and downstream. However, if the initial offset is  $0.01$ , material points pass over the bubble and then enter the bubble region from the rear. Both offsets are considered to allow material point visualizations inside and outside the bubble.

Examination of the streaklines at discrete points in time reveal that the initially axisymmetric bubble breakdown erupts temporarily into a 3-D spiral flow, followed by a decay of three-dimensionality to the nearly columnar solution along the  $s^+$  branch. Furthermore, the instability associated with the appearance of 3-D flow appears greatest just aft of the breakdown bubble.

The emergence and decay of 3-D flow is illustrated in Fig. 5. At  $t = 0$ , the bubble is clearly evident by streaklines which pass around the bubble region and convect downstream. The bubble structure remains intact through  $t = 25$ . However, as discussed later, it is found that asymmetries have developed both within and aft of the bubble region by  $t = 25$  and have significantly altered the flow inside the bubble. Thus the material points shown in Fig. 5 do not provide a total picture of the emerging 3-D flow. By  $t = 40$ , the aft portion of the bubble is replaced with a loosely organized spiral arrangement of material points. The material points upstream and slightly downstream of the nose of the bubble remain nearly undisturbed. By  $t = 50$ , a spiral structure replaces the bubble entirely, and then slowly transitions over time to nearly columnar flow. By  $t = 60$ , the original location of the nose of the bubble is replaced with nearly columnar flow. The axial extent of the nearly columnar flow increases downstream with time as evidenced by the streaklines at  $t = 100$ . The flow becomes steady and nearly columnar everywhere by  $t = 400$ .



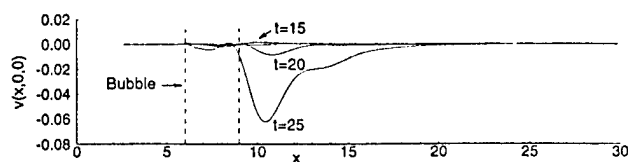


FIG. 6. Centerline values of the  $y$  velocity component,  $v$ , versus  $x$  for various times,  $t$ :  $\mathcal{V}^* = 1.47^*$ ,  $Re = 1000$ .

The emergence of 3-D flow aft of the bubble is illustrated in Fig. 6, where the centerline value of the  $y$  velocity component,  $v$ , is plotted versus  $x$  at various times. Note that nonzero centerline values of  $v$  imply 3-D flow. The location of the breakdown bubble is marked in the figure by two vertical dashed lines. It is found that below  $t=5$ , small asymmetries,  $v \approx \mathcal{O}(10^{-5})$ , exist slightly upstream and downstream of the bubble region. As  $t$  is increased, the asymmetries upstream of the bubble grow to only  $\mathcal{O}(10^{-4})$ . Within and especially aft of the bubble region, however, asymmetric flow develops quickly. By  $t=25$ , asymmetric flow extends from the front portion of the bubble region to as far downstream as  $x=20$ . This asymmetric flow develops before any obvious signs of their existence appears in the streaklines of Fig. 5.

The streaklines shown in Fig. 7 convect upstream into the interior of the bubble, and help visualize the impact of the emerging asymmetric flow. Between  $t=0$  and  $t=5$  the bubble structure remains basically unchanged from the initial

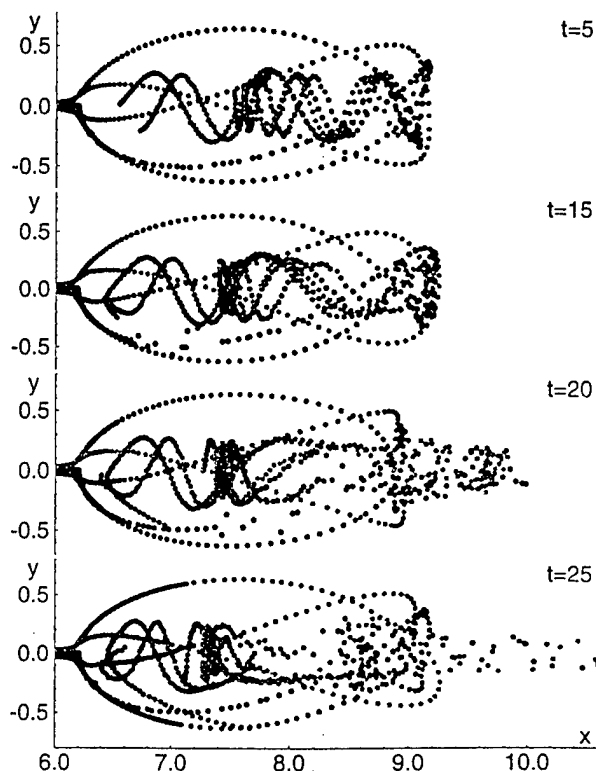


FIG. 7. Streaklines showing flow reversal into the breakdown bubble and subsequent affect of emerging flow asymmetries:  $\mathcal{V}^* = 1.47^*$ ,  $Re = 1000$ .

condition, with all material points entering the bubble from the rear and spiraling upstream. By  $t=15$ , two changes to the aft portion of the bubble are apparent. First, the spiraling material points within the bubble between approximately  $x=8$  and  $x=9$  are not as tightly wrapped as before. This is found to be associated with the elimination of reversed flow near the rear of the bubble. Second, the rear of the bubble appears to have shifted slightly downstream. By  $t=20$ , reversed flow is lost in the downstream half of the bubble interior, and the ejection of material points out of the bubble interior is evident. Furthermore, three-dimensional flow is now clearly evident from the material points. By  $t=25$ , the region of reversed flow along the centerline is contained to the region between the nose of the bubble and  $x \approx 7$ .

The dynamic behavior illustrated above in Figs. 5–7 demonstrates the instability of the initial axisymmetric flow along the  $s^-$  branch to 3-D disturbances. Furthermore, the instability is strongest just aft of the breakdown bubble (Fig. 6).

The explanation for the subsequent decay of the 3-D disturbances, however, is not clear. A possible explanation is as follows. A large increase in  $Q$  is observed between  $t \approx 40$  and  $t \approx 50$  (Fig. 4), and is found to coincide with the largest growth of flow asymmetries. The increase in  $Q$  may be a direct result of the emerging 3-D flow, as was found in previous work by the authors.<sup>17</sup> As a result of increasing  $Q$ , the flow may reach a point in time where the underlying axisymmetric base flow is no longer unstable to 3-D disturbances. [It is of interest to note that flow asymmetries begin to diminish at a point in time ( $t \approx 47$ ) when  $Q$  switches sign from negative to positive.] This would then cause the subsequent decay of the spiral formation in Fig. 5 to axisymmetric flow. However, the strongest attracting axisymmetric solution is now the nearly columnar solution along the  $s^+$  branch. In summary, solutions along  $s^-$  are unstable to 3-D disturbances. The emerging asymmetries are associated with an increase in  $Q$  (i.e., away from the  $s^-$  branch) until a sufficiently high value of  $Q$  is reached. At this value of  $Q$ , it is postulated that the base flow can no longer support asymmetric disturbances. The solution would then be attracted to the nearly columnar,  $s^+$ , branch.

A similar scenario may exist for a flow computed along the  $s^-$  branch past the primary limit point. In this case, however, there is no attracting  $s^+$  solution available, providing the scenario for a new branch of solutions to form.

### C. Evidence for a Hopf bifurcation near the primary limit point

The time-asymptotic behavior of the flows computed near the primary limit point is discussed here and compared to the initial flow state. The time-asymptotic behavior of the flows computed before the primary limit point  $\mathcal{V}^* < \mathcal{V}_p^*$  is steady and axisymmetric. Flow steadiness is confirmed by monitoring the global maximum value of the solution increment,  $\Delta^n U$ , as time increases. All of the runs computed before the primary limit point converge to maximum values of  $\Delta^n U$  near  $1 \times 10^{-6}$  at  $t = 400$ , which is considered an acceptable level of convergence. The time-asymptotic solutions are found to be axisymmetric by computing the value of  $H$ ,

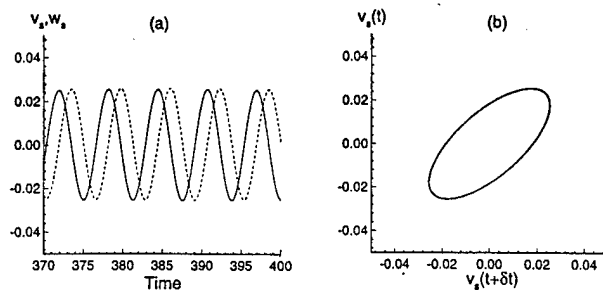


FIG. 8. Periodic behavior of flow computed at  $\mathcal{V}=1.5$  and  $Re=1000$ : (a)  $v_s$  (solid) and  $w_s$  (dashed) versus time, (b) phase plot of  $v_s$  for  $t=370$  to  $t=400$ .

which characterizes the degree of flow asymmetry and is defined as the global maximum absolute value of  $d\hat{\theta}/d\theta$ .  $H$  is found to be very close to zero when the vortex strength is below  $\mathcal{V}_p$ . For example, for  $\mathcal{V}=1.47^{s+}$ , the time-asymptotic value of  $H$  is  $8.4 \times 10^{-3}$ . Furthermore, it is found that 89% of this value<sup>20</sup> is due to interpolation errors in computing  $H$ . The remaining 11% is believed to be attributable to the asymmetric arrangement of the grid nodes, and not to the physical presence of asymmetric flow.

The time-asymptotic behavior past the primary limit point is three-dimensional and time-periodic. Values of  $H$  for time-asymptotic flows computed past the primary limit point are much greater than the near-zero value of  $H$  computed at  $\mathcal{V}=1.47^{s+}$ . For example,  $H=1.293 \times 10^{-1}$  for the time-asymptotic flow at  $\mathcal{V}=1.48$ . The time-periodic nature of the flow at is observed by plotting time histories of flow quantities at a fixed location in space. In particular,  $v_s$  and  $w_s$  are defined as the crossplane velocity components at a fixed centerline location of  $x=7$ . Plots of  $v_s$  and  $w_s$  are shown in Fig. 8(a), with the corresponding phase plot of  $v_s$  shown in Fig. 8(b) ( $\delta t=0.8$ ). The periodic nature of  $v_s$  is evident in the figure. The phase plot of  $w_s$  is not shown, owing to the similarity between  $v_s$  and  $w_s$ . The axial velocity component  $u_s$  is found to be steady.

Contours of the axial velocity component,  $u$ , are shown in Fig. 9 to illustrate the change in flow behavior. Contours of  $u$  are shown in Fig. 9(a) for  $\mathcal{V}=1.47^{s+}$ . One-half of the  $x-y$  plane is omitted due to flow symmetry about the  $x$  axis. The initial, steady axisymmetric flow is shown with dashed contour lines, while the time-asymptotic, steady solution of the TANS model is shown with solid contour lines. The agreement between the two solutions is excellent, demonstrating that the initial flow is stable to the small 3-D disturbances introduced in the numerical solution procedure. Fig. 9(b) shows the initial axisymmetric solution for  $\mathcal{V}=1.5$ , which is past the primary limit point. The strong bubble breakdown region is clearly evident from the negative region of  $u$  (dashed lines) between  $x=5$  and  $x=10$ . Time integration of this flowfield to  $t=400$  results in the 3-D flowfield depicted in Fig. 9(c). The bubble breakdown structure vanishes when 3-D flow is allowed, resulting in a solution with no reversed flow. The three-dimensional nature of the flow is found to be contained to the region aft of the tube constric-

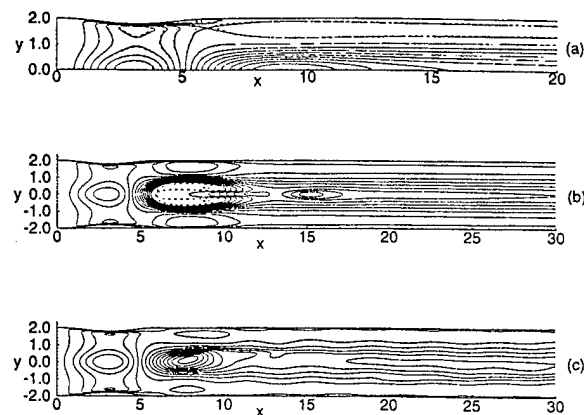


FIG. 9. Contours of the axial velocity component,  $u$ , in the  $x-y$  plane ( $z=0$ ) for  $Re=1000$  flows computed about  $\mathcal{V}_p=1.47435$  (numbers in parentheses indicate the range of 15 evenly-spaced contour values): (a)  $\mathcal{V}=1.47^{s+}$  (0.44, 1.4); initial axisymmetric solution (dashed), TANS time-asymptotic solution (solid), (b) initial axisymmetric solution at  $\mathcal{V}=1.5$  (-0.12, 1.4);  $u>0$  (solid),  $u<0$  (dashed), (c) 3-D TANS time-asymptotic solution for  $\mathcal{V}=1.5$  at  $t=400$  (0.1, 1.4).

tion, with steady and axisymmetric flow maintained upstream.

Snapshots of the time-asymptotic streaklines for  $\mathcal{V}=1.47^{s+}$  and  $\mathcal{V}=1.5$  are shown in Fig. 10; the tube geometry is omitted for clarity. The flows have a base rotation in the clockwise direction when viewed in the positive  $x$  direction. At  $\mathcal{V}=1.47^{s+}$  [Fig. 10(a)], before the Hopf point, the vortex core swells at an axial location of about  $x=6$ . The swelling of the core occurs symmetrically, and illustrates the effect of axial flow deceleration. At  $\mathcal{V}=1.5$  [Fig. 10(b)], beyond the Hopf point, a spiral asymmetric disturbance occurs upstream of the initial swelling at  $x=6$  for  $\mathcal{V}=1.47^{s+}$ . The upstream movement of flow disturbances with increasing  $\mathcal{V}$ , evident between Figs. 10(a) and 10(b), is in agreement with experimental evidence.<sup>1</sup> The axial deceleration along with a time-periodic rotation of the disturbance produces distorted rings of material points, which subsequently spiral and convect downstream. The direction of rotation is clockwise (looking downstream); consistent with the

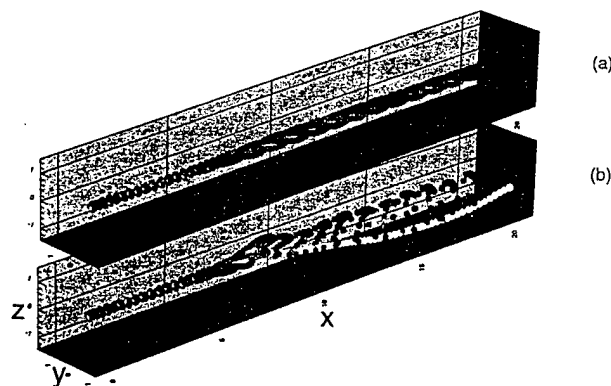


FIG. 10. Particle traces showing development of three-dimensionality beyond the primary limit point at  $\mathcal{V}_p=1.47435$ : (a)  $\mathcal{V}=1.47^{s+}$ , (b)  $\mathcal{V}=1.5$ .

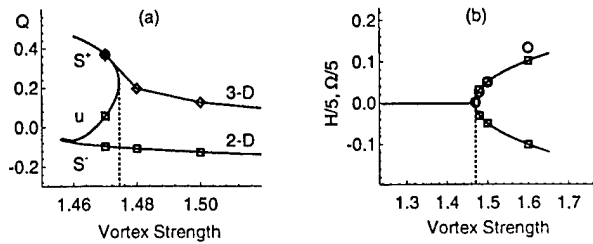


FIG. 11. Bifurcation diagram: (a) Initial and time-asymptotic values of  $Q$  showing emergence of 3-D solution branch (diamonds) from branch of axisymmetric solutions (squares). (b) magnitude of time-periodic disturbances,  $\Omega$ , (squares) and magnitude of flow asymmetries,  $H$  (circles).

base vortical flow. Solutions at higher vortex strengths reveal more coherent spiral disturbances, similar to previous results at  $Re=250$ .<sup>17</sup>

The loss of stability of steady flow to time-periodic flow as vortex strength is increased is evidence for a Hopf bifurcation. The nature of the bifurcation is summarized in Fig. 11. In Fig. 11(a), the initial and time-asymptotic values of  $Q$  are depicted. The initial conditions are denoted with square symbols while time-asymptotic values are time-averaged and denoted with diamond symbols. A distinct change in solution character occurs when  $\mathcal{V}$  is increased slightly from 1.47 to 1.48. All three time-asymptotic solutions at  $\mathcal{V}=1.47$  are steady and axisymmetric, while at  $\mathcal{V}=1.48$  the time-asymptotic flowfield is time-periodic and three-dimensional. In between the vortex strengths of 1.47 and 1.48 lies the primary limit point at  $\mathcal{V}_p=1.47435$ . Thus the maximum difference in  $\mathcal{V}$  between the location of the Hopf bifurcation and the primary limit point is  $5.65 \times 10^{-3}$ . The diamond symbols denote the emerging path of 3-D solutions which bifurcate from the branch of steady, axisymmetric solutions. The authors' interpretation of this result is that the mechanism for the existence of at least one family of 3-D solutions, which possess reversed flow at sufficiently large values of vortex strength, is the loss of stability of the axisymmetric base flows. Reversed flow is not observed along the 3-D solution branch until the vortex strength is increased from  $\mathcal{V}=1.5$  to  $\mathcal{V}=1.6$ . After the primary limit point,  $\mathcal{V}=1.48$ , the time-asymptotic value of  $Q$  (diamond symbol) is significantly larger than the initial value of  $Q$  (square symbol) for the same value of  $\mathcal{V}$ . This observation is consistent with previous results<sup>17</sup> where the increase in  $Q$  is correlated to the positive net production of both radial and azimuthal vorticity components as flow asymmetries emerge.

The nature of the Hopf bifurcation is further illustrated by plotting the parameters  $H$  and  $\Omega$  in Fig. 11(b).  $\Omega$  is defined as the maximum and minimum centerline values of the sum  $v+w$  found over a sufficiently long time interval in the time-asymptotic flow. Thus  $\Omega$  is zero for axisymmetric flow and nonzero for 3-D flow. The fact that  $\Omega$  steadily increases from zero near  $\mathcal{V}_p$  is evidence for the supercritical type of Hopf bifurcation.<sup>23</sup> Furthermore, it is evident that  $H$  sharply departs from zero for flows computed past the primary limit point. Values of  $H$ ,  $\Omega$  and  $Q$  for  $Re=1000$  are summarized in Table I.

The solid line in Fig. 11(b) is a quadratic polynomial fit

TABLE I. Summary of time-asymptotic parameter values for  $Re=1000$ .

$\mathcal{V}$	$Q$ (2-D)/(3-D)	$\Omega$	$H$
1.47 <sup>+</sup>	+0.369/+0.371	-0.0001/0.0001	0.0084
1.47 <sup>u</sup>	+0.056/+0.364	-0.0001/0.0002	0.0084
1.47 <sup>-</sup>	-0.098/+0.369	-0.0003/0.0004	0.0084
1.48	-0.110/+0.195	-0.1550/0.1550	0.1293
1.50	-0.128/+0.124	-0.2513/0.2513	0.2491
1.60	-0.159/-0.032	-0.5080/0.5080	0.6653

of  $\Omega$  for  $\mathcal{V}=1.48, 1.5$ , and  $1.6$ . The curve shows the quadratic nature of the data, and is useful in estimating the Hopf bifurcation point,  $\mathcal{V}_h$ . The computed curve is  $\mathcal{V}=0.5147\Omega^2-0.0013\Omega+1.468$ , which yields  $\mathcal{V}_h=1.468$ . This value is  $2 \times 10^{-3}$  lower in vortex strength than the  $\mathcal{V}=1.47$  case where steady flow was found. Thus the Hopf point identified through the curve fit is slightly lower in vortex strength than the bracket containing the Hopf point identified through time integration. The linear term in the polynomial is nearly zero, which implies that  $\Omega$  departs from zero at the bifurcation point with nearly infinite slope. This is in good agreement with Hopf bifurcation theory,<sup>23</sup> which dictates that the bifurcation parameter,  $\mathcal{V}$ , is symmetric with respect to a characteristic amplitude of the bifurcated flow, i.e.,  $\mathcal{V}(\Omega)=\mathcal{V}(-\Omega)$ . This symmetry condition holds when the linear term is identically zero.

The stability of 2-D flows computed with the noncolumar (zero azimuthal vorticity) inflow condition is briefly investigated for  $Re=1000$ . The primary limit point for this case is higher ( $\mathcal{V}_p=1.59048$ ) than the primary limit point for the columnar inflow condition ( $\mathcal{V}_p=1.47435$ ). It is also found that the region of nonuniqueness for this case has increased to 0.048, compared to 0.015 for the columnar initial conditions. Four time-integration runs are performed. Two runs are performed at  $\mathcal{V}=1.585^{+}$  and  $\mathcal{V}=1.585^{-}$ , which are below the primary limit point. The other two runs are at  $\mathcal{V}=1.595$  and  $\mathcal{V}=1.605$ , which are above the primary limit point. The temporal behavior of the two runs computed before the primary limit point is similar to the behavior observed for the columnar inflow conditions. That is, both flows time-asymptote to steady, axisymmetric conditions. Past the primary limit point, the  $\mathcal{V}=1.595$  case is also found to approach a steady, axisymmetric flow. It is noted, however, that much longer run times ( $t \approx 1000$ ) are required to approach time-asymptotic conditions for this case. At  $\mathcal{V}=1.605$ , the initial breakdown bubble transitions to a 3-D, time-periodic flow with no breakdown, analogous to the results for the columnar inflow condition. Thus the results indicate that changing inflow conditions delays the instability to 3-D disturbances to a point slightly past the primary limit point. The difference in vortex strength between the primary limit point and the  $\mathcal{V}=1.605$  case is  $1.452 \times 10^{-2}$ . Vortex strengths between these two cases were not investigated.

As previously discussed in Section I, the location of the primary limit point in an axisymmetric solution space has been associated with the appearance of critical flow. The results of this study may add further insight into the role of the primary limit point. The results show that the Hopf and

primary limit point locations differ by a maximum of  $5.65 \times 10^{-3}$  in  $\mathcal{V}$ . Also, for the case of noncolumnar inflow conditions, the Hopf point and the primary limit point locations differ by a maximum of  $1.452 \times 10^{-2}$ . Thus, the results imply a possible connection between the loss of stability to 3-D disturbances, the location of the primary limit point, and the appearance of critical flow.

The results of this work do not imply that the Hopf bifurcation and the location of the primary limit point are exactly coincident. The vortex strengths chosen here are not sufficiently close to the limit point to make this determination. Also, subtle differences between the PAC and TANS models, such as the introduction of artificial damping, are unavoidable. This makes it very difficult to precisely predict the onset of the instability. Furthermore, time-integration proves to be quite demanding on computational resources when computing solutions near the Hopf bifurcation. This is primarily due to the lengthy times required for the instability to develop, with this time increasing dramatically the closer one computes to the actual Hopf point. Instead, a contribution of this work is that a Hopf bifurcation point is bracketed to lie in close proximity to the primary limit point—a contribution previously unreported in the literature. It is anticipated that a more direct means of computing the Hopf point is in order for determining if there exists a definite correspondence between the flow instability and the primary limit point. Such solvers have recently been developed for 2-D flows.<sup>24</sup>

#### IV. SUMMARY AND DISCUSSION

Axisymmetric solutions computed in this study at  $Re=1000$  contain a region of nonuniqueness, resulting in primary and secondary limit points. These axisymmetric solutions are treated as initial conditions to a 3-D time-integration algorithm. When the vortex strength is prescribed to be less than that at the primary limit point, the resulting time-asymptotic solutions are found to be steady and axisymmetric. In particular, when three nonunique initial conditions are time-integrated, all three initial conditions time-asymptote to the solution corresponding to the initial condition of the upper stable branch. The transition between the initial bubble breakdown solution of the lower stable branch to the nearly columnar upper stable branch solution is investigated. It is found that the bubble breakdown flow transforms temporarily to a 3-D spiral form, which ultimately decays to nearly columnar flow. When the vortex strength is prescribed to be greater than the primary limit point, the resulting time-asymptotic solutions are found to be time-periodic and three-dimensional. Thus a Hopf bifurcation is found to occur in very close proximity to the primary limit point. Modifying the inflow boundary condition to relax the columnar flow assumption results in the Hopf point lying at a vortex strength that is slightly greater than the primary limit point.

Previous results<sup>17</sup> by the authors for  $Re=250$  also show evidence for the Hopf bifurcation, which occurs in this case near  $\mathcal{V}=1.53$ . However, only unique axisymmetric solutions exist at this lower Reynolds number. The lack of limit points

preclude any obvious correlation between the loss of stability and the character of the axisymmetric solution branch. Two other similarities in the solution behavior are noted at the two Reynolds numbers. First, as  $\mathcal{V}$  is increased, the loss of stability occurs before reversed flow is present. Second, for vortex strengths near the instability, the time-asymptotic values of  $Q$  for 3-D flows are higher than for the initial 2-D flow.

The role of the primary limit point is further defined in this study. Previous (axisymmetric) work had established a correspondence between the primary limit point and a change in flow criticality, implying that flow criticality signals the emergence of axisymmetric breakdown. This study indicates that the primary limit point is in close proximity to the vortex strength where stability to 3-D disturbances is lost, with further increases in vortex strength ultimately resulting in vortex breakdown. This result may allow the distinct, time-periodic fluctuations associated with the Hopf bifurcation to be used to signal the onset of breakdown. However, a precise statement concerning the connection between the Hopf bifurcation and the primary limit point is not established in this work. This is due to the practical limits of bracketing a bifurcation point through time integration, and possibly due to subtle differences in which artificial damping is employed within the two numerical models.

Finally, it is of interest to contrast the role of the primary limit point for 3-D flows to the role associated with axisymmetric solutions. For axisymmetric flows, the primary limit point is associated with values of  $Q$  which are positive. However, a slight increase in  $\mathcal{V}$  above the primary limit point brings about large differences in solution behavior, due to the sudden drop of solutions from the upper to lower stable branch. Thus, a slight increase in  $\mathcal{V}$  from  $\mathcal{V}_p$  in 2-D flows results in a dramatic change in solution character—from flows with no reversed flow to flows with reversed flow. Results in this study indicate that 3-D flows do not undergo this large change in flow structure as the primary limit point is crossed. Instead, flows computed just past the primary limit point are void of reversed flow. In 3-D flows, therefore, the primary limit point is not associated with breakdown, as it is generally perceived in axisymmetric flows. For example, Fig. 11(a) shows that the primary limit point is at  $\mathcal{V}_p=1.47435$ , whereas reversed flow is not achieved until approximately  $\mathcal{V}=1.6$ . In general, the effect of three-dimensionality is the delay of the formation of reversed flow, requiring generally larger values of vortex strength to achieve breakdown than in axisymmetric flows.

Further work is needed to establish a precise relationship between the Hopf bifurcation and the primary limit point. In particular, a theoretical study of 2-D and 3-D vortical flows in tubes would help confirm and may better define the numerically determined relationship found in this work. In addition, more studies are needed to determine the effects of inlet flow profiles and tube geometry on the dynamic and time-asymptotic behavior.

## ACKNOWLEDGMENTS

This work was sponsored by the Air Force Office of Scientific Research and Wright Laboratory. Computational resources were provided by a grant of HPC time from the DoD HPC Center, Bay St. Louis, MS.

## APPENDIX: SOLUTION PROCEDURE

The solution procedure is a Beam-Warming,<sup>25</sup> approximate factorization scheme. The equations are solved in a nonconservative, implicit manner using three-point-backward time integration. Temporal accuracy is second order for the inviscid terms and first order for the viscous terms, owing to the explicit treatment of the viscous terms. A fourth-order spatially accurate compact,<sup>26</sup> or Padé, operator is employed to approximate derivatives. The compact approximation for the derivative of a scalar,  $u$ , with respect to  $x$ , for example, is given by

$$u_x = \frac{1}{2\Delta x} \left( \frac{\delta_x u}{\mathcal{S}_x} \right) + \mathcal{O}(\Delta x)^4,$$

where

$$\delta_x u \equiv u_{i+1} - u_{i-1}, \quad \mathcal{S}_x \equiv 1 + (u_{i+1} - 2u_i + u_{i-1})/6.$$

$\mathcal{S}$  denotes a general operator while the subscript refers to the coordinate direction.

The general, approximately factored scheme in delta form, where  $\Delta^n U \equiv U^{n+1} - U^n$  is given by

$$\mathcal{X}\mathcal{Y}\mathcal{Z}\Delta^n U = \mathcal{R}, \quad (\text{A1})$$

where

$$\mathcal{X} = [I + (\Delta t/3)\mathcal{A}^{n+1}(\delta_\xi/\mathcal{S}_\xi) - \omega_i \delta_\xi^2],$$

$$\mathcal{Y} = [I + (\Delta t/3)\mathcal{B}^{n+1}(\delta_\eta/\mathcal{S}_\eta) - \omega_i \delta_\eta^2],$$

$$\mathcal{Z} = [I + (\Delta t/3)\mathcal{C}^{n+1}(\delta_\zeta/\mathcal{S}_\zeta) - \omega_i \delta_\zeta^2],$$

$$\mathcal{R} = t1 + t2 - t3\Delta t/3,$$

$$t1 = (2/3)(\Delta t D^n + 0.5\Delta^{n-1}U),$$

$$t2 = -\omega_e \Delta t (\delta_\xi^4/\mathcal{S}_\xi^4 + \delta_\eta^4/\mathcal{S}_\eta^4 + \delta_\zeta^4/\mathcal{S}_\zeta^4)U^n,$$

$$t3 = \left( \mathcal{A}^{n+1} \left( \frac{\delta_\xi}{\mathcal{S}_\xi} \right) + \mathcal{B}^{n+1} \left( \frac{\delta_\eta}{\mathcal{S}_\eta} \right) + \mathcal{C}^{n+1} \left( \frac{\delta_\zeta}{\mathcal{S}_\zeta} \right) \right) U^n.$$

The  $\mathcal{A}$ ,  $\mathcal{B}$ , and  $\mathcal{C}$  matrices at the unknown time level,  $n+1$ , are obtained through extrapolation. This is required for the nonconservative scheme to achieve second-order temporal accuracy. To insure steady-state consistency,<sup>27</sup> the explicit damping coefficient,  $\omega_e$ , is defined above such that the explicit damping term is multiplied by  $\Delta t$ . The implicit damping coefficient,  $\omega_i$ , is set to zero for this work.

The solution is updated following  $\xi$ ,  $\eta$ , and  $\zeta$  sweeps:

$$[\mathcal{S}_\xi I + (\Delta t/3)\mathcal{A}^{n+1}\delta_\xi]\Delta^n U_1 = \mathcal{S}_\xi(t1 + t3) + t2,$$

$$[\mathcal{S}_\eta I + (\Delta t/3)\mathcal{B}^{n+1}\delta_\eta]\Delta^n U_2 = \mathcal{S}_\eta(\Delta^n U_1),$$

$$[\mathcal{S}_\zeta I + (\Delta t/3)\mathcal{C}^{n+1}\delta_\zeta]\Delta^n U = \mathcal{S}_\zeta(\Delta^n U_2).$$

$$U^{n+1} = U^n + \Delta^n U.$$

$\mathcal{S}_\xi$  is multiplied through Eq. (A1) before solving the  $\xi$  sweep, and acts on all of the right-hand side terms except the damping term,  $t2$ . The damping term is excluded for consistency in comparing results to the central-difference PAC scheme. The traditional method of sweeping in the  $\eta$  and  $\zeta$  directions is modified<sup>20</sup> to allow for the presence of a multi-block grid structure. Spatial derivatives in  $t3$ , grid metrics, and viscous terms,  $D$ , are computed implicitly at time-level  $n$  to fourth-order accuracy. This is accomplished in an efficient manner using a lower/upper decomposition technique, since the resulting set of equations represent a constant, tridiagonal matrix-inversion problem. At boundaries  $s1$ ,  $s2$  and  $s3$ , second-order accurate, three-point forward/backward differences are used. Derivative terms normal to the grid cuts are approximated with fourth-order central differences.

The numerical procedure was partially checked by solving for a uniform freestream with Dirichlet (no correction) boundary conditions at  $s1$ ,  $s2$  and  $s3$ . The resulting temporal corrections,  $\Delta^n U$ , were found to be machine zero everywhere for 100 iterations over a wide range of time steps. It is of interest to note that employing a fourth-order accurate boundary stencil<sup>26</sup> along the physical boundaries  $s1$ ,  $s2$  and  $s3$  of the form

$$u_{\xi,1} + 3u_{\xi,2} = (1/6)(-17u_1 + 9(u_2 + u_3) - u_4)$$

resulted in freestream conservation errors.

Validation of the TANS model<sup>20</sup> proceeded along two lines. First, a variety of model problems were solved, including the incompressible and compressible flows over a flat plate, unsteady Couette flow and unsteady heat conduction. The model output and the known solutions matched to a high degree of accuracy in each case. Second, the TANS and PAC models were cross-validated by comparing computed solutions obtained under flow conditions which lead to steady and axisymmetric flow. The resulting solutions were found to agree to a high degree of accuracy.

<sup>1</sup>J. H. Faler and S. Leibovich, "Disrupted states of vortex flow and vortex breakdown," *Phys. Fluids* **20**, 1385 (1977).

<sup>2</sup>J. D. Buntine and P. G. Saffman, "Inviscid swirling flows and vortex breakdown," *Proc. R. Soc. London Ser. A* **449**, 139 (1995).

<sup>3</sup>S. Wang and Z. Rusak, "On the stability of an axisymmetric rotating flow in a pipe," *Phys. Fluids* **8**, 1007 (1996).

<sup>4</sup>S. Wang and Z. Rusak, "On the stability of non-columnar swirling flows," *Phys. Fluids* **8**, 1017 (1996).

<sup>5</sup>J. M. Lopez, "On the bifurcation structure of axisymmetric vortex breakdown in a constricted pipe," *Phys. Fluids* **6**, 3683 (1994).

<sup>6</sup>D. L. Darmofal and E. M. Murman, "On the trapped wave nature of axisymmetric vortex breakdown," *AIAA Paper No. 94-2318*, 1994.

<sup>7</sup>P. S. Beran and F. E. C. Culick, "The role of non-uniqueness in the development of vortex breakdown in tubes," *J. Fluid Mech.* **242**, 491 (1992).

<sup>8</sup>M. Breuer and D. Hänel, "Solution of the 3-D incompressible Navier-Stokes equations for the simulation of vortex breakdown," *8th GAMM Conference*, Delft, Netherlands, 1989.

<sup>9</sup>R. E. Spall, T. B. Gatski, and R. L. Ash, "The structure and dynamics of bubble-type vortex breakdown," *Proc. R. Soc. London Ser. A* **429**, 613 (1990).

<sup>10</sup>R. E. Spall and T. B. Gatski, "A computational study of the topology of vortex breakdown," *Proc. R. Soc. London Ser. A* **435**, 321 (1991).

<sup>11</sup>M. R. Visbal, "Computed unsteady structure of spiral vortex breakdown on delta wings," *AIAA Paper No. 96-2074*, 1996.

<sup>12</sup>S. Táasan, "Multigrid method for a vortex breakdown simulation," *NASA CR-178106*, 1986.

- <sup>13</sup>S. Leibovich and A. Kribus, "Large-amplitude wavetrains and solitary waves in vortices," *J. Fluid Mech.* **216**, 459 (1990).
- <sup>14</sup>P. S. Beran, "The time-asymptotic behavior of vortex breakdown in tubes," *Comput. Fluids* **23**, 913 (1994).
- <sup>15</sup>Z. Rusak and S. Wang, "Review of theoretical approaches to the vortex breakdown phenomenon," AIAA Paper No. 96-2126, 1996.
- <sup>16</sup>T. Sarpkaya, "On stationary and traveling vortex breakdowns," *J. Fluid Mech.* **45**, 545 (1971).
- <sup>17</sup>J. C. Tromp and P. S. Beran, "Temporal evolution of three-dimensional vortex breakdown from steady, axisymmetric solutions," *AIAA J.* **34**, 632 (1996).
- <sup>18</sup>T. B. Benjamin, "Theory of the vortex breakdown phenomenon," *J. Fluid Mech.* **14**, 593 (1962).
- <sup>19</sup>M. G. Hall, in *Annual Review of Fluid Mechanics* (Annual Review, Palo Alto, 1972), Vol. 4, p. 195.
- <sup>20</sup>J. C. Tromp, "The dependence of the time-asymptotic structure of 3-D vortex breakdown on boundary and initial conditions," Ph.D. thesis, Air Force Institute of Technology (1995).
- <sup>21</sup>J. P. Steinbrenner, J. R. Chawner, and C. L. Fouts, "The GRIDGEN 3D multiple block grid generation system," 1 (WRDC, Wright-Patterson AFB, OH, 1990), TR-90-3022.
- <sup>22</sup>Z. Rusak, S. Wang, and C. Whiting, "Numerical computations of axisymmetric vortex breakdown in a pipe," AIAA Paper No. 96-0801, 1996.
- <sup>23</sup>G. Iooss and D. D. Joseph, *Elementary Stability and Bifurcation Theory*, 2nd ed. (Springer-Verlag, New York, 1990).
- <sup>24</sup>S. A. Morton and P. S. Beran, "Hopf-bifurcation analysis of airfoil flutter at transonic speeds," AIAA Paper No. 96-0060, 1996.
- <sup>25</sup>R. M. Beam and R. F. Warming, "An implicit finite-difference algorithm for hyperbolic systems in conservation-law form," *J. Comput. Phys.* **22**, 87 (1976).
- <sup>26</sup>S. K. Lele, "Compact finite difference schemes with spectral-like resolution," *J. Comput. Phys.* **103**, 16 (1992).
- <sup>27</sup>J. Désidéri, J. L. Steger, and J. C. Tannehill, "On improving the iterative convergence properties of an implicit approximate-factorization finite difference algorithm," NASA TM 78495, 1978.

# **Critical-State Transients for a Rolling 65-Degree Delta Wing**

D. S. Grismer and J. E. Jenkins

Reprinted from

## **Journal of Aircraft**

Volume 34, Number 3, Pages 380-386



*A publication of the*  
American Institute of Aeronautics and Astronautics, Inc.  
1801 Alexander Bell Drive, Suite 500  
Reston, VA 20191-4344

# Critical-State Transients for a Rolling 65-Degree Delta Wing

Deborah S. Grismer\* and Jerry E. Jenkins†

U.S. Air Force Wright Laboratory, Wright-Patterson Air Force Base, Ohio 45433-7521

Force and moment experiments were conducted for a 65-deg delta wing undergoing ramp-and-hold and harmonic rolling motions. This extensive set of experiments isolated critical-state responses. Motions between critical states and motions crossing critical states were included. Roll-angle amplitude and the roll rate were varied. The total angle of attack and Mach number were held constant at 30 deg and 0.3, respectively. The amount of time required for the rolling moment coefficient to reach its steady-state value after the end of a ramp was quantified for numerous ramp motions. This relaxation time was a significantly large value for many of the motions, especially when the 5-deg critical state was crossed. Motion history effects were determined for motions that crossed critical states. The effect of roll rate on critical-state transients proved to be insignificant.

## Nomenclature

$b$	= trailing-edge wing span
$C_l$	= rolling moment/ $qSb$
$C_{l_{dyn}}$	= $C_l - C_{l_{static}}$
$c$	= root chord
$\bar{c}$	= mean aerodynamic chord
$k$	= reduced frequency, $\omega b/2U_\infty$
$q$	= freestream dynamic pressure
$S$	= model planform area
$t$	= time
$t^*$	= nondimensional time, $2U_\infty t/b$
$U_\infty$	= freestream velocity
$\sigma$	= total angle of attack, body-axis inclination with respect to $U_\infty$
$\phi$	= body-axis roll angle $\cong \phi_1$
$\dot{\phi}$	= first derivative of $\phi$ with respect to time
$\ddot{\phi}$	= second derivative of $\phi$ with respect to time
$\phi_{ND}$	= nondimensional roll rate, $\dot{\phi}(b/2U_\infty)$
$\phi_1$	= shaft rotation angle at the base of the sting
$\phi_2$	= shaft rotation angle at the center of the force balance
$\omega$	= circular frequency, rad/s

## Introduction

**A**N expansion of the flight envelope has been and remains a very important goal for designers of high-performance air vehicles. Such high-performance aircraft are required to fly faster and at higher angles of attack. Because of these demands they often employ highly swept wing surfaces. When flying at higher angles of attack, controllability has become a large problem for these aircraft. Intense changes in the flowfield are encountered that result in dramatic nonlinearities in an aircraft's aerodynamic behavior. Under these conditions the aerodynamics are time- and motion-history-dependent; therefore, conventional quasisteady modeling techniques are not adequate.

This paper will discuss some implications of experimental force and moment results for a 65-deg delta wing driven

through roll maneuvers. This delta wing has been the focus of an in-depth study over the past several years.<sup>1-11</sup> Previous analyses of the delta wing have shown severe nonlinear aerodynamic behavior and the aerodynamics have been shown to be dependent on the precise motion history. As with other highly swept planforms, vortex breakdown was found to be a large contributor to the aerodynamic behavior of the 65-deg delta wing. The axial progression of breakdown because of a time-dependent variation in wing orientation was found to be quite slow.

The dynamic force and moment responses possessed large time lags. Two possible causes for these time lags are 1) finite response times caused primarily by the response of vortex breakdown and 2) transients resulting from one or more critical-state encounters. A critical state exists when a discontinuity in a static force or moment curve (or its derivative) occurs and its crossing causes a discrete change in the equilibrium response. Thus, time lags can result without encountering a critical state, but if a critical state is encountered, there is an additional amount of time that is required for the transition from one flow state to another. The time scales for these critical-state transients had not been established. For modeling purposes and possible simplifications, it would be very useful to know if the effects from one or more critical-state encounters can be neglected.

The force and moment experiments of this study were designed to isolate the effects induced by critical-state encounters. Measurements were obtained for ramp-and-hold motions and harmonic motions in roll. Comprehensive static and dynamic force and moment measurements were obtained. An examination of these results will be the focus of this paper, with the goal being to increase the knowledge of how to better model the transients induced from critical-state encounters.

## Discussion

### Experimental Equipment

The model used for the experiments was a 65-deg delta wing with sharp leading and trailing edges. A schematic of the model is shown in Fig. 1. Both the leading and trailing edges were symmetrically beveled with an included angle normal to the leading edge of 20 deg. The wing was constructed with a multilayer graphite composite skin and a foam core, and the fuselage was constructed purely of graphite composite. The wing thickness-to-root-chord ratio is 1.53%.

The delta wing was mounted in the Subsonic Aerodynamic Research Laboratory (SARL) 7 ft  $\times$  10 ft (2.1 m  $\times$  3.0 m)

Presented as Paper 96-2432 at the AIAA 14th Applied Aerodynamics Conference, New Orleans, LA, June 17-20, 1996; received Aug. 24, 1996; revision received Feb. 12, 1997; accepted for publication Feb. 17, 1997. This paper is declared a work of the U.S. Government and is not subject to copyright protection in the United States.

\*Captain, U.S. Air Force, Flight Control Division, Flight Dynamics Directorate, WL/FIGC, Building 146, 2210 Eighth Street, Suite 11. Member AIAA.

†Aerospace Engineer, Flight Control Division, Flight Dynamics Directorate, WL/FIGC, Building 146, 2210 Eighth Street, Suite 11. Senior Member AIAA.



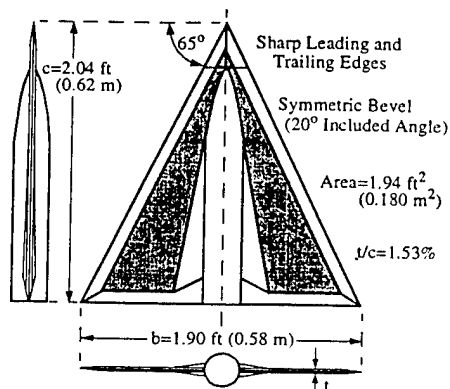


Fig. 1 Delta wing model.

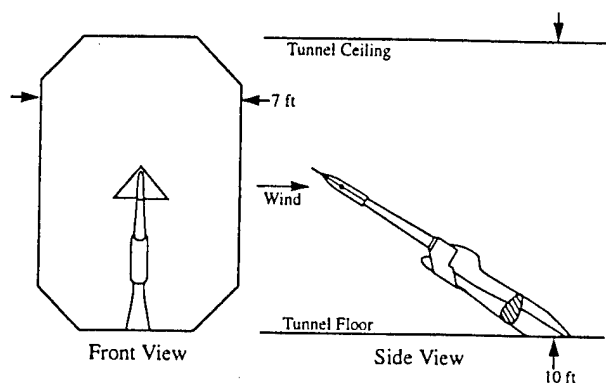


Fig. 2 Roll rig apparatus in SARL wind tunnel.

wind tunnel via a roll rig. The wing was mounted on a five-component strain gauge balance that was supported, by a drive shaft, through a hollow sting. The dynamic roll rig, installed in the SARL tunnel, is shown in Fig. 2. The apparatus, developed by the Canadian National Aeronautical Establishment (NAE), was designed for large-amplitude and high-rate motions. A more detailed description of both the model and roll rig design can be found in Ref. 12.

#### Data Acquisition and Reduction

The data presented here were obtained from a series of experiments designed and conducted both by personnel from Wright Laboratory and members of the Canadian Institute for Aerospace Research (IAR) in 1994. The delta wing was driven through both ramp-and-hold maneuvers and harmonic oscillations in roll. During these experiments, digitally sampled time histories of both the model motion and five-component force and moment responses were obtained.

For all roll motions presented here the total angle of attack  $\alpha$  was fixed at 30 deg and the Mach number was 0.3. Data were acquired with a constant sampling interval for a given motion and for several (usually 20) cycles of the motion. Five-component force and moment data were ensemble-averaged to yield 1024 data points for one cycle. The five components produced were normal force, pitching moment, side force, yawing moment, and rolling moment. The shaft rotation angle at the base of the sting was also measured throughout the same sampling time. For each motion data were acquired both with the tunnel operating at the desired testing speed and with the wind off.

#### Ramp Motions

The constant ramp roll rate was varied from 0.25 rad/s (14 deg/s) through 7 rad/s (400 deg/s) for the various ramp motions. A ramp-up cycle consists of a hold at  $\phi_{\min}$ , the ramp-up, a 0.5-s hold at  $\phi_{\max}$ , and a return to  $\phi_{\min}$ . The data, however, were acquired only for a small amount of time before

the ramp up starts, through the ramp up, and for the 0.5-s hold at  $\phi_{\max}$  after the end of the ramp. The part of the cycle spent returning to  $\phi_{\min}$  and an amount of time at  $\phi_{\min}$  before starting the next cycle are not included in the data acquisition sampling period. Data were acquired over a sufficient number of cycles so that the ensemble-averaged data did not change with the acquisition of data over an additional cycle.

The first step taken in the data reduction process was to convert the raw output voltages from the force balance to non-dimensional force and moment coefficients, based on the model geometry. The remaining part of the data reduction was much more involved. For many applications, a simple subtraction of the wind-off tare data from the wind-on data would be an adequate method of removing the inertial effects. However, for the ramp motions at which high angular accelerations were commanded at the beginning and end of the ramp, it was determined that such a subtraction was not appropriate.

For a given ramp-and-hold motion, the difference in the roll angle between the wind-on and wind-off data was very small. Slight differences between the measured and commanded roll angles, however, resulted in severely different accelerations commanded by the servo-system. Because of this, significant oscillations were present in both the wind-on and wind-off rolling moment coefficients, particularly following the commanded accelerations. The oscillations between the wind-on and wind-off runs were not always in-phase because the small roll-angle errors are influenced by the airloads acting on the model. Therefore, a subtraction of the two rolling-moment time histories often increased the amplitude of the oscillations.

The inertial effects were determined by an alternate method and they were subtracted from the wind-on force and moment coefficients, yielding a more accurate result, with significantly smaller oscillations. Knowing the roll angle, the rolling moment contribution caused just by the inertia can be calculated and subtracted from the wind-on rolling moment resulting from both the inertial and aerodynamic effects.

To determine the inertial effects the roll motion history  $\phi_i(t)$  from the tare runs was used to calculate  $\ddot{\phi}_i(t)$ .  $\ddot{\phi}_i(t)$  was calculated by taking a second-order central difference in time. The initial and final values of  $\phi_i(t)$  were calculated using a second-order one-sided difference. Because of the noise produced from differentiating twice, frequencies in the roll acceleration time histories above 100 Hz were numerically filtered out. Knowing  $\ddot{\phi}_i(t)$  and  $C_l(t)$  for a tare run, an estimate of the inertia  $I$  could be determined assuming a simple one-degree-of-freedom system in roll where

$$C_l(t) = (I/qSb)\ddot{\phi}_i(t) + K \quad (1)$$

$K$  is the value of  $C_l$  before and after the ramp when  $\ddot{\phi}_i(t) = 0$ . This value was near zero, but is included to account for any small biases in the signal. Using a least-squares linear curve fit, values of both  $I$  and  $K$  were calculated, since  $q$  from the wind-on tests  $S$  and  $b$  are all known. Also, the correlation coefficient could be calculated to assess the validity of the linear correlation assumption. Correlation coefficients from 0.60 to 0.85 were obtained. Plots of  $C_l$  vs  $\phi_i$  showed noticeable loops around the linear curve fit. Since the rotation angle was sensed at the end of the actuator shaft, it was desired to try to determine the shaft rotation angle at the same location where the rolling moment was measured, at the balance center. It was thought that a difference in the rotation angle between the base of the shaft and the balance center, because of torsional deflections of the drive shaft, might be the cause of the observed loops.

To determine the shaft rotation angle at the balance center  $\phi_2$  the entire shaft from its base to the center of the balance was modeled as a cylinder of uniform torsional stiffness. This system was modeled as a second-order system in terms of the difference in shaft rotation angle  $\Delta\phi$ , where  $\Delta\phi = \phi_2 - \phi_1$ .

Therefore, the system was described by the following equation:

$$\Delta \ddot{\phi}(t) + 2\zeta\omega_n \Delta \dot{\phi}(t) + \omega_n^2 \Delta \phi(t) = 0 \quad (2)$$

$\zeta$  and  $\omega_n$  are the damping ratio and natural frequency of the drive shaft torsional degree of freedom, respectively.  $\Delta \phi(t)$  was calculated using the indicial form of the Duhamel integral:

$$\Delta \phi(t) = \phi_2(t) - \phi_1(t) = A(t)\phi_1(0) + \int_0^t A(t-\tau)\dot{\phi}(\tau) d\tau \quad (3)$$

where  $A(t) = -e^{-\zeta\omega_n t}[\cos \omega_n t + (n/\omega)\sin \omega_n t]$  with  $n = -\zeta\omega_n$ , and  $\omega = \omega_n\sqrt{1 - \zeta^2}$ . Since  $\phi_1(t)$  was known,  $\phi_2(t)$  was then determined.  $\phi_1(t)$  was found to be essentially identical to  $\phi_2(t)$ .

Fixed values of  $\zeta$  and  $\omega_n$  were found by trying to minimize the difference between the measured  $C_l(t)$  and the  $C_l(t)$  calculated using  $\phi_2(t)$  in Eq. (1). Previous work<sup>11</sup> had shown, however, that the damping force was not proportional to  $\dot{\phi}$ , but rather it was essentially a constant force opposing the direction of motion. Therefore,  $\zeta$  was set to be inversely related to  $|\dot{\phi}|$  to provide a constant damping force. This provided a good match between the measured and calculated values of  $C_l(t)$  as desired.

Using the values of  $l/qSb$  and  $K$  determined by including the tare values of  $\phi_2(t)$  in Eq. (1), the necessary information was found to subtract the inertial effects from the wind-on rolling moment data. For ramp motions, the values of  $C_l(t)$  discussed in the remainder of this paper were calculated by taking the wind-on measured values of  $C_l(t)$  and subtracting  $C_l(t)$  calculated from Eq. (1), using the wind-on measured values for  $\phi_1(t)$ .

#### Harmonic Motions

The frequency was varied from 1.1 through 11 Hz for the harmonic motions. For these motions one sampling cycle is one complete harmonic oscillation. In these cases, force and moment data were obtained by subtracting the wind-off data from the wind-on data. Obvious oscillations were present in the resulting force and moment time histories. To better smooth the data, a fast Fourier transform was performed and a limited number of harmonics were kept. The number of harmonics retained varied with forcing frequency as shown in Table 1. Determining the number of harmonics to retain was established by choosing a number small enough to provide sufficient smoothing while retaining the overall shape of the time histories.

#### Observations

Previous findings<sup>1</sup> revealed the existence of a critical state for this delta wing at approximately  $\phi = 5$  deg. This can be seen in the static rolling moment coefficient vs  $\phi$ , shown in Fig. 3. In the region of  $\phi = 5$  deg a definite discontinuity in the rolling moment coefficient is observed. A discontinuity in

the pitching moment coefficient was also observed around this angle. These discontinuities indicate the existence of a subcritical bifurcation. Critical states around 8 and 11.3 deg were also proposed in previous work. The 8-deg critical state is likely to be a Hopf bifurcation because of the large rms fluctuations.<sup>2</sup> The increase in scatter for  $\sim 8 \text{ deg} < \phi < \sim 12 \text{ deg}$ , shown in Fig. 3, indicates that time-averaging failed to average out low-frequency fluctuations. The 11.3-deg critical state appears to be a supercritical bifurcation. Also, the unsteadiness in  $C_l$  is greatly reduced for  $\phi > \sim 12$  deg.

#### Ramp Motions

The experiments were designed to isolate the effects of critical-state encounters from viscous time lags caused primarily by the slow response of vortex breakdown position. Four different ramp motions are shown in Fig. 4. These ramp motions either stay below the critical state around  $\phi = 5$  deg, cross the critical state, or stay above the critical state.

Figure 5 illustrates  $C_l(t)$  for a ramp motion in roll from 7 to 4 deg at  $-1 \text{ rad/s}$  as compared to the quasisteady  $C_l(t)$  over this range in roll angle. This figure reveals an obvious difference between the measured and quasisteady response. Also, it is interesting that at ramp onset the dynamic response is increasing, while the reverse is true of the quasisteady behavior. Note that  $C_l(t)$  does not approach the quasisteady value until long after the ramp has ended. The amount of time required for the rolling moment coefficient after the end of a ramp ( $\dot{\phi} \approx 0$ ) to reach its quasisteady value was quantified for many motions.

It was desired to isolate the transient effects resulting from the presence of the leading-edge vortices. Previous findings<sup>13</sup>

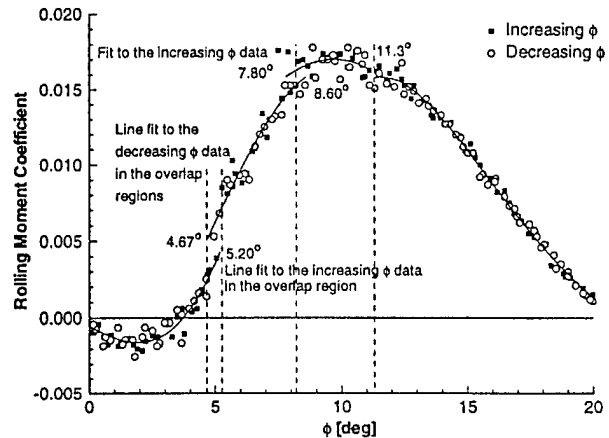


Fig. 3 Time-averaged static  $C_l$  for both increasing and decreasing  $\phi$ .

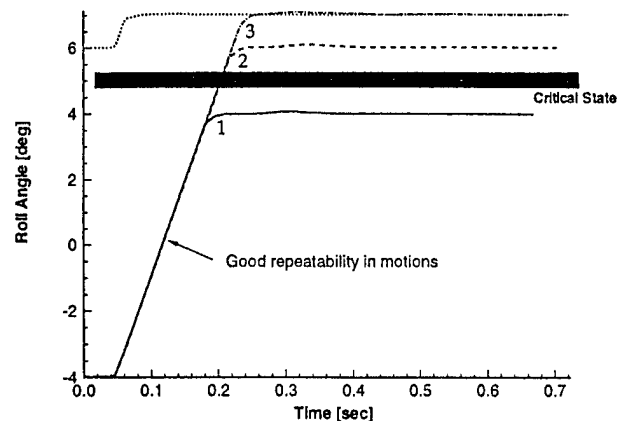


Fig. 4 Sample (1 rad/s) ramp motions about the 5-deg critical state.

Table 1 Number of harmonics retained for harmonic motions of varying forcing frequency

Forcing frequency, Hz	Reduced frequency	Number of harmonics kept	Resulting cutoff frequency, Hz
1.1	0.010	8	8.8
2.2	0.021	8	17.6
3.3	0.031	7	23.1
4.4	0.042	6	26.4
5.5	0.052	5	27.5
7.7	0.073	4	30.8
8.8	0.084	4	35.2
11	0.105	3	33.0

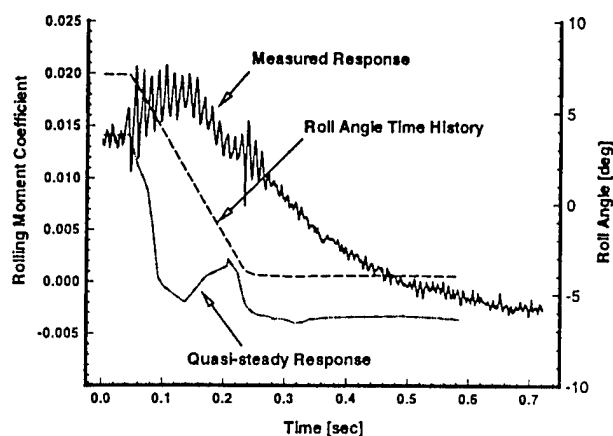


Fig. 5 Static and dynamic  $C_l$  for a  $(-1 \text{ rad/s})$  ramp through the 5-deg critical state.

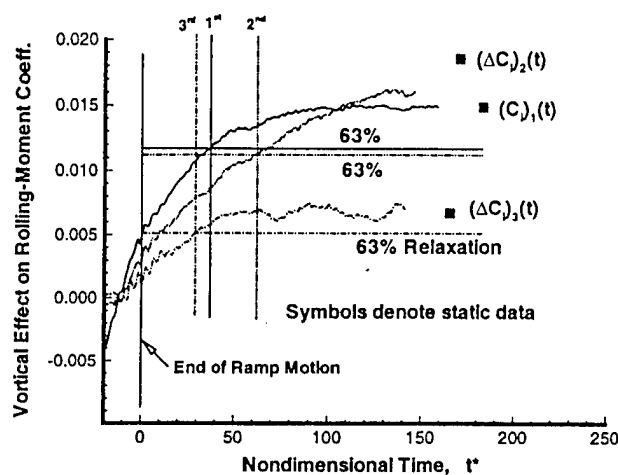


Fig. 6 Determination of relaxation times for ramp motions through the 5-deg critical state ( $\phi_{ND} = 0.003$ ).

revealed that the vortical component of the rolling moment had a net destabilizing effect for roll-angle variations. The presence of vortex breakdown and its relatively slow response is considered to be the dominant cause of time lags observed for dynamic maneuvers (not counting critical-state effects). The potential flow component of the rolling moment reacts at the freestream convection speed, which for these rates can be considered virtually instantaneous. Therefore, the potential flow part of the rolling moment coefficient was subtracted from the total rolling moment coefficient. The potential contribution was calculated using QUADPAN, a panel code developed by Lockheed-California Company.<sup>14</sup>

Figure 6 shows the vortical contribution to the rolling moment coefficient, the total rolling moment minus the potential contribution. This figure illustrates how relaxation times were calculated. The first, second, and third rolling moment coefficients correspond to ramp motions from  $-4$  deg to  $4$ ,  $6$ , and  $7$  deg, respectively, each for a roll rate of  $1 \text{ rad/s}$ , as shown in Fig. 4. For each of these three ramp motions the vortical rolling moment responses were time-shifted so that a nondimensional time of  $0.0$  corresponded to the end of each of the ramp motions. Also, the second vortical rolling moment coefficient  $(\Delta C_l)_2$ , shown in Fig. 6, has the response of the first motion subtracted. Likewise, the third response had the response from the second motion subtracted.

The relaxation times that were quantified, as shown in Fig. 6, were actually the time after the end of the ramp until the rolling moment coefficient reached 63% of its value at the end

of the ramp-and-hold. This value of 63% was chosen because, for an exponential decaying function  $C_l(t)$ , where  $\Delta C_l(t) = C_{l_{static}}[1 - e^{-(t/a)}]$ , with  $C_l(t \rightarrow \infty) = C_{l_{static}}$ , and  $C_l(t = a) = 0.632C_{l_{static}}$ .  $a$  must have the same units as  $t$  and it is called the time constant. The relaxation times, according to this definition, are indicated by vertical lines. It should be noted, as evidenced by Fig. 6, that these calculations of the relaxation times are conservative because they did not take the time-averaged static values (denoted by solid symbols) to be the necessary equilibrium value. The second ramp motion, which crosses the critical state, illustrates that even at the end of the sampling period the vortical rolling moment contribution has not yet reached the static value.

These (63%) relaxation times were quantified for several ramp motions with positive and negative roll rates about various critical states. The nondimensional relaxation times  $t_{63\%}^*$ , as well as the  $\Delta C_{l_{max}}$  (from the end of the ramp to the assumed steady-state value) are included in Table 2.

Table 2 reveals the relaxation time constant about the 5-deg critical state ( $t_{63\%}^* \approx 70$ ) to be quite large. The 8-deg critical state yielded a lower value ( $t_{63\%}^* \approx 50$ ). Calculations of the relaxation time constants for the 11.3-deg critical state, although not included in the table, found  $t_{63\%}^* \approx 10$ . The  $\Delta C_{l_{max}}$  values used to calculate the relaxation time constants for the 11.3-deg critical state, however, were very small. Therefore, these relaxation time constants were less meaningful. This might be expected from Fig. 3, which shows that for roll-angle variations around 11.3 deg, the difference in the static rolling-moment coefficient is small.

The relaxation time constants calculated for ramp motions that did not involve crossing a critical state yielded values of  $t_{63\%}^* \approx 30$ . For these motions, where vortex breakdown existed over the wing, the time constant reflects the relaxation time resulting from the response of vortex breakdown.

The range of ramp motions examined allowed history effects across critical states to be assessed. As shown in Fig. 4, ramp motions were conducted for  $\phi$  between  $-4$  and  $6$  deg, between  $-4$  and  $7$  deg, and between  $6$  and  $7$  deg. The rolling-moment data obtained for the ramp from  $6$  to  $7$  deg were compared to the rolling moment data for the ramp from  $-4$  to  $7$  deg with the rolling-moment data for the ramp from  $-4$  to  $6$  deg subtracted. The result of this subtraction is denoted  $\Delta = 6$  to  $7$  deg. This comparison is shown in Fig. 7a. Note again that the potential flow contribution to the rolling moment was subtracted, leaving just the vortical contribution. This plot reveals no significant history effects on the rolling moment coefficient in the  $\phi$  range from  $6$  to  $7$  deg after crossing the 5-deg critical state. Table 2 also illustrates that the time constants ( $t_{63\%}^* \approx 30$ ) determined for  $\Delta = 6$  to  $7$  deg were approximately equal to the time constant determined for a direct ramp motion from  $6$  to  $7$  deg.

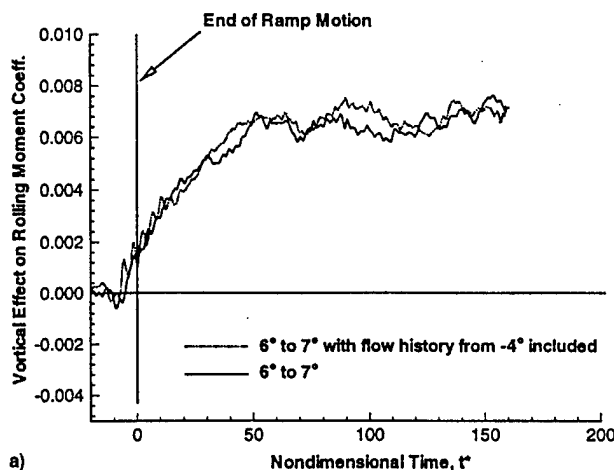
The same type of procedure was used to examine the history effect on the subsequent response after passing through the 8-deg critical state. Figure 7b illustrates the comparison between the vortical rolling moment coefficient for a ramp from  $9$  to  $10$  deg with a ramp from  $6$  to  $10$  deg, subtracting the history of the ramp from  $6$  to  $9$  deg. This comparison illustrates a noticeable difference between the two results. Therefore, including the flow history from  $6$  to  $9$  deg, which crosses the 8-deg critical state, produced a distinctly different transient response over the  $9$ - to  $10$ -deg range. The causes for and conditions under which critical-state history effects become important are not yet understood. This will be a subject of future investigations.

The effect of roll rate on the critical-state transients was investigated using the data obtained with different roll rates over the same roll-angle range. Figure 8, which contains the vortical contribution to the rolling moment coefficient for three different roll rates, reveals that the roll rate has no significant effect on the transients for the 5-deg critical state. Again, Table 2 illustrates that the time constants for each roll rate were all approximately  $t_{63\%}^* \approx 70$ .

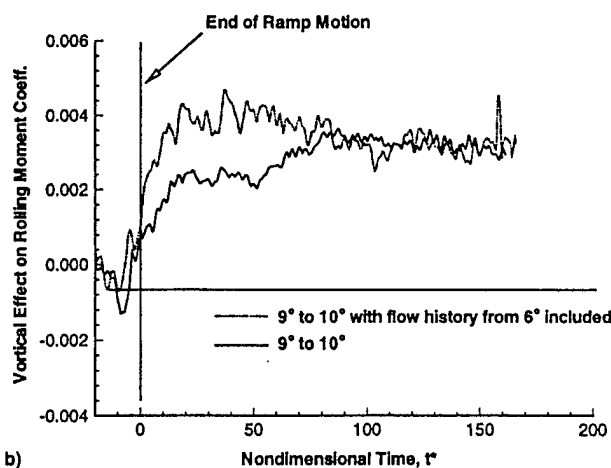
Table 2 Relaxation times to 63% of steady-state values for various ramp motions

Critical state, deg	Rate rad/s, ND	Up/down	Precritical state		Crossing critical state		Postcritical state	
			$t_{63\%}^*$	$\Delta C_{l_{max}}$	$t_{63\%}^*$	$\Delta C_{l_{max}}$	$t_{63\%}^*$	$\Delta C_{l_{max}}$
5			-4 to 4 deg		-4 to 6 deg		-4 to 7 deg	
					$\Delta = 4$ to 6 deg <sup>a</sup>		$\Delta = 6$ to 7 deg	
	1 (0.003)	Up	36	0.010	62	0.014	30	0.006
	4 (0.012)	Up	33	0.014	68	0.014	40	0.007
	7 (0.020)	Up	33	0.014	73	0.006	47	0.007
8			7 to 6 deg		7 to 4 deg		7 to -4 deg	
					$\Delta = 6$ to 4 deg		$\Delta = 4$ to -4 deg	
	1 (0.003)	Down	24	-0.006	61	-0.014	78	-0.010
			6 to 7 deg		6 to 9 deg		6 to 10 deg	
					$\Delta = 7$ to 9 deg		$\Delta = 9$ to 10 deg	
			10 to 9 deg		10 to 7 deg		10 to 6 deg	
	1 (0.003)	Up	33	0.006	42	0.009	5	0.004
					$\Delta = 9$ to 7 deg		$\Delta = 7$ to 6 deg	
	1 (0.003)	Down	14	-0.002	53	-0.008	34	-0.005

<sup>a</sup>  $\Delta = 4$  to 6 deg denotes moment response for  $\phi$  from -4 to 4 deg was subtracted from moment response for  $\phi$  from -4 to 6 deg.



a)



b)

Fig. 7 Response of the vortical contribution to  $C_l$  with and without the prior motion history through the a) 5- and b) 8-deg critical state included ( $\phi_{ND} = 0.003$ ).

#### Harmonic Motions

The rolling-moment responses for numerous harmonic roll oscillations were obtained. Figure 9 contains rolling-moment-coefficient responses for 5-deg amplitude harmonic oscillations in roll. These oscillations, which vary in frequency from 1.1 to 11 Hz ( $0.010 \leq k \leq 0.105$ ), are centered about  $\phi = 3$  deg. The solid symbols in Fig. 9 show the static results and the dashed curve shows the static potential flow contribution to  $C_l$ . These  $C_l$  loops run in a counterclockwise sense, therefore,

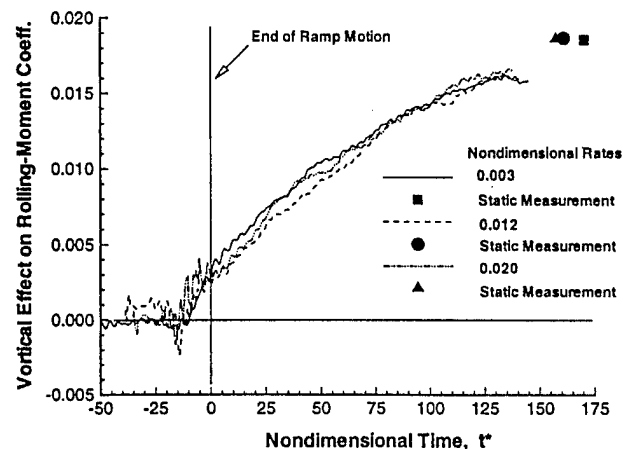


Fig. 8 Roll-rate effect on the transient  $C_l$  response through the 5-deg critical state.

at a given  $\phi$ ,  $C_l$  on the upstroke is less than  $C_l$  on the downstroke.

For the oscillation of lowest frequency,  $k = 0.010$ ,  $C_l$  attempts to follow the curvature of the static data. As the frequency is increased, however, the deviation from the static data becomes more apparent. For all but the lowest frequency the rolling moment response no longer even remotely resembles the curvature of the static data. For each oscillation shown in Fig. 9,  $C_l$  for  $\phi_{min}$  and  $\phi_{max}$  were obtained. A line (dash-double-dot) is shown connecting these two values for each oscillation. Even at the lowest frequency,  $C_l$  values at the roll angle limits ( $\phi \approx 0$ ) do not reach their static values. With increasing frequency the slope of the line connecting the roll angle limits moves closer to the slope of the potential flow contribution. It would be expected that for a harmonic oscillation of very large frequency, the flow would respond only to the virtually instantaneously reacting flow component. Furthermore, the amplitude of the rolling-moment response loops decreases as frequency increases. Figure 9 also illustrates that on the upstroke, in the range of the offset angle,  $\phi = 3$  deg, the value of  $C_l$  is virtually independent of roll rate. However, on the downstroke, after crossing the 5-deg critical state, the roll rate has a significant effect on the rolling-moment coefficient.

Using the nonlinear indicial response model (NIR) and the superposition integral (presented in detail in previous papers<sup>15,16</sup>), the classic Taylor-series expansion for the aerodynamic response to a motion input can be derived.<sup>17</sup> When these results are specialized to the case of forced harmonic motion, relationships are established between specific stability derivatives (both linear and nonlinear) and the variation of the aero-

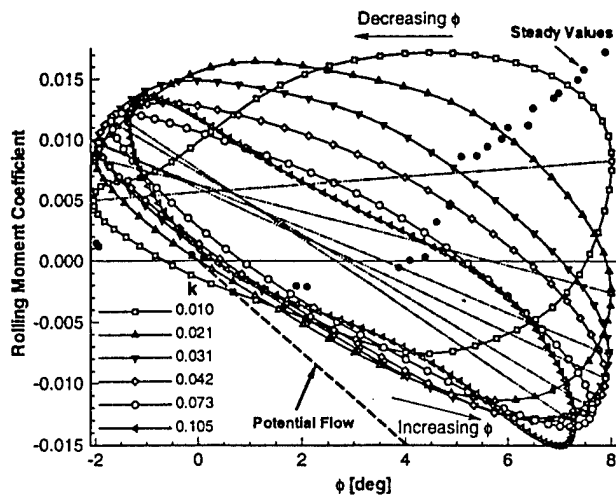


Fig. 9  $C_l$  response to 5-deg-amplitude harmonic motions centered at  $\phi = 3$  deg.

dynamic responses at harmonics of the forcing frequency. That is, for the steady-state response to a harmonic motion input; e.g.,

$$\phi(t) = \phi_0 + \Delta\phi \cos(kt) \quad (4)$$

the rolling moment response can be shown to be of the form

$$C_{l_{dyn}} = C_{l_0} + F_1 \cos(kt) + F_2 \cos(2kt) + F_3 \cos(3kt) + \dots + G_1 \sin(kt) + G_2 \sin(2kt) + G_3 \sin(3kt) + \dots \quad (5)$$

where each of the in-phase coefficients  $F_n$  is a summation of the contributions  $f_{n,j}$  from particular stability parameters that are designated by the subscript  $j$ . Therefore,

$$F_n = \sum_{j=1}^{j_{\max}} f_{n,j}$$

Similarly, out-of-phase terms  $G_n$  also consist of contributions  $g_{n,j}$ . The individual contributions can be factored into the form

$$f_{n,j} = \tilde{f}_{n,j}(\phi_0, \Delta\phi)[a_2 k^2 + a_4 k^4 + \dots] \quad (6)$$

$$g_{n,j} = \tilde{g}_{n,j}(\phi_0, \Delta\phi)k[b_1 + b_3 k^2 + b_5 k^4 + \dots]$$

Note that the frequency effect appears as a power series in  $k$ . Also, the coefficients of these terms, ( $a_i$ ,  $b_i$ ), correspond to the relevant stability derivative. Furthermore, the higher-order terms (in  $k$ ) arise from repeated differentiation of the motion parameters.<sup>17</sup> Differentiation of  $\sin(nkt)$  gives  $nk \cos(nkt)$ . That is, the series proceeds in the order  $b_1(nk) + a_2(nk)^2 + \dots$ . Thus, if

$$k > 1/(na_2/b_1)$$

the series diverges.

It must also be noted that this analysis is valid under the following conditions:

1) The motion is analytic (which is true for forced oscillation tests).

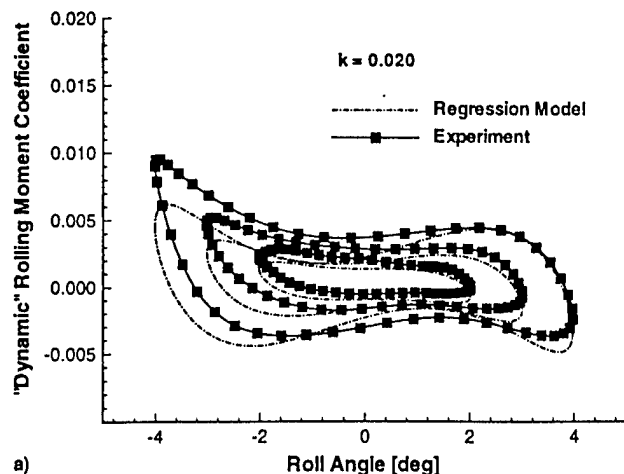
2) The motion does not cross a critical state.

3) Time constants for the indicial response transients are less than  $1/nk$ , where  $nk$  is the frequency of the affected harmonic.

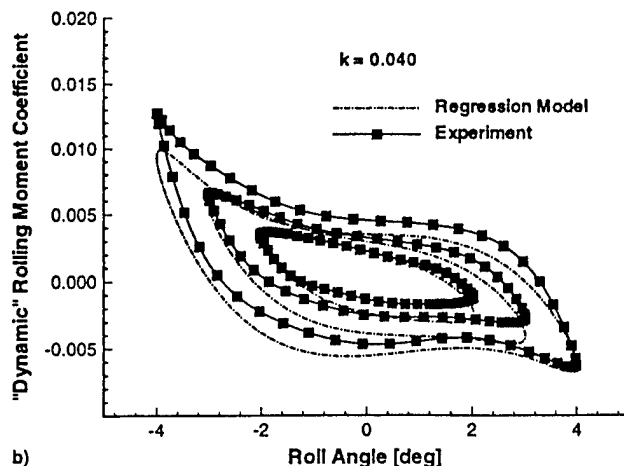
The convergence properties of the series representation (when applied to harmonic motion) can be used to provide an independent check of indicial response time scales. From ramp-and-hold motion data (see Table 2), indicial response time constants of about 30 are expected in the roll angle range

Table 3 Regression results

$j$	Parameter	Harmonic, $n$	$na_2/b_1$	$k_{crit}$
1	Linear, $\phi$	1	28.4	0.035
2	$\phi^2 \phi$	1	19.5	0.051
3	$\phi \phi \phi$	1	16.0	0.063
4	$\phi \phi \phi$	2	24.8	0.040



a)



b)

Fig. 10  $C_{l_{dyn}}$  for harmonic oscillations centered at  $\phi = 0$  deg for  $k =$  a) 0.02 and b) 0.04.

between the critical states at  $\pm 5$  deg. Thus, for harmonic motions in this range, the series approximation is expected to converge for reduced frequencies below about 0.033. Therefore, harmonic motions (centered about 0-deg roll angle and with amplitudes of 2, 3, and 4 deg) at the two lowest frequencies,  $k = 0.02$  and  $0.04$ , were analyzed. A stepwise regression analysis<sup>7</sup> was used to identify the most significant terms in the series expansion. The correlation coefficient for the regression was 0.886, and comparisons between experimental and predicted  $C_{l_{dyn}}$  are shown in Figs. 10a and 10b. Although the data trends with frequency and amplitude are well captured by the regression model, the overall agreement may be compromised by the fact that  $k = 0.04$  slightly exceeds the expected range of applicability.

Four separate contributions were identified; i.e.,  $j_{\max} = 4$ . The results are summarized in Table 3. As shown, the key contributors are the first and fourth parameters, both showing divergence for  $k \approx 0.04$ . Thus, these results also show that application of the procedure to data taken at  $k = 0.04$  is marginal. Moreover, the regression analysis confirms that indicial response time constants, as determined from ramp and hold maneuvers, are correct within approximately 10%. It also suggests

that some of the nonlinear contributions are somewhat faster, contradicting the assumption that the decaying loads are simple exponentials.

### Conclusions

Experimental force and moment measurements were made for both harmonic and ramp-and-hold motions in roll. These experiments were designed to isolate critical-state effects. For the first time, evidence showing significant critical-state transients was presented. Several conclusions regarding these critical-state transients are as follows.

- 1) Severe time lags ( $t_{63\%}^* \approx 30$ ) existed for motions during which a critical state was not crossed (for  $-4 \text{ deg} < \phi < 4 \text{ deg}$ ). Therefore, stability derivatives are not valid for reduced frequencies,  $k \geq 0.033$ .
- 2) An independent assessment of the longest time-scales in the  $|\phi| < 5\text{-deg}$  range based on relationships between stability derivatives and indicial response characteristics confirmed  $t_{63\%}^* \approx 30$ . Also, the good agreement between independent experiments also supports the validity of nonlinear indicial response theory as applied to these data.
- 3) Critical-state encounters often have a severe effect on the transient rolling moment behavior.
- 4) The 5-deg critical state yielded the longest transient effects. A relaxation time,  $t_{63\%}^* \approx 70$ , was found when crossing this critical state from either above or below. Crossing the range including the 5-deg critical state, however, did not yield a noticeable history effect on the subsequent response for  $\phi$  from 6 to 7 deg.
- 5) The 8-deg critical state yielded slightly smaller relaxation times  $t_{63\%}^* \approx 50$  compared to the 5-deg critical state. However, including the flow history response for a crossing of the 8-deg critical state yielded a noticeable history effect on the subsequent response for  $\phi$  from 9 to 10 deg.
- 6) The analysis of the 11.3-deg critical state was not conclusive because the overall change in rolling moment coefficient from the end of the ramp to its steady-state value was very small.
- 7) Responses to roll motions at the examined angle of attack and roll angles exhibit three distinct time scales (potential, vortical, and critical-state transients). These time scales must be accounted for to achieve accurate aerodynamic models.

### Acknowledgments

This work was conducted under a Joint Research Program of the U.S. Air Force Office of Scientific Research, Wright Laboratory, the Institute for Aerospace Research, and the Canadian Department of National Defence. The support of these organizations is gratefully acknowledged.

### References

- <sup>1</sup>Jobe, C. E., Hsia, A. H., Jenkins, J. E., and Addington, G. A., "Critical States and Flow Structure on a 65-Deg Delta Wing," *Journal of Aircraft*, Vol. 33, No. 2, 1996, pp. 347-352.
- <sup>2</sup>Jenkins, J. E., Myatt, J. H., and Hanff, E. S., "Body-Axis Rolling Motion Critical States of a 65-Degree Delta Wing," *Journal of Aircraft*, Vol. 33, No. 2, 1996, pp. 268-278.
- <sup>3</sup>Huang, X. Z., and Hanff, E. S., "Roll Rate Induced Camber Effect on Delta Wing Leading-Edge Vortex Breakdown," AIAA Paper 95-1793, June 1995.
- <sup>4</sup>Ericsson, L., and Hanff, E. S., "Further Analysis of High-Rate Rolling Experiments of a 65-Deg Delta Wing," *Journal of Aircraft*, Vol. 31, No. 6, 1994, pp. 1350-1357.
- <sup>5</sup>Huang, X. Z., Hanff, E. S., Jenkins, J. E., and Addington, G., "Leading-Edge Vortex Behavior on a 65° Delta Wing Oscillating in Roll," AIAA Paper 94-3507, Aug. 1994.
- <sup>6</sup>Huang, X. Z., and Hanff, E. S., "Prediction of Normal Force on a Delta Wing Rolling at High Incidence," AIAA Paper 93-3686, Aug. 1993.
- <sup>7</sup>Hsia, A. H., Myatt, J. H., and Jenkins, J. E., "Nonlinear and Unsteady Aerodynamic Responses of a Rolling 65-Delta Wing," AIAA Paper 93-3682, Aug. 1993.
- <sup>8</sup>Addington, G., and Jenkins, J., "Flow Visualization of a Rolling Delta Wing and Its Pertinence to the Nonlinear Indicial Response Model," AIAA Paper 93-3469, Aug. 1993.
- <sup>9</sup>Huang, X. Z., and Hanff, E. S., "Prediction of Leading-Edge Vortex Breakdown on a Delta Wing Oscillating in Roll," AIAA Paper 92-2677, June 1992.
- <sup>10</sup>Hanff, E. S., and Huang, X. Z., "Roll-Induced Cross-Loads on a Delta Wing at High Incidence," AIAA Paper 91-3223, Sept. 1991.
- <sup>11</sup>Hanff, E. S., and Jenkins, J. B., "Large-Amplitude High-Rate Rolling Experiments on a Delta and Double Delta Wing," AIAA Paper 90-0224, Jan. 1990.
- <sup>12</sup>Hanff, E. S., Kapoor, K., Anstey, C. R., and Prini, A., "Large-Amplitude High-Rate Roll Oscillation System for the Measurement of Non-Linear Loads," AIAA Paper 90-1426, June 1990.
- <sup>13</sup>Jenkins, J. E., and Hanff, E. S., "Highlights of the IAR/WL Delta Wing Program," AIAA Workshop on Delta Wings: Unsteady Aerodynamics and Modeling, Atmospheric Flight Mechanics Conf., Aug. 1995.
- <sup>14</sup>Youngren, H. H., Bouchard, E. E., and Coopersmith, R. M., "Quadrilateral Element Panel Method: User's Manual Ver. 3.2," Lockheed-California Co., Burbank, CA, 1984.
- <sup>15</sup>Tobak, M., and Chapman, G. T., "Nonlinear Problems in Flight Dynamics Involving Aerodynamic Bifurcations," *AGARD Symposium on Unsteady Aerodynamics—Fundamentals and Applications to Aircraft Dynamics*, CP-386, AGARD, 1985, pp. 25-1-25-15.
- <sup>16</sup>Tobak, M., Chapman, G. T., and Unal, A., "Modeling Aerodynamic Discontinuities and Onset of Chaos in Flight Dynamical Systems," *Annales des Telecommunications*, Tome 42, Nos. 5, 6, 1987, pp. 300-314; also NASA TM-89420, Dec. 1986.
- <sup>17</sup>Jenkins, J. E., "Simplification of Nonlinear Indicial Response Models: Assessment for the Two-Dimensional Airfoil Case," *Journal of Aircraft*, Vol. 25, No. 2, 1991, pp. 131-138.